Downloaded from orbit.dtu.dk on: Dec 20, 2017

Technical University of Denmark

An experimental and theoretical investigation of annular steam-water flow in tubes and annuli at 30 to 90 bar

Forskningscenter Risø, Roskilde

Publication date:
1978

Document Version
Publisher's PDF, also known as Version of record

Link back to DTU Orbit

Citation (APA):
Würtz, J. (1978). An experimental and theoretical investigation of annular steam-water flow in tubes and annuli at 30 to 90 bar. (Denmark. Forskningscenter Risoe. Risoe-R; No. 372).

DTU Library
Technical Information Center of Denmark

General rights
Copyright and moral rights for the publications made accessible in the public portal are retained by the authors and/or other copyright owners and it is a condition of accessing publications that users recognise and abide by the legal requirements associated with these rights.

- Users may download and print one copy of any publication from the public portal for the purpose of private study or research.
- You may not further distribute the material or use it for any profit-making activity or commercial gain
- You may freely distribute the URL identifying the publication in the public portal

If you believe that this document breaches copyright please contact us providing details, and we will remove access to the work immediately and investigate your claim.

Risø Report No. 372

Risø Report No. 372

Risø National Laboratory

An Experimental and Theoretical Investigation of Annular Steam-Water Flow in Tubes and Annuli at 30 to 90 bar

by Jørgen Würtz

April 1978

Risø Bibliotek
- [illegible]/1979
Forsøgsanlæg Risø

Sales distributors: Jul. Gjellerup, Sølvgade 87, DK-1307 Copenhagen K, Denmark

Available on exchange from: Risø Library, Risø National Laboratory, P.O. Box 49, DK-4000 Roskilde, Denmark

INIS Descriptors

ANNULAR SPACE
BURNOUT
CRITICAL HEAT FLUX
DEPOSITION
DRYOUT
ENTRAINMENT
EXPERIMENTAL DATA
FILM FLOW
FILMS
FLOW MODELS
FLOW RATE
HZ RANGE
MEDIUM PRESSURE
PRESSURE DROP
PRESSURE GRADIENTS
STEAM
TABLES
THICKNESS
TUBES
TWO-PHASE FLOW
WATER
WAVE PROPAGATION

UDC 621.039.524.4-97 : 532.529 : 536.248.2

April 1978 Risø Report No. 372

An Experimental and Theoretical Investigation of Annular Steam-Water Flow in Tubes and Annuli at 30 to 90 bar

by

Jørgen Würtz

Risø National Laboratory
Department of Reactor Technology

Abstract

Measurements are presented of film flow rates, pressure gradients, film thicknesses, wave frequencies and velocities, and burnout heat fluxes in one annular and two tubular geometries. The more than 250 experiments were performed with steam-water at 30 to 90 bar under both adiabatic and diabatic conditions. On the basis of these data a film-flow model for the prediction of burnout is set up. General film roughness and entrainment correlations are derived from the adiabatic, equilibrium data. The capability of the model is demonstrated by several comparisons between calculations and measurements.

This report is submitted to the Technical University of Denmark in partial fulfilment of the requirements for obtaining the lic.tech. (Ph.D.) degree.

ISBN 87-550-0593-4
ISSN 0418-6443

CONTENTS

1. INTRODUCTION

Power generation in nuclear boiling water reactors is limited by a thermohydraulic phenomenon called burnout. When the heat flux is increased beyond a certain level (called the burnout or critical heat flux), the temperature at the heated wall suddenly increases (cf. fig. 1.1). In a nuclear fuel element this temperature excursion may result in fuel cladding rupture accompanied by the release of radioactive gases or solids into the coolant.

To avoid this risk it is necessary to know the value of the critical heat flux, so that a reasonable value of the operating heat flux can be estimated. It is obvious that the value of the necessary factor of safety used in this estimation is strongly dependent on the accuracy of our knowlegde of the burnout heat flux.

To obtain information about the critical value, numerous burnout experiments have been carried out during the last twenty-five years. The burnout heat flux has been found to depend on the operating variables. These include pressure, mass flow rate, length and shape of the channel, liquid inlet subcooling, etc. Burnout measurements were at first only used to evaluate purely empirical relationships between the critical heat flux and the operating variables.

In the middle of the 1960's it was, however, verified that burnout at high steam qualities results from the disappearance of a liquid film that is normally found on the heated wall. Based on this fact, burnout models were evolved that described the variation of the liquid film with the operating variables.

This development has, however, been limited due to the lack of experimental information on the variation of the film. Hitherto, only very few film flow measurements have been carried out with steam-water at operating pressures for boiling water reactors. Thus most of the film-flow models developed until now have been based on burnout heat flux data, and supplied with information on the film flow achieved from experiments performed with air-water mixtures at low pressures. Because of the great differences in the properties of air-water at 1 bar and steam-water at 70 bar, it has been very difficult to develop correlations that correctly describe the steam-water film flow.

The experimental part of this report (chapter 3) is an attempt to rectify this lack of a consistent set of film flow data achieved with steam-water at high pressures. More than 200 film flow measurements are presented, and they are accompanied by experimental values of pressure gradients, film thicknesses, wave frequencies and velocities, and burnout heat fluxes. The experiments were carried out under both adiabatic and diabatic conditions in one annular and two tubular geometries.

On the basis of these data, a film-flow model for the prediction of burnout in tubes and annuli is developed in the analytical part of the report (chapter 4). Finally, the capability of the model is shown by comparisons of predicted and experimental values.

2. ANNULAR TWO-PHASE FLOW

The flow regime, which is characterized by the presence of a liquid film adjacent to the channel wall, is called the annular two-phase flow regime. This chapter only deals with the general aspects of annular flow in a very superficial way. A detailed description of this topic (especially regarding air-water systems) is given by Hewitt and Hall-Taylor (1970). The terminology used in the present report follows to a great extent that used in this recommendable textbook.

2.1. Flow Regimes

The evolution of the annular flow pattern is illustrated in conceptual form in fig. 2.1. Here a tube is shown with a heated wall, where the liquid is introduced at the bottom.

The first generation of steam takes place by nucleation at the wall, producing steam bubbles. As the fluid proceeds up the tube, further generation of steam takes place, and the small bubbles coalesce into bullet-shaped bubbles called slugs. After the slug flow regime, a transition region called the churn flow regime is reached. This flow pattern is a result of instabilities in the slugs due to the increase of the steam velocity It is characterized by a "churning" or oscillatory action.

After this transition region, the annular flow regime is established. It is seen that the liquid film is strongly agi-

tated by the gas stream. Thus large roll waves are generated on the film surface and liquid is torn off. This entrained liquid is carried along as droplets or agglomerates ("wisps") in the gas core, until they are deposited onto the film. The size of the droplets and wisps is gradually reduced as the gas velocity is increased.

Due to the increased steam generation, the film thickness decreases until the burnout point is reached. At that point (also called the dryout locus), where the heated wall becomes dry and the wall temperature abruptly increases, liquid droplets are still entrained in the gas stream. This flow pattern, called the mist flow regime, is present in the channel until all the droplets are evaporated, so a single-phase steam flow is achieved.

2.2. Basic Flow Parameters

This section gives the definitions of the basic flow parameters used in the succeeding chapters.

The total (mass) flow rate m(kg/s) is given by

$$m = m_f + m_e + m_g = m_l + m_g \tag{2.1}$$

where

m_f(kg/s) is the film flow rate,
m_e(kg/s) is the flow rate of entrained liquid,
m_g(kg/s) is the gas flow rate, and
m_l(kg/s) is the total liquid flow rate.

The mean steam quality x(-) is defined by

$$x \equiv \frac{m_g}{m} . \tag{2.2}$$

The definition of the mean void fraction α(-) is given by

$$\alpha \equiv \frac{A_g}{A} = \frac{A_g}{A_g + A_l} \tag{2.3}$$

where

$A(m^2)$ is the cross-sectional area of the channel,
$A_g(m^2)$ is the cross-sectional area of the steam,
and $A_l(m^2)$ is the cross-sectional area of the liquid.

The (total) mass flux $G(kg/m^2s)$ is defined by the ratio:

$$G \equiv \frac{\dot{m}}{A} . \tag{2.4}$$

The mean velocity of the gas $\bar{u}_g(m/s)$ is related to G through

$$\bar{u}_g = \frac{\dot{m}_g}{\rho_g A_g} = \frac{\dot{m}x}{\rho_g A_g} = \frac{Gx}{\rho_g \alpha} \tag{2.5}$$

where $\rho_g(kg/m^3)$ is the density of the gas.

The relationship between the mass flux and the mean velocity of the liquid (film and entrainment) $\bar{u}_l(m/s)$ is developed in a similar way:

$$\bar{u}_l = \frac{\dot{m}_l}{\rho_l A_l} = \frac{\dot{m}(1-x)}{\rho_l A_l} = \frac{G(1-x)}{\rho_l (1-\alpha)} \tag{2.6}$$

where $\rho_l(kg/m^3)$ is the density of the liquid.

The ratio between $\bar{u}_g$ and $\bar{u}_l$ is denominated the mean slip ratio S(-):

$$S \equiv \frac{\bar{u}_g}{\bar{u}_l} = \frac{x}{1-x} \frac{1-\alpha}{\alpha} \frac{\rho_l}{\rho_g} . \tag{2.7}$$

2.3. Previous Experimental Work

2.3.1. Measurements of Film Flow Rates

Measurements of the liquid film flow rate by extraction of the film through a permeable section of the channel have been carried out through several years.

In some of the earliest investigations (Bennet and Thornton (1961); Collier and Hewitt (1961); Gill, Hewitt and Lacey (1965)) a slit in the wall was used to divert the liquid film. These measurements were carried out with air-water in a perspex tube with an inner diameter of 31.8 mm. However, a disadvantage of the slit is that the large roll waves are likely to overshoot the rather narrow gap. Therefore poreous sinters or perforated wall sections with a length of app. 5 cm were used in the later studies.

The film flow rate is measured by an estimation of the liquid and the gas flow rate in the extracted mixture. In a two-component system (e.g. air-water) this is done by means of a cyclone separator (cf. e.g. Bennet and Thornton (1961)). For

a one-component flow (e.g. steam-water), the mixture is condensed and heat and mass balances are performed as explained in sections 3.1.2 and 3.2.2. The film flow rate is estimated from a plot of the liquid flow rate versus the gas flow rate as discussed in section 3.3.1.

One of the most comprehensive sets of film flow data with air-water mixtures was reported by Whalley, Hewitt and Hutchinson (1973). The report also includes measurements with air-trichloroethane mixtures, where the surface tension is much smaller than for air-water. The measurements were carried out in a tube 31.8$^{\emptyset}$mm with a length of 18.9 m. By applying two different injection methods (axial jet and porous wall) it was shown that the flow in this very long tube was independent on the inlet conditions. It was therefore made probable that a single equilibrium state exists for a particular liquid and gas flow rate.

The first measurements with steam-water mixtures were carried out at low pressure (3.8 bar) by Hewitt et al. (1965). They were performed under diabatic conditions (i.e. with a heated wall) in a 9.3$^{\emptyset}$mm tube, and they showed that the film flow rate tends to zero as the burnout point is approched. Hewitt and Pulling (1969) measured the corresponding film flow rates under adiabatic conditions (i.e. with no heat transfer at the wall). Bennet et al. (1967) performed diabatic experiments with the same test section but with unheated lengths (cold patches) between the heated lengths. These measurements showed that the film tends toward the adiabatic values at the cold pathes.

The first high pressure steam-water film flow measurements were performed by Singh et al. (1969). They were carried out under adiabatic conditions at 69 and 84 bar in a tube with an internal diameter of 12.5 mm. Some of these results are, together with examples of the measurements mentioned below, shown in chapter 3. Measurements under diabatic conditions with steam-water at 69 bar were first reported by Bennet et al.(1969). Film flow rates were estimated in a 12.7$^{\emptyset}$mm tube with a heated length of 3.66 m. As in the low pressure experiments by Hewitt et al. (1965), the film flow shows a smooth decrease towards zero at the burnout point. The 12.7$^{\emptyset}$mm tube was also used in the adiabatic and diabatic measurements by Keeys, Ralph and Roberts (1970 a,b).

A tube with an internal diameter of 13.3 mm was used in the experiments by Nigmatulin, Malyshenko and Shugaev (1976). These adiabatic measurements were mainly performed at 50 bar, but results as 10, 20, 30, 70 and 100 bar are also reported.

It is seen that all experiments in tubes with steam-water at high pressures until now have been carried out with diameters of approximately 13 mm. One of the main objectives of the present work is to investigate the influence of geometry on annular flow. Thus in the present report film flow measurements in tubular test sections with internal diameters of 10 and 20 mm are presented.

Film flow measurements in an annular test section with steam-water mixtures were performed by Moeck (1970). The experiments were carried out in a concentric annulus at 35 and 69 bar. The rod diameter was 19.7 mm and the internal tube diameter 23.8 mm. The total length of the test section was 2.9 m. Most of the experiments were performed under diabatic conditions with a movable heater inside the rod. However, also a few measurements were carried out under adiabactic conditions. These measurements showed that the tube carried much more liquid per unit perimeter than the rod film. This asymmetry was also detected in the adiabatic experiments by Mannov (1973b). Here the test section consisted of a $17.0^{\emptyset}$mm rod mounted concentrically inside a $27.2^{\emptyset}$mm tube. The total length of this test section was 3.5 m.

Due to the relatively short lengths of the two annuli, it was not absolutely certain that the flow was fully developed, i.e. that the equilibrium situation was reached in the experiments. However, the present adiabatic measurements in a long (8 m) annulus ($17^{\emptyset}/26^{\emptyset}$ mm) confirm that the asymmetry is present in the equilibrium situation.

The first diabatic measurements in annuli with both a heated rod and tube wall were performed by Jensen and Mannov (1974) in a 3.5 m long annulus ($17^{\emptyset}/26^{\emptyset}$mm). This investigation of the influence of the relative heat flux distribution on the film flow rates is continued in the present work.

Finally, it should be mentioned that Andersen et al. (1974) measured the circumferential film flow distribution in an eccentric annulus with steam-water mixtures. Here it appeared that the minimum film flow rate occured at the minimum gap. A similar result was achieved by Schraub et al. (1969) with air-

Table 2.1. Film Flow Measurements with Steam-Water in Tubes and Annuli

Reference	Test Section	Number of exp.	Test Conditions	Pressure	Mass Flux
				bar	kg/m^2s
Hewitt et al. (1965)	Tube $9.3^{\varnothing}$mm	38	Diabatic	3.8	298
Bennet et al. (1967)	Tube $9.3^{\varnothing}$mm	27	Diabatic	3.8	298
Hewitt and Pulling (1969)	Tube $9.3^{\varnothing}$mm	67	Adiabatic	2.4-4.5	298
Bennet et al. (1969)	Tube $12.7^{\varnothing}$mm	33	Diabatic	69	1360-2720
Singh et al. (1969)	Tube $12.5^{\varnothing}$mm	22	Adiabatic	69-84	275-960
Keeys, Ralph and Roberts (1970a)	Tube $12.7^{\varnothing}$mm	21	Adiabatic	34-69	1313-2765
Keeys, Ralph and Roberts (1970b)	Tube $12.7^{\varnothing}$mm	20	Diabatic	69	1360-2720
Nigmatulin et al. (1976)	Tube $13.3^{\varnothing}$mm	45	Adiabatic	10-100	500-4000
Present Report	Tube $10.0^{\varnothing}$mm	81	Adiabatic	30-90	500-3000
Present Report	Tube $10.0^{\varnothing}$mm	79	Diabatic	30-90	500-3000
Present Report	Tube $20.0^{\varnothing}$mm	21	Adiabatic	70	500-2000
Moeck (1970)	Cc. Ann. $19.7^{\varnothing}/23.8^{\varnothing}$mm	8	Adiabatic	34-69	250-2700
Moeck (1970)	Cc. Ann. $19.7^{\varnothing}/23.8^{\varnothing}$mm	91	Diabatic	34-69	250-2700
Mannov (1973b)	Cc. Ann. $17.0^{\varnothing}/27.2^{\varnothing}$mm	29	Adiabatic	70	400-1975
Mannov (1973b)	Cc. Ann. $17.0^{\varnothing}/27.2^{\varnothing}$mm	21	Diabatic	30-70	400-1200
Andersen et al. (1974)	Ec. Ann. $17.0^{\varnothing}/27.2^{\varnothing}$mm	43	Diabatic	70	600-1200
Jensen and Mannov (1974)	Cc. Ann. $17.0^{\varnothing}/26.0^{\varnothing}$mm	16	Diabatic	70	900-1200
Present Report	Cc. Ann. $17.0^{\varnothing}/26.0^{\varnothing}$mm	26	Diabatic	70	500-1000
Present Report	Cc. Ann. $17.0^{\varnothing}/26.0^{\varnothing}$mm	29	Adiabatic	30-90	500-2000

water mixtures. This contrasts, however, with the work of Butterworth (1968). He measured a uniform film flow distribution in an eccentric annulus with air-water, and found that the thickest film occured at the narrowest gap.

The available film flow measurements with steam-water mixtures in tubes and annuli are summarized in table 2.1.

2.3.2. Pressure Drop Measurements

While the number of film flow measurements are rather few, several thousands pressure drop data for steam-water mixtures are reported (cf. Collier (1977)). Thus more than 2700 measurements are referred by Friedel (1977). The measurements in tubes are carried out within the following intervals:

Tube diameter	3.2	-	55.9	mm
Pressure	1	-	212	bar
Mass flux	99	-	8210	kg/m^2s.

The main purpose with the present pressure drop measurements is, however, not to extend these intervals, but to obtain corresponding values of the film flow rate and the frictional pressure gradient.

2.3.3. Burnout Power Measurements

As already mentioned in the introduction numerous burnout measurements have been carried out. Thus Nilsson and Larsson (1971) refer more than 8400 measurements performed in tubes with steam-water within the following ranges:

Tube diameter	3.9	-	44.7	mm
Heated length	0.035	-	7.10	m
Pressure	2.4	-	221	bar

In addition to these measurements 3767 burnout measurements in annuli are referred. These experiments are carried out within the following ranges:

Tube diameter	14.1	-	31.8	mm
Rod diameter	9.5	-	15.9	mm
Hydraulic diam.	5.1	-	22.3	mm
Heated length	0.608	-	4.66	m
Pressure	8	-	100	bar

Most of these measurements are performed with heated rod only. Burnout experiments with two-sided heating are reported by Jensen and Mannov (1974) and Becker and Letzter (1975).

2.4. Previous Theoretical Work

2.4.1. Annular Flow Prediction Models for Burnout

One of the earliest burnout models for tubes was developed by Vanderwater in 1956 (cf. Isbin et al. (1961)). The mass balance on the film (eq. (4.39)) was integrated under the following assumptions:

a) The liquid film on the wall acts as a sink for the droplets.
b) No slip is assumed between the phases, i.e. S = 1.
c) The deposition rate is proportional to the mean droplet concentration.
d) The entrainment rate is proportional to the axial velocity and heat flux.
e) The fraction of entrained liquid at the onset of the annular flow regime is constant.
f) Burnout occurs when the film flow rate vanishes.

During the next fifteen years many burnout models have been developed. A summary of some of the most important is given by Hewitt (1978). Most of the models contain the assumptions a), c), e) and f). Instead of assuming the same velocity for the gas and the liquid (assumption b), velocity profiles for the film and the gas core are introduced in most of the models.

The main difference in the varius proposed models is however the way of calculating the entrainment rate (cf. Hewitt (1978)). It is obvious from experiments that Vanderwater's assumption d) of proportionality between the entrainment rate and the heat flux cannot be correct, because measurements under adiabatic conditions show that a great part of the liquid can be entrained in the gas core. The most reliable way of calculating the entrainment rate seems to be the method suggested by Hutchinson and Whalley (1973). Here the entrainment correlation is based on equilibrium film flow data. This method has been applied in a modified way on the present equilibrium data, and a new more general entrainment correlation is obtained (cf. section 4.1.4).

3. EXPERIMENTAL PART

The experimental part of this report is divided into three sections. First is given a description of the experimental equipment. The measuring procedures are then discussed in the following section. Finally, the reported data are shown graphically in the third section. Tabulations of the data are given in Appendix.

The experiments were carried out with steam-water at 30, 50, 70 and 90 bar. The main properties of the medium are given in table 3.1 (Schmidt (1969)).

3.1. Experimental Equipment

The experiments were carried out in the high pressure water loop at the Risø National Laboratory during 1977.

The facility, installed in the Section of Experimental Heat Transfer (SEHT), is shown in the schematic flow diagram fig. 3.1. It is constructed of stainless steel and dimensioned to a critical pressure of 221 bar.

3.1.1. Main Loop Hydraulics

The main pump, built by Nikkiso Co. Ltd., feeds subcooled water into the test section and spray condenser. Its main features are:

Max. temperature	375°C
Max. pressure	225 bar
Dynamic head	150 m
Max. flow	15 l/s
Power	45 kW

The pump feeds water to the test section via two control valves V2 and V5. These valves regulate the flow rate and inlet temperature to the test section. The control valves are operated by compressed air and are regulated, via I/P (current to pressure) converters, by PID (proportional-integral-differential) regulators.

In the test section the steam is generated by means of up to 665 kW electrical power. The outlet temperature and thereby the

Table 3.1 Properties of Steam-water

System Pressure p(bar)	30	50	70	90
Saturation Temperature T_{sat} (^{o}C)	233.8	263.9	285.8	303.3
Density of Steam ρ_g (kg/m^3)	15.01	25.36	36.53	48.79
Density of Water ρ_l (kg/m^3)	822.2	777.7	740.0	705.3
Density Ratio $\rho_l/\rho_g=\rho'$ (-)	54.8	30.7	20.3	14.5
Dynamic Viscosity of Steam μ_g (10^{-6}kg/ms)	16.8	18.0	19.1	20.1
Dynamic Viscosity of Water μ_l (10^{-6}kg/ms)	117	102	94	88
Surface Tension σ (10^{-3}N/m)	30.0	22.9	17.7	13.6
Enthalpy of Water h_2 (kJ/kg)	1008.4	1154.5	1267.4	1363.7
Evaporation Heat r_{ev} (kJ/kg)	1793.9	1639.7	1506.0	1380.9

system pressure (when steam is present) are regulated by control valve V6. The valve regulates the cold water flow from the heat exchanger to the sprays in the condenser.

From the spray condenser, the water returns to the main pump. To prevent pump cavitation, the saturated water from the condenser is mixed with subcooled water from the heat exchanger via valve V11. The subcooling was always kept at a temperature above 10^{o}C.

3.1.2. Heat Balance Unit

The film flow rates are measured by means of a heat balance unit (cf. Mannov (1973a)) shown schematically in fig. 3.2.

At the outlet of the test section a mixture of steam and water is sucked off through a perforation in the wall. The mixture passes through a regenerator where some (perhaps all) of the steam is condensed. From the regenerator the mixture passes

through a heat exchanger, where a subcooling takes place.

The secondary cooling flow through the heat exchanger is measured by one of two flowmeters. The primary flow, the total suction rate, is measured by one of three flowmeters (venturi or orifice) and one of three dp-cells. The measuring range is from 10 g/s to 350 g/s with an accuracy of ± 1.5%.

After the total suction rate is measured, the primary flow is returned to the regenerator, where it is reheated. Finally, it is returned to the main system through the ejector pump at V1 on fig. 3.1.

From the measured flow rates and temperatures T_2 to T_{10}, the film flow rate can be determined as described in sect. 3.2.2.

When the film flow rates on the rod and tube wall in the annular test section are determined, two heat balance units are used. However, the measurements were not carried out simultaneously because the opposite film might be disturbed.

3.1.3. Test Sections

The following test sections were used during the experimental periods (cf. table 3.2):

Period 1: Annular test section 17/26S
$d_1 = 0.017$ m, $d_2 = 0.026$ m, $l = 3.5$ m

Periods 2-4: Tubular test section 10
$d_2 = 0.010$ m, $l = 9.0$ m

Period 5: Annular test section 17/26L
$d_1 = 0.017$ m, $d_2 = 0.026$ m, $l = 8.0$ m

Period 6: Tubular test section 20
$d_2 = 0.020$ m, $l = 9.0$ m

where

d_1 (m) is the outer diameter of the rod
d_2 (m) is the inner diameter of the tube
l (m) is the length of the test section

In the adiabatic experiments (periods 2, 5 and 6) the experimental set-up consisted in addition to the test section, of a steam generator placed between the flowmeter and the inlet flange at the test section.

The steam generator is electrically heated as a resistance element. It consists of nine tubes ($d_2 = 0.0083$ m, $l = 4.0$ m)

connected in parallel and equipped with a power clamp at each end.

In the diabatic experiments (periods 1, 3 and 4) the steam generator acted as a preheater. This preheater was used in connection with the control valves V2 and V5 to regulate the inlet temperature to the test section.

The test sections and the steam generator are constructed to withstand a pressure of 100 bar and a temperature of 315°C.

3.1.3.1. Annular Test Sections 17/26S and L. The diabatic experiments in period 1 were carried out with the short annulus (17/26S) with a heated length of 3.5 m. This test section was previously used in the experiments reported by Jensen and Mannov (Jensen(1974); Mannov (1973b); Jensen and Mannov (1974)).

It consists of a rod with an outer diameter of 17 mm, mounted centrally inside a tube with an inner diameter of 26 mm. Both the rod and the tube, made of stainless steel, are heated electrically as resistance elements (cf. fig. 3.3).

The upper part of the test section is shown in detail in fig. 3.4.a.

Just above the outlet end of the heated section, numerous 1.2 mm holes are drilled in the rod and tube walls covering a length of 50 mm (cf. fig. 3.4.b). Through these holes the films on the rod and tube walls are sucked off.

A stainless steel disc, in which a 10 mm silver rod is fastened by brazing, separates the upper rod part from the heated length. The upper end of the silver rod is connected to the stainless steel tube with two fins. As the majority of the electrical current flows in the silver rod, the power generated in the thin-walled steel tube can be neglected.

The outer tube is provided with holes for spacers, needle contact probes and tubes for pressure drop measurements.

The rod is fixed at the top end of the tube, and because of the thermal expansion of the rod, the lower end of the tube is provided with a water-cooled gasket.

When the adiabatic experiments in period 5 were carried out, the middle part of the test section was extended so that the total length of the annulus (17/26L) was 8 m.

3.1.3.2. Tubular Test Sections 10 and 20. The tubular test section 20, with an inner diameter of 20 mm, is shown in fig. 3.5.

The suction area is made in the same manner as in the annular test section. Both the upper and the lower power clamps are movable for the whole length of the tube. The wall is provided with holes for needle contact probes and tubes for pressure-drop measurements.

The tubular test section 10 is constructed in the same way as test section 20.

3.1.4. Power Supplies

The electrical power to the test sections and steam generator is delivered from two 250 kW thyristor-controlled dc power supplies and one 165 kW vario transformer.

The dc power supplies are ASEA type YMVD, giving 100 V, 2500 A each. Because of severe problems with electric noise in the measuring channels, it was necessary to install two filter-inductances to reduce the superimposed ac-components from these supplies. (Cf. Cortzen (1976)). Each of the filters has an inductance of 150 μH at 250 A and 34 μH at 2500 A.

3.1.5. Pressure-Drop Measurement Equipment

The axial pressure gradient in the test sections was determined by means of electric differential pressure transducers (dp-cells), type Rosemount model 1151 DP.

The pressure range is -10 kPa to + 190 kPa with an accuracy of ± 0.5 kPa.

In the annular test sections, there are 8 pressure taps placed 0.5 m apart. The upper pressure tap is placed immediately below the outlet, the lowest 3.5 m below. The partial pressure drops between the taps and the total pressure drop were measured by means of 8 dp-cells.

In the tubular test sections, the pressure taps located from the outlet and down to 1.0 m below are placed 0.25 m apart. From 1.0 m to 4.0 m below, the distance between the taps is 0.5 m. Thus, in the tubular test section, 1 total and 10 partial pressure drops were measured.

To eliminate bubbles of steam in the pressure drop tubes, a stainless steel canister was connected to each pressure tap.

3.1.6. Film Thickness Measurement Equipment

In periods 5 and 6 the film thickness was determined by means of needle contact probes (cf. Jensen et al. (1971)).

The needle is a 148 mm long stainless steel wire with a diameter of 0.5 mm (cf. fig. 3.6). It is encased in a tube of Degussit, a ceramic material. The Degussit tube with the needle is encased in a tunnel of stainless steel sheet. At the end opposite to the needle tip, the sheet is soldered to a brass cylinder with a fine thread, which fits into a bushing mounted on the outer wall of the test section. A finger screw is fastened at the other end of the cylinder.

By means of the finger screw the distance between the needle tip and the wall of the test section can be adjusted. This distance is measured by means of an electronic distance transducer. The accuracy of this measurement is ± 5μm. The needle contact time, i.e. the time that the needle tip is in contact with the water film, is determined by means of the equipment shown schematically in fig. 3.7. (Cf. Jensen et al. (1971)).

3.1.7. Burnout Detectors

Burnout was detected by means of a bridge detector, type 4819C (AB Atomenergi, Sweden). The resistance of the heated test section from the outlet to 0.2 m below the outlet is compared with the resistance from 0.2 to 0.4 m below. When burnout occurs, the resistance of the upper part suddenly increases due to the temperature excursion. The difference in the two resistances is detected by the device, and the electrical power is decreased manually or shut off automatically by the control system.

3.2. Experimental Procedures

A short description of the experimental procedures is given in this section.

The majority of the experimental data was detected and processed on-line by a PDP 11/05 computer with scanner (logger). The data processing, carried out on-line, is also described in this section.

3.2.1. Measurements of the Main System Parameters

When the main loop was in normal operation, the following main system parameters were shown on the screen connected to the computer while the experiment was running:

p (bar), the system pressure (in the condenser).

Q_0 (kW), the electrical power on the steam generator (pre-heater).

Q_1 (kW), the electrical power on the rod in the annular test sections.

Q_2 (kW), the electrical power on the tube in the test sections.

m (kg/s), the flow rate through the test section.

T_0 (^oC), the inlet temperature to the steam generator (pre-heater).

T_1 (^oC), the inlet temperature to the test section.

T_2 (^oC), the outlet temperature from the test section.

x_{out} (%), the steam quality at the outlet.

The system pressure was measured by a dp-cell (Shoppe & Faeser) with an accuracy of ± 0.2 bar.

The electrical powers Q_0, Q_1 and Q_2 were determined by measuring the voltage and current separately. Due to the oddly shaped output from the thyristor regulated dc power supplies, it was necessary to construct two true rms devices for determination of the power. They were tested against two commercial equipments, and it was found that the deviations were within the accuracy of the instruments (±2%).

The flow rate through the test section was determined by means of a venturi connected to a dp-cell. The flow range from 0.03 to 1.2 kg/s was covered by means of two venturis and two dp-cells. The venturis were calibrated within an accuracy of ±2%.

The temperatures were measured by means of cromel-alumel thermocouples, calibrated within an accuracy of ±0.2^oC.

The steam quality at the outlet was calculated from

$$x_{out} = \frac{Q_0}{mr_{ev}} - \frac{h_2-h_0}{r_{ev}} \qquad \text{(adiabatic)} \qquad (3.1)$$

for adiabatic experiments, and

$$x_{out} = \frac{Q_1+Q_2}{mr_{ev}} - \frac{h_2-h_1}{r_{ev}} \qquad \text{(diabatic)} \qquad (3.2)$$

for diabatic experiments.

Here h_i (J/kg) is the enthalpy of the water at temperature T_i, and r_{ev} (J/kg) is the evaporation heat at the saturation temperature T_{sat}.

The measurements of the main system parameters were frequently checked by means of a single-phase heat balance. This was established by comparing the electrical power Q_1+Q_2 with the thermal power:

$$Q_{th} = m\ (h_2-h_1). \qquad (3.3)$$

To prevent subcooled boiling, this comparison was always carried out with T_2 at least $50^{\circ}C$ below T_{sat}. The discrepancy between the two powers was always less than 3%.

The measurements reported in the following sections were performed within the following intervals of the main system parameters:

p	$= p_{nom}$	$\pm$ 0.5 bar
Q	$= Q_{nom}$	$\pm$ 1%
m	$= m_{nom}$	$\pm$ 2%
T	$= T_{nom}$	$\pm$ 0.5°C
x_{out}	$= x_{out,nom}$	$\pm$ 0.005

where subscript nom denotes nominal value.

3.2.2. Film Flow Measurements

The film flow measurements were initiated by activating the heat balance unit. This was done by opening the by-pass valve V1. The suction rate was then regulated to the desired value by means of a valve at the most suitable primary flowmeter.

Before a two-phase heat balance was carried out, it was checked that the levels in the heat exchanger and regenerator, as well as all the temperatures, were in the steady-state condition. This was done by simultaneously monitoring the differences T_5-T_6 and T_3-T_4 (cf. fig. 3.2).

When the steady state was achieved, the following dimensionless heat balances were made for test purposes:

$$HB_{reg} = \frac{h_2-h_3}{h_7-h_8} \tag{3.4}$$

$$HB_{h.ex.} = \frac{m_p}{m_s}\frac{h_3-h_4}{h_5-h_6} \tag{3.5}$$

where m_p (kg/s) is the (primary) suction rate and m_s (kg/s) is the (secondary) cooling rate.

The heat balance on the regenerator, HB_{reg}, is theoretically unity when water only is sucked off the test section.

The heat balance on the heat exchanger, $HB_{h.ex.}$, becomes theoretically unity when all the steam in the suction mixture is condensed in the regenerator. This is supposed to be fulfilled when the difference T_2-T_3 is greater than 50^oC. In these cases, the values of $HB_{h.ex.}$ was always within the range 0.95-1.05.

The steam flow in the suction mixture, m_g, is then calculated by means of

$$m_g = ((h_5-h_6)m_s+(h_7-h_8)\ m_p - (h_2-h_4)m_p)/r_{ev}. \tag{3.6}$$

If all the steam is condensed in the regenerator, it is seen from eq. (3.5) that

$$m_g = \frac{m_p}{r_{ev}}\ (h_7-h_8-(h_2-h_3)). \tag{3.7}$$

Due to the smaller number of parameters in the latter equation, m_g was determined by eq. (3.7) when the difference T_2-T_3 was greater than 50^oC.

The liquid flowrate in the mixture, m_l, was now determined by

$$m_l = m_p-m_g. \tag{3.8}$$

For each adjustment of the total suction rate, three measurements of m_g and m_l were carried out. The mean values were then plotted in the suction diagram where m_l/m is shown versus $x_{out}-m_g/m$. The total suction rate was then varied until a sufficient number of points was obtained to draw a suction curve. A typical example is shown in fig. 3.9.

The time spent on determining one suction curve was 2-4 hours, depending on the number of points and the stabilization time in the regenerator and steam generator.

3.2.3. Pressure Drop Measurements

The pressure drops were measured when the suction curve was determined and the by-pass valve V1 was closed.

The dp-cells were scanned 10 times each, and the minimum, maximum and mean values were printed out. The extremum values differed generally less than 10% from the mean values. The mean value of the total pressure drop was compared with the sum of the mean values of the partial pressure drops. The difference was less than 5%.

When the diabatic experiments were carried out, the inlet temperature T_1 was so adjusted that the nominal outlet steam quality was found in the midpoint between the two upper pressure taps.

3.2.4. Film Thickness Measurements

The determination of the film thickness was initiated by an estimation of the trigger level made by means of a Hewlett Packard 3721A correlator to show the probability density of the needle signal. A typical example is shown in fig. 3.8.

Ideally, this figure should only consist of two sharp peaks: one representing the contact situation, and the other, at zero voltage, representing the switched-off situation. However, due to capacitive couplings in the measuring system, this was not the case. It was therefore necessary to choose a signal level under which the needle is supposed not to be in contact with the film. It was found most reasonable to determine the trigger level V_t as shown in the figure.

The trigger level was determined for approximately 5 different distances of the needle to the wall, and a mean value was selected.

The contact time was then determined for approximately 30 different positions of the needle. The measuring time was 10 seconds for each position. The contact time, in per cent of the total measuring time, was then plotted versus the needle distance from the wall. Typical examples are shown in figs. 3.30 and 3.31.

3.2.5. Measurements of Wave Frequency and Velocity

Besides being used for the determination of the film thickness, the needle contact probes were also used to measure the frequency and velocity of the roll waves on the film. (Cf Whalley, Hewitt, Hutchinson (1973)).

By means of the Hewlett Packard 3721A correlator, an autocorrelation of the signal from one needle was recorded. The correlation was then processed by a Hewlett Packard 3720A spectrum display to obtain the power spectrum of the signal.

The signals from two needles, mounted 0.5 m apart, were then cross-correlated using the 3721A correlator.

Typical examples of correlations and power spectra are shown on figs. 3.35 and 3.36.

3.3. Experimental Data

A summary of the experiments is given in table 3.2. This lists the test sections, the main system parameters and the measurements carried out in the experimental periods.

In the table, the diabatic length L_d refers to the distance between the inner sides of the power clamps. The adiabatic length L_a is the distance between the inner side of the upper power clamp and the lower end of the suction area. In the adiabatic experiments this length is identical to the total length of the test section.

The majority of the data obtained are reported graphically in this section. A complete list of the data is given in tabular form in Appendix.

3.3.1. Film Flow Rates

The film flow rates are estimated from suction curves, which are obtained as described in sect. 3.2.2. In fig. 3.9 an example of a suction curve is shown. Two straight lines are drawn through the measuring points. The line with the slope s_c is assumed to represent the situation where droplets are sucked off the core. The intersection of this line with the line $m_g = 0$ ($x_{out}-m_g/m = x_{out}$) is assumed to represent the film flow rate m_f. In this figure and in the tables the film flow rate is designated $m_{f,max}$.

The line with the slope s_w is assumed to represent the case where waves on the film are sucked off. Thus the intersection

Table 3.2. Summary of the Experiments

					Main System Parameters				Experiments				
Exp. Per.	Dates	Test Section	Test Conditions	Run Nos.	System Press.	Mass Flux	Diabatic Length	Adiabatic Length	Film Flow	Press. Drop	Burn-out	Film Thick.	Wave Meas.
	1977	-		-	bar	kg/m^2s	m	m					
1	24/1-29/3	17/26S	Diabatic	101-126	70	500-1000	3.5	0.1	x	x			
2	2/5-7/7	10	Adiabatic	201-281	30-90	500-3000	-	9.0	x	x			
3	18/7-16/8	10	Diabatic	301-345	30-90	500-3000	2.0-6.0	0.1	x	x			
3	5/9-8/9	10	Diabatic	346-356	30-90	500-3000	4.0	0.5	x				
3	17/8-25/8	10	Diabatic	357-368	30-90	500-3000	4.0	1.0	x				
3	25/8-1/9	10	Diabatic	369-379	30-90	500-3000	4.0	2.0	x				
4	10/8	10	Diabatic	401-406	70	500-3000	2.0	-			x		
4	14/7-18/7	10	Diabatic	407-454	30-90	500-3000	4.0	-			x		
4	4/8-8/8	10	Diabatic	455-466	70	500-3000	6.0	-			x		
4	10/8	10	Diabatic	467-471	70	1000-3000	8.0	-			x		
5	20/9-4/11	17/26L	Adiabatic	501-529	30-90	500-2000	-	8.0	x	x		x	x
6	14/11-30/12	20	Adiabatic	601-621	70	500-2000	-	9.0	x	x		x	x

with the line $m_g = 0$ represents the flow rate of the film if no waves were present. This flow rate is denoted $m_{f,min}$.

The slope s_c is related to $x_{c,s}$, the steam quality in the core near the wall:

$$x_{c,s} = \frac{1}{1+s_c} \quad . \tag{3.9}$$

When no slip is assumed between the gas (steam) and the droplets, the void fraction in the core near the wall is given by

$$\alpha_{c,s} = \frac{\rho'}{s_c+\rho'} \tag{3.10}$$

where

$$\rho' = \frac{\rho_l}{\rho_g} \quad . \tag{3.11}$$

Under the no-slip assumption, the mean void fraction in the core can be calculated from

$$\alpha_{c,m} = \frac{\rho' x}{m_e/m+\rho' x} \quad , \tag{3.12}$$

where m_e(kg/s) is the flow rate of the entrained liquid:

$$\begin{aligned} m_e &= m-m_g-m_f \\ &= m(1-x-m_f/m) \quad . \end{aligned} \tag{3.13}$$

In the case of an annular geometry, m_f denotes the total film flow rate:

$$m_f = m_{f1}+m_{f2} \tag{3.14}$$

where m_{f1} (kg/s) is the film flow rate on the rod and m_{f2} (kg/s) is the film flow rate on the tube wall.

In the tables A1-A8 in Appendix, $\alpha_{c,s}$ is compared with $\alpha_{c,m}$ by:

$$\frac{\Delta\alpha}{\alpha_{c,s}} = \frac{\alpha_{c,m}-\alpha_{c,s}}{\alpha_{c,s}} \quad . \tag{3.15}$$

From the tables it is seen that there is a tendency to an in-

crement of the difference when G increases. This is supposed to result mainly from the non-infinite size of the suction area. When the gas velocity, and thereby the velocity of the droplets, increases, a greater fraction of the droplets avoids the suction chamber because of the inertia of the droplets.

The slope s_w can be used to estimate the void fraction in the wave region:

$$\alpha_w = \frac{\rho'}{s_w+\rho'} \quad . \tag{3.16}$$

Here it is assumed that there is no slip between the gas and the liquid (waves and droplets) in the wave region.

In the tables, the film flow rates $m_{f,min}$ and $m_{f,max}$ are given as well as the slopes s_c and s_w. The suction curves can be estimated from these four parameters. In some cases no waves could be detected on the film so only s_c could be estimated. In other cases, the suction curves were incomplete so it was impossible to estimate s_c and $m_{f,max}$.

3.3.1.1. Adiabatic Data. The conditions for the adiabatic experiments were chosen in such a way that the data can be regarded as equilibrium data. True equilibrium can never be obtained as the pressure gradient cannot be zero. However, all the reported data fulfil the equilibrium criterion suggested by Hutchinson and Whalley (1973):

$$(L_a/r_h > 300) \wedge (p/(dp/dz)_{tot} > 20m) \tag{3.17}$$

where r_h(m) is the hydraulic radius of the test section and $(dp/dz)_{tot}$(kPa/m) is the total axial pressure gradient.

In figs. 3.10.a-d, the value of m_f/m is plotted versus x_{out} with G as parameter for test section 10 at 30, 50, 70 and 90 bar. The measurements for test section 20, which were performed at 70 bar only, are shown in fig. 3.11. It is seen that m_f/m decreases with the diameter, when p, G and x_{out} are kept constant. This is also shown in figs. 3.12.a-c, where the measurements are compared with other available data. In figs. 3.12.a-b the film flow rates are compared with the data obtained by Singh et al. (1969). The inner diameter of the tube was 12.5 mm and the length approximately 2.5 m. The comparison shown in fig. 3.12.c is between

interpolated values of the present results and the film flow rates reported by Keeys, Ralph and Roberts (1970). The test section was in this case 3.66 m long and the inner diameter 12.7 mm. All three figures adequately show the influence of the geometry.

The results of the measurements carried out in the annular test section 17/26L are shown in figs. 3.13 and 3.14. The film flow rates on the rod, m_{fl}, are shown in figs. 3.13.a-d for p = 30, 50, 70 and 90 bar. The corresponding values for the tube film are plotted in figs. 3.14.a-d. It is seen that the tube film carries more liquid per unit perimeter than the rod film. This asymmetry was also reported by Moeck (1970). His equilibrium experiments were carried out with an annulus where d_1 = 0.0197 m, d_2 = 0.0238 m, and L_a = 2.9 m. The effect of this narrower geometry is shown in fig. 3.15. As in the tubular case, it is seen, that the fraction of entrained liquid increases with the hydraulic diameter.

3.3.1.2. Diabatic Data for Test Section 10. The diabatic measurements listed in table A3 are performed to obtain information on the influence of the heat flux on the film. These experiments were carried out with a subcooled inlet to the diabatic length, i.e., $\Delta T_{sub} = T_2 - T_1 > 0$. In order to investigate if the degree of subcooling could have any significant effect on the film, the diabatic length was varied between 2,4 and 6 m. This was done by moving the lower power clamp while the upper was fixed. The distance between the inlet of the test section and the lower power clamp was, however, always greater than 2.5 m. This should guarantee that a fully developed single-phase flow always was achieved at the initial point of the diabatic length.

Besides the experimental values of $m_{f,min}$, $m_{f,max}$, s_c and s_w, predicted values of burnout steam qualities are also included in table A3. These predicted values of x_{BO} have been evaluated from the burnout results reported in sect. 3.3.3. For each value of L_d, p and G, the burnout power Q_{BO} was estimated for a subcooling of 10°C and 100°C. These experimental values are denominated Q_{BO} (10°C) and Q_{BO} (100°C).

The values of Q_{BO} at the subcooling ΔT_{sub} was then evaluated under the assumption that Q_{BO} is a linear function of $\Delta h_{sub} = h(T_2) - h(T_1)$:

$$Q_{BO}(\Delta T_{sub}) = \frac{Q_{BO}(100^{\circ}C)-Q_{BO}(10^{\circ}C)}{h(T_2-10^{\circ}C)-h(T_2-100^{\circ}C)} \left(h(T_2-10^{\circ}C)-h(T_2-\Delta T_{sub})\right) + Q_{BO}(10^{\circ}C) \qquad (3.18)$$

The validity of this assumption has been demonstrated by Jensen and Mannov (1974). x_{BO} was then calculated from eq. (3.2).

For L_d = 2.0 m, only Q_{BO} (10°C) was measured, so it was necessary to extrapolate from the results for L_d = 4 and 6 m to obtain Q_{BO} (100°C). The values of x_{BO} evaluated from these extrapolations are shown in brackets in the table.

For G = 500 kg/m^{2}s, it is seen that x_{BO} exceeds 100%. This obviously incorrect result arises, however, from the burnout measurements (cf. table A14), and is therefore not a consequence of the assumption (3.18). (Cf. sect. 3.3.3.).

In figs. 3.16.a-f the measured film flow rates are shown. In figs. 3.16.c-e it is seen that L_d has no significant influence on the measurements. Thus it can be concluded that the film flow rate is independent of the subcooling. This is, of course, only true when the subcooling is positive so that no steam is present at the inlet to be heated length.

The figures also show that the burnout measurements give reasonable values for the steam quality, where the film flow rate becomes zero. The exception for G = 500 kg/m^{2}s will be discussed in sect. 3.3.3.

The influence of the heat flux and the boiling length is shown in fig. 3.17. Here are also some of the adiabatic results, (where the boiling length is 9 m), plotted for q" = 0. Notice that the film flow rate for low values of x_{out} increases with the heat flux. This relationship is supposed to be due to the decrement in the boiling length when the heat flux is increased. Thus the increment in m_f is interpreted as a hydrodynamic effect of a shorter developing length. At high heat fluxes, the entrainment rate is supposed to increase due to bursting of bubbles from the film surface (cf. section 4.2.2). Therefore, it is likely that the above mentioned tendency cannot hold for high heat fluxes, so a maximum value must be reached. An example of such an extremum is shown in fig. 3.17b for x_{out} = 24%.

The film flow measurements listed in tables A4-A6 are performed with an adiabatic length of 0.5, 1.0 and 2.0 m. This was carried out by moving both upper and lower clamps while the distance between them was fixed. The purpose of these measurements was to investigate how rapidly the equilibrium situation was achieved after the diabatic length. Some of the results are shown in fig. 3.18. Again it is seen that, for low values of x_{out}, the diabatic film flow rate exceeds the adiabatic.

3.3.1.3. Diabatic Data for Test Section 17/26S. This set of diabatic measurements was basically performed to investigate the influence on the film of the relative distribution of heat flux on the two walls. In figs. 3.19.a-b some of the measurements of film flow rates are shown versus the outlet quality. A comparison is made with some of the measurements reported by Jensen and Mannov (1974). These measurements were carried out in the same test section, but at the high pressure water loop at the Royal Institute of Technology in Stockholm. The good agreement observed checks the measuring system and gives an impression of the reproducibility of the measurements.

To illustrate the transition from the slug flow regime, a few measurements were carried out at very low outlet steam qualities. These measurements for G = 1000 kg/m^{2}s, $q_1" = q_2" =$ 45 W/cm^2, show that the entrainment increases when the slug flow regime is approached. Furthermore, it is indicated that the ratio between the film flow rates per unit perimeter tends to unity when x_{out} tends to zero.

The influence of the relative heat flux distribution on the rod and tube wall is shown in figs. 3.20.a-b. The corresponding adiabatic values from table A7 are also included. The other data in table A1 show similar deviations from the adiabatic, equilibrium film flow rates.

3.3.2. Axial Pressure Gradients

The axial pressure gradients are determined from the pressure drop measurements described in sect. 3.2.3.

The pressure drop measured between the pressure taps i and i+1 is designated Δp_i. The total axial pressure gradients in the midpoints between the taps are determined by subtraction of the

difference in hydrostatic head in the two pressure tubes that connect the taps to the dp-cells. The mean temperature of the water in these tubes is measured to about $30^{o}C$. Thus we find

$$\left(\frac{dp}{dz}\right)_{tot}(z_{mi}) = \frac{\Delta p_i - \rho_l(30^{o}C)\,g(z_{i+1}-z_i)}{z_{i+1}-z_i} \tag{3.19}$$

where z_i (m) is the distance from the inlet to pressure tap i, and z_{mi} (m) is the midpoint between z_i and z_{i+1}:

$$z_{mi} = \frac{z_i+z_{i+1}}{2} . \tag{3.20}$$

For the sake of convenience, all pressure gradients are calculated as positive values, even if the pressure in fact decreases with z.

The hydrostatic pressure gradient is calculated from

$$\left(\frac{dp}{dz}\right)_{hyd}(z_{mi}) = g\,(\rho_l(z_{mi})(1-\alpha(z_{mi}))+\rho_g(z_{mi})\alpha(z_{mi})) \tag{3.21}$$

where $\rho_g(z)$ is the gas density at the axial position z.

The acceleration pressure gradient is derived from

$$\left(\frac{dp}{dz}\right)_{acc}(z_{mi}) =$$

$$\frac{G^2}{z_{i+1}-z_i}\left\{\left(\frac{x(z_i)^2}{\rho_g(z_i)\alpha(z_i)} + \frac{(1-x(z_i))^2}{\rho_l(z_i)(1-\alpha(z_i))}\right)\right.$$

$$\left. - \left(\frac{x(z_{i+1})^2}{\rho_g(z_{i+1})\alpha(z_{i+1})} + \frac{(1-x(z_{i+1}))^2}{\rho_l(z_{i+1})(1-\alpha(z_{i+1}))}\right)\right\} \tag{3.22}$$

The frictional pressure gradient can now be calculated:

$$\left(\frac{dp}{dz}\right)_f = \left(\frac{dp}{dz}\right)_{tot} - \left(\frac{dp}{dz}\right)_{acc} - \left(\frac{dp}{dz}\right)_{hyd} . \tag{3.23}$$

It is seen that the estimation of the frictional pressure gradient requires information on how the mean void varies along the channel. Especially for the diabatic data, it is necessary to know the void fraction with very good accuracy, because the acceleration pressure gradient in this case is of the same order as the frictional pressure gradient.

Due to the lack of experimental values for α, it was necess-

ary to use an empirical relationship to estimate the mean void fraction.

In this case we chose the Bankoff-Jones void formula, where the mean slip ratio S is calculated from:

$$S = \frac{1-\alpha}{k_s-\alpha+(1-k_s)\alpha^R} \tag{3.24}$$

with the following constants

$$k_s = k_{BJ}+(1-k_{BJ})p/p_{cr} \tag{3.25}$$

$$R = 3.33 + 0.0026\ \text{bar}^{-1}\cdot p + 0.000097\ \text{bar}^{-2}\cdot p^2 \tag{3.26}$$

$$k_{BJ} = 0.9086\ G/(G+123\ \text{kg/m}^2\text{s}) \tag{3.27}$$

where p_{cr} is the critical pressure 221.2 bar.

The mean void fraction is related to the mean steam quality through the continuity equation (cf. eq. (2.7)):

$$\frac{x}{1-x} = \frac{\alpha}{1-\alpha}\frac{S}{\rho'} \ . \tag{3.28}$$

The mean steam quality at the axial position z is calculated from (cf. eqs. (3.1) and (3.2)):

$$x(z) = \frac{1}{r_{ev}(T_{sat})}\left(\frac{Q_0}{m} - (h(T_{sat}) - h_0)\right) \text{ (adiabatic)} \tag{3.29}$$

$$x(z) = \frac{1}{r_{ev}(T_{sat})}\left(\frac{(Q_1+Q_2)z}{m\ L_d} - (h(T_{sat})-h_1)\right) \text{ (diabatic)} \tag{3.30}$$

where T_{sat} refers to the saturation temperature at z.

It is seen that this void correlation depends neither on the geometry nor on the heat flux. To give an impression of the error this simplification gives, values calculated from eqs. (3.24) - (3.30) are compared with void fractions estimated from eq. (4.24). The latter equation relates the measured film flow rate to the mean void fraction under the assumption of no slip between the gas and droplets in the core. The comparison is illustrated in figs. 3.21.a-b, where the diabatic film flow data from tables A1 and A3 are used to calculate α from eq. (4.24).

The observed good agreement indicates that eqs. (3.24) -

(3.30) can be used to estimate the axial variation of the void fraction, so $(dp/dz)_f$ can be calculated from $(dp/dz)_{tot}$ with reasonable accuracy.

The two-phase friction multiplier ϕ^2 is defined by

$$\phi^2 \equiv \frac{(dp/dz)_f}{(dp/dz)_{f,l}} \tag{3.31}$$

where the single-phase friction pressure gradient $(dp/dz)_{f,l}$ is measured to fit the relationship (cf. Jensen and Mannow (1974)):

$$\left(\frac{dp}{dz}\right)_{f,l} = 0.40 \left(\frac{4\ m}{\rho_l \nu_l \pi (d_1+d_2)}\right)^{-0.25} \frac{G^2}{2(d_2-d_1)\rho_l} \ . \tag{3.32}$$

3.3.2.1. Adiabatic Data. The values obtained for $(dp/dz)_{tot}$, $(dp/dz)_f$ and ϕ^2 are listed in tables A10, A12 and A13 for test-sections 10,17/26L and 20, respectively. To illustrate the variation of the frictional pressure gradient along the channel, two values of $(dp/dz)_f$ are tabulated. The first value is the mean value over the whole length, where pressure drops are measured. This distance is 4 m for the tubular test sections and 3.5 m for the annular test section. The second value is the mean value over the last meter before the outlet. By comparing the two values, it is seen that it is reasonable to assign the frictional pressure gradient at the outlet to the latter value designated $(dp/dz)_f$ (1 m).

The variation of this value with G and x_{out} is shown in figs. 3.22 - 3.24. The influence of system pressure is demonstrated in figs. 3.22.a-d, where $(dp/dz)_f$ in test section 10 is plotted for 30, 50, 70 and 90 bar. The variation with geometry is shown by figs. 3.22.c, 3.23 and 3.24, where the results at 70 bar are plotted for test sections 10, 20 and 17/26L.

3.3.2.2. Diabatic Data. Under diabatic conditions the pressure drops were measured at an outlet steam quality that exceeded the nominal value of x_{out}. This was done so that the pressure gradient at the midpoint between the two upper pressure taps could be estimated at a steam quality equal to (or greater than) the nominal x_{out}. Thus the pressure drop measurements were carried out at a degree of subcooling that differed from that

used for the corresponding film flow measurements. It was therefore necessary to investigate if the subcooling had any significant effect on the pressure drops by varying the inlet temperature. As in sect. 3.3.1.2, it was verified that the measurements were independent of ΔT_{sub} as long as no steam was present at the inlet. Thus it can be concluded that $(dp/dz)_f$ at the outlet can be estimated from measurements of pressure drops below the outlet without introducing any significant error.

Examples of measurements are shown in figs. 3.25 and 3.26 for test sections 10 and 17/26S, respectively. Notice that the frictional pressure gradient decreases when burnout is approached. This feature was also reported by Kirillov et al. (1973), who measured film thickness and pressure drop at o8.6 bar in a tube with an inner diameter of 17 mm (cf. fig. 4.20).

3.3.3. Burnout Powers

The burnout measurements were carried out in test section 10 with fixed values of p, G and ΔT_{sub}. The electrical power, and thereby the outlet steam quality, was increased until burnout was detected as described in sect. 3.1.7. The estimated maximum values of Q_2 and x_{out} are designated Q_{BO} and x_{BO}.

The burnout powers and steam qualities obtained are entered in table A14, where also q''_{BO} is tabulated. It appears that x_{BO} for G = 500 kg/m^{2}s in some cases exceeds 100%. These obviously incorrect results indicate that the sensitivity of the resistance bridge measurement in the burnout detector has been too small. The good agreement between the film flow measurements and burnout steam qualities, which was shown in figs. 3.16.a-f, indicates, however, that this was only the case at G = 500 kg/m^{2}s, where the heat fluxes, and hence the temperature differences, are small.

The results are shown graphically in figs. 3.27-3.29. The influence of subcooling is illustrated in figs. 3.27.a-d. It appears that the subcooling has only little effect on x_{BO}.

The effect of diabatic length is shown in fig. 3.28 that illustrates that x_{BO}, and thereby Q_{BO}, increases with L_d. The burnout heat flux q''_{BO}, however, shows the opposite tendency, which is shown in fig. 4.23.

Figure 3.29 illustrates the influence of system pressure on x_{BO}. Here it is seen that x_{BO} reaches a maximum value in the

interval between 50 and 70 bar. This is, however, not the case for Q_{BO}. From table A14 and fig. 4.22 it appears that the burn-out power decreases with the pressure when ΔT_{sub} is fixed.

3.3.4. Film Thicknesses

The film thickness was measured in test sections 17/26L and 20 under adiabatic conditions as described in sect. 3.2.4. In the annulus only the thickness of the rod film could be measured.

Examples of needle contact time curves are shown in figs. 3.30 and 3.31. Here the contact time τ_{con} is plotted versus the distance y from the wall to the needle tip. It is seen that the minimum contact time τ_{min} is greater than zero in the annular test section. This indicates that the films on the rod and tube wall are forming bridges across the narrow gap.

The mean film thickness is evaluated from

$$\delta = \frac{1}{1-\tau_{min}} \int_0^{y(\tau_{min})} \tau_{con}(y)\,dy \qquad (3.33)$$

and the values are entered in tables A15 and A16.

The needle distances where τ_{con} is 10, 50 and 90 per cent are also included in the tables. It appears that y(10%) is approximately twice the mean film thickness and 10 times y(90%). This observation agrees well with Hutchinson, Whalley and Hewitt (1973), who report that the ratio between the amplitude and the mean film thickness in air-water systems is about 5. From table A15 it is also seen that τ_{min} tends to zero when δ decreases, which supports the theory of the formation of bridges across the annular gap.

The measured values of the mean film thickness are plotted versus the steam quality in figs. 3.32 and 3.33. In fig. 3.34 the results of similar experiments carried out by Kirillov et al. (1973) are shown. These measurements were performed in a 17 mm tube at 68.6 bar. By comparing figs. 3.33 and 3.34, it is seen that the film thickness increases with the diameter. However, it seems that the influence is overestimated, especially at smaller film thicknesses. This overestimation is supposed to be due to an adjustment error in the present measuring equipment. It appeared that the estimation of the film thickness was

very sensitive to the choice of the trigger level V_t (cf. fig. 3.8). Thus a variation of V_t on 10% could give up to 50% difference in the estimated value of δ. As a result of this relationship, the uncertainty of the present measuring method is believed to be up to 50%.

3.3.5. Wave Frequencies and Velocities

In sect. 3.2.5 it was mentioned that the frequency and the velocity of the roll waves are estimated from auto- and cross-correlations of the needle signals. The auto-correlation was Fourier-transformed by the spectrum display to obtain the power spectrum $S_v(f)$. Examples of power spectra are shown in fig. 3.35. It was shown by Webb (1970) that the peak in a power spectrum corresponds to the wave frequency measured by manual counting of peaks on a trace of the time-varying film thickness. This wave frequency f_w, together with the frequency range Δf_w over which the power density is more than half of the maximum value, is entered in tables A15 and A16. It is seen that f_w increases and Δf_w becomes broader when the film thickness decreases. At the smallest values of δ it was impossible to determine values of f_w and Δf_w because the intensity of the auto-correlation was too small.

Examples of the cross-correlation $C_v(t)$ of signals from two needles 0.5 m apart are shown in fig. 3.26. Webb (1970) also showed that the position of the largest peak in a cross-correlation corresponds to the time taken for a wave to pass between two probes. Thus the wave velocity v_w (m/s) can be found from

$$v_w = \frac{L_n}{T_w} \tag{3.34}$$

where L_n(m) is the distance between the needles and T_w (s) is estimated from the cross-correlations.

The wavelength λ_w(m) and the wavenumber k_w(m^{-1}) can now be calculated:

$$\lambda_w = v_w/f_w \tag{3.35}$$

$$k_w = 2\pi/\lambda_w \tag{3.36}$$

The values of λ_w obtained are plotted versus δ in figs. 3.37-3.38. The figures indicate a proportionality between λ_w and δ:

$$\lambda_{w1} \approx 700\delta_1 \quad \text{(test section 17/26L)} \tag{3.37}$$

$$\lambda_w \approx 200\delta \quad \text{(test section 20)} \tag{3.38}$$

Tatterson, Dallman and Hanratty (1977) assumed that λ_w was proportional to δ in their theory of droplet sizes in annular flow. They concluded that such a relationship was compatible with the fact that the wavelength is much greater than the film thickness.

The measurements of f_w and T_w were normally carried out at a needle distance corresponding to y(50%). It should, however, be noticed that only the intensity of the auto- and cross-correlations was affected by the needle distance, whereas the values of f_w and T_w were independent of y. This was also the case in the annular geometry at large needle distances, where the needle tip was assumed to be present in the tube film (cf. fig. 3.30). Because the film flow per unit perimeter for the tube is greater than for the rod, it is assumed that δ_2 is greater than δ_1. This indicates that the relationship between λ_2 and δ_2 for the tube film in the annulus differs from the relationship shown in fig. 3.37 for the rod film. However, as a result of the lack of experimental values of δ_2, it was impossible to estimate this lower ratio and compare it with the value from eq. (3.38) for the tubular case. Nevertheless, in the analytical part of this report, the film thickness is related to the experimental film flow rate.

4. ANALYTICAL PART

The analytical part of this report is divided into four sections. The first two sections deal with tubular geometries. First is presented a model which, on the basis of the experimental data, describes the adiabatic, equilibrium annular flow. In the second section, the diabatic film flow data are analyzed, and equations for the calculation of burnout are set up. In the

last two sections, the model is extended so that adiabatic and diabatic film flow and burnout in annuli can be calculated. Each section is concluded with comparisons between experiments and predictions.

4.1. Equilibrium Conditions in Tubular Geometries

The equilibrium condition, characterized by constant velocities, film flow rates, film thicknesses, etc., is achieved in an adiabatic tube of sufficient length (cf. eq. (3.17)). For flow velocities and film thicknesses large enough to cause liquid to be entrained in the gas core, this equilibrium is independent of the inlet condition. This is assumed to be achieved for the adiabatic data presented in sect. 3.3.

This section presents a set of equations that permit the calculation of the equilibrium condition. All equations are "microscopic", i.e., they describe basic processes or conditions (unlike correlations for, e.g., pressure drop or void). Some of the empirical relationships will be obtained through analysis of the adiabatic data.

4.1.1. Shear Stress

Because of the uniformity of the static pressure across the tube, the shear stress on the wall τ_w(N/m^2) becomes:

$$\tau_w = \left(\frac{dp}{dz}\right)_f \frac{r_2}{2} \quad . \tag{4.1}$$

The interfacial shear stress, i.e., the shear stress at the film surface is denoted τ_i(N/m^2):

$$\tau_i = \left(\frac{dp}{dz}\right)_f \frac{r_{i2}}{2} \tag{4.2}$$

where the interfacial radius r_{i2}(m) is given by

$$r_{i2} = r_2 - \delta. \tag{4.3}$$

4.1.2. Velocity Profile in the Film

In the present film flow model Prandtl's universal, turbulent, two-layer model is used to describe the velocity distribution in the film.

Here the dimensionless velocity u_l^+ is:

$$u_l^+ = u_l/u_l^* , \tag{4.4}$$

where u_l(m/s) is the velocity in the film and u_l^*(m/s) is the shear velocity:

$$u_l^* = \sqrt{\tau_w/\rho_l} , \tag{4.5}$$

related to the dimensionless wall distance y^+:

$$y^+ = yu_l^*/\nu_l \tag{4.6}$$

where y(m) is the distance from the wall:

$$y = r_2 - r. \tag{4.7}$$

The two-layer model is given by (cf. Schlichting (1968)):

$$u_l^+ = \begin{cases} y^+ & y^+ \leq y_{tr}^+ \text{ (laminar)} \\ \frac{1}{\kappa} \ln y^+ + B & y^+ > y_{tr}^+ \text{ (turbulent)} \end{cases} \tag{4.8}$$

where κ is von Kármán's constant:

$$\kappa = 0.4. \tag{4.9}$$

The value corresponding to smooth tubes is chosen for the roughness function B:

$$B = 5.5. \tag{4.10}$$

The transition between the laminar and the turbulent regions is assumed to take place at:

$$y_{tr}^+ = 11.5. \tag{4.11}$$

From the velocity profile, the interfacial velocity, i.e. the velocity at the film surface, u_i(m/s), is derived:

$$u_i = u_1(y = \delta). \tag{4.12}$$

Integration of the velocity profile yields:

$$Re_f = \frac{m_f}{2\pi r_2 \mu_1} = \int_0^{\delta^+} u_1^+ \, dy^+ \tag{4.13}$$

where

$$\delta^+ = \delta u_1^*/\nu_1. \tag{4.14}$$

Thus the consequence of the existence of a universal film velocity profile is a unique relationship between the dimensionless film thickness δ^+ and the film Reynolds number Re_f:

$$\delta^+ = \begin{cases} \sqrt{2Re_f} & Re_f \leq Re_{f,tr} \\ \dfrac{Re_f + C(\kappa, B, y_{tr}^+)}{\frac{1}{\kappa}(\ln \delta^+ - 1) + B} & Re_f > Re_{f,tr} \end{cases} \tag{4.15}$$

where

$$C(\kappa, B, y_{tr}^+) = y_{tr}^+ (\tfrac{1}{\kappa}(\ln y_{tr}^+ - 1) + B - \tfrac{1}{2} y_{tr}^+) = 38.592 \tag{4.16}$$

and

$$Re_{f,tr} = \tfrac{1}{2}(y_{tr}^+)^2 = 66.125. \tag{4.17}$$

This set of equations enables us to calculate the mean film thickness when the film flow rate and the frictional pressure gradient are known. This calculation has been carried out for the data where experimental values of the film thickness are available. This is the case for the present data from test section 20 and 17/26L. The relationships between δ_1^+ and Re_{f1} for the rod film in the annular geometry are similar to the relationships presented above for tubes (cf. sect. 4.3.2).

The comparison between the experimental and the theoretical values is shown in fig. 4.1. It is seen that the experimental

value exceeds the theoretical for large film thicknesses and vice versa for small film thicknesses. This discrepancy is supposed to be mainly due to the adjustment error in the film thickness instrumentation discussed in sect. 3.3.4.

The above assumption is supported by the comparison shown in fig. 4.2, where another set of experimental and theoretical values of film thicknesses is plotted. These data were obtained from Whalley, Hewitt and Hutchinson (1973), who measured film flow rates, pressure drops and film thicknesses in a tube (r_2 = 15.9 mm, l = 18.9 m) with air-water at 2-4 bar. The thickness of the film was measured by a conductance probe method (cf. Webb (1970)). The probe consisted of two 3.2 mm diameter rods, and an attempt was made to set these flush with the tube wall 12.7 mm apart. However, because the probe rods were not quite flush with the wall, a zero error appeared. Thus the smallest film thickness which could be measured was approximately 90 μm.

When the zero error is taken into account, the comparison in fig. 4.2 illustrates a good agreement between δ_{exp} and δ_{th}. It is therefore assumed that the universal, turbulent, two-layer model reasonably describes the velocity profile in the film.

4.1.3. Velocity Profile in the Core

The velocity distribution in the gas core is assumed to obey the turbulent logarithmic profile (Schlichting (1968)):

$$u_g(r) = u_i + u_g^* \left(\frac{1}{\kappa} \ln \frac{r_{i2} - r}{k_S} + B\right) \tag{4.18}$$

where k_S(m) denotes the equivalent sand roughness and u_g^*(m/s) is the friction velocity for the gas core:

$$u_g^* = \sqrt{\tau_i/\rho_g} \ . \tag{4.19}$$

The value for completely rough walls is chosen for the roughness function B:

$$B = 8.5. \tag{4.20}$$

The measurements presented by Gill, Hewitt and Lacey (1963) and Kirillov et al. (1973) confirm that a logarithmic law describes the gas velocity profile in annular two-phase flow adequately well. The measurements indicate, however, that κ does not (as in single-phase flow) remain constant. This is illustrated in fig. 4.3 where the measurements of κ made by Kirillov et al. are plotted versus the experimental film thickness. The correlation shown indicates that the roll waves on the film (not the droplets in the core) are responsible for the decrement of the turbulence constant. This was also suggested to be the most likely explanation by Gill, Hewitt and Lacey. Their air-water measurements also showed that κ lies in the interval 0.2-0.4. It was, however, impossible to correlate their values to the film thickness. Because of this lack of a consistent way to correlate the two sets of data, it was decided to apply the classical constant value of κ in eq. (4.18):

$$\kappa = 0.4. \tag{4.21}$$

The mean gas velocity is obtained by :

$$\bar{u}_g = \frac{2}{r_{i2}^2} \int_0^{r_{i2}} u_g(r) r \, dr \, . \tag{4.22}$$

On the other hand, we have (cf. eq. (2.5)):

$$\bar{u}_g = \frac{Gx}{\rho_g \alpha} \, . \tag{4.23}$$

If no slip is assumed between the gas and the droplets, the mean void can be calculated from

$$\alpha = \left(\frac{r_{i2}}{r_2}\right)^2 \frac{m_g/\rho_g}{\frac{m_g}{\rho_g} + \frac{m_e}{\rho_l}} \, . \tag{4.24}$$

The adequacy of this assumption has already been demonstrated in figs. 3.21.a-b where comparisons were made between void frac-

tions calculated from the Bankoff-Jones void formula (eq. (3.24)) and eq. (4.24).

By means of the experimental values of the film flow rate and the frictional pressure gradient, the equivalent sand roughness, k_s, can now be estimated from eqs. (4.1)-(4.24). The results of this calculation are shown versus the theoretical film thicknesses in figs. 4.4.a-d for p = 30, 50, 70 and 90 bar, respectively. The figures indicate that the relationship between k_s and δ_{th} is slightly dependent on the system pressure. To decide whether or not this indication is significant, similar results from the air-water measurements of Whalley, Hewitt and Hutchinson (1973) are plotted in fig. 4.5. It is seen that these points show the same relationship as the points in fig. 4.4.c for 70 bar. Therefore it is concluded that the above-mentioned tendency is insignificant. Thus all the points in figs. 4.4.a-d and 4.5 are replotted in fig. 4.6, and a general roughness correlation is derived (valid for $\delta_{th} < 800\mu m$):

$$k_s = 0.57\ \delta_{th} + 21.73\cdot10^3 m^{-1}\ \delta_{th}^2 - 38.30\cdot10^6 m^{-2}\ \delta_{th}^3 + 55.68\cdot10^9 m^{-3}\ \delta_{th}^4 \quad (4.25)$$

4.1.4. Mean Droplet Concentration

In the equilibrium situation, the rate of entrainment of the droplets from the liquid film is equal to the rate of deposition of droplets back into the film.

The deposition rate G_D (kg/m^2s) is written as

$$G_D = k_D c \quad (4.26)$$

where k_D (m/s) is a mass transfer coefficient, and c (kg/m^3) is the mean concentration of liquid droplets in the core. When no slip is assumed between the gas and the droplets, c can be calculated from (cf. eq. (3.12)):

$$c = \rho_l\ (1 - \alpha_{c,m}) = \frac{m_e/m}{\frac{m_e/m}{\rho_l} + \frac{x}{\rho_g}} = \frac{m_e}{\frac{m_e}{\rho_l} + \frac{m_g}{\rho_g}} \quad (4.27)$$

Thus in the equilibrium situation we have:

$$G_E = k_D \, c_{eq} \tag{4.28}$$

where G_E (kg/m^2s) denotes the entrainment rate, and subscript eq denotes equilibrium.

Hutchinson and Whalley (1973) showed that values of c_{eq} obtained from air-water experiments correlate with the dimensionless entrainment parameter:

$$S_\delta = \frac{\delta_{th} \tau_i}{\sigma} \, . \tag{4.29}$$

Such a correlation is shown in fig. 4.7 for the equilibrium data obtained by Whalley, Hewitt and Hutchinson (1973). The values of S_δ and c_{eq} are calculated from the film flow and pressure drop data by means of eqs. (3.21), (3.23), (4.1) - (4.24), (4.27), and (4.29).

If k_D is assumed to be a constant, this relationship indicates that the entrainment rate can be characterized by the parameter S_δ. Thus it was argued that the entrainment process is dominated by the competition between the interfacial stress and the containment pressure of a surface dislocation. The latter is given by

$$p_{cont} = \frac{2\sigma}{r_{curv}} \tag{4.30}$$

where r_{curv}(m) denotes the radius of curvature of the surface dislocation. In eq. (4.29) this was assumed to correlate with the film thickness δ_{th}.

In figs. 4.8.a-d, similar correlations are obtained from the present steam-water data.

It is seen that the following relationship describes the correlation adequately well:

$$c_{eq} = \begin{cases} 0 & S_\delta \leq Z_E \\ F_E (S_\delta - Z_E) & S_\delta > Z_E \end{cases} \tag{4.31}$$

where the values of F_E and Z_E are entered in table 4.1.

Table 4.1

Constants in eq.(4.31)

p (bar)	2-4*	30	50	70	90
F_E(kg/m^3)	55	55	75	110	155
Z_E(-)	0.03	0.10	0.15	0.15	0.20

*Air-water mixtures.

From the table it appears that F_E increases with the pressure. If S_δ describes the entrainment process in a reasonable way, this increment must be due to a decrement in the mass transfer coefficient k_D.

The value of k_D was estimated by Cousins and Hewitt (1968) for air-water flow. They found that the mass transfer coefficient was approximately independent of flow conditions, and the value was approximately 0.15 m/s. For steam-water flow at 70 bar, Bennett et al. (1966) estimated the value to be approximately 0.01 m/s. Thus the ratio between F_E for air-water mixtures and steam-water at 70 bar should be about 15. However, from table 4.1 it is seen that the ratio is only 2. Thus it must be concluded that S_δ *does not describe the entrainment* process in a quantitatively correct manner.

The above-mentioned inconsistency was discovered by Whalley, Hewitt and Hutchinson (1973) through comparing their air-water data with the steam-water data of Singh et al. (1969) and of Keeys, Ralph and Roberts (1970). They attempted to overcome the discrepancy by replacing S_δ by the modified entrainment parameter:

$$S_k = \frac{k_s \tau_i}{\sigma} \quad . \tag{4.32}$$

Here the equivalent sand roughness was used instead of the film thickness as length scale for the containment force due to surface tension. This replacement reduced the discrepancy but did not remove it. A similar analysis with the present data and theory gave the same result. When S_k was used as parameter, it also appeared that the points for $\bar{u}_g$ > 20 m/s fell outside the correlating curve. Thus it was indicated that the influence

of the gas velocity on the entrainment process was underestimated. An attempt was therefore made to incorporate $\bar{u}_g$ more closely in the entrainment parameter without introducing further scattering of the points in the correlation. The best result was achieved by means of the following dimensionless group:

$$S_u = \frac{k_S \tau_i \bar{u}_g \mu_l}{\sigma^2} \quad . \tag{4.33}$$

It is seen that the modified entrainment parameter S_k is multiplied by a dimensionless velocity $\bar{u}_g \mu_l / \sigma$. This velocity was also used by Paleev and Filippovich (1966) in their attempt to correlate air-water entrainment data.

The introduction of this new entrainment parameter makes it possible to overcome the above inconsistency in the two sets of data. This is shown in figs.4.9.a-b, where the entrainment rate $G_E = k_D \, c_{eq}$ is plotted versus S_u. The values of k_D used in the estimation of G_E are listed in table 4.2.

Table 4.2

Mass Transfer Coefficients

p (bar)	2-4*	30	50	70	90
k_D (m/s)	0.15	0.021	0.013	0.010	0.006

*Air-water mixtures.

The mass transfer coefficients for p = 30, 50 and 90 bar are in good agreement with a relationship between k_D and σ suggested by Whalley, Hutchinson and Hewitt (1974).

It is seen that the relationship

$$G_E = 2.0 \, S_u \ \text{kg/m}^2\text{s} \tag{4.34}$$

correlates the two sets of data adequately well.

This general entrainment correlation closes the set of equations, and permits us to calculate the equilibrium conditions.

4.1.5. Predictions of Data

The capability of the set of equations presented will now

be demonstrated by comparisons between experimental and calculated values of film flow rates and frictional pressure gradients. Comparisons will be carried out both with the experimental data that were used to evaluate the entrainment and roughness correlations, and with the data that have not been analyzed in the preceding sections.

4.1.5.1. Predictions of Film Flow Rates. In figs.4.10.a-d and 4.11 the calculated values of film flow rates are compared to the adiabatic measurements in test sections 10 and 20. A similar comparison is made for the data reported by Singh et al. (1969) and by Keeys, Ralph and Roberts (1970) in fig. 4.12. It is seen that the agreement is in general good, but that the model overestimates the experimental values for low gas velocities. It should be noted that this was also the case when eq. (4.31) was used instead of eq. (4.34) as entrainment correlation. The main reason for this discrepancy is supposed to be an incorrect interpretation of the suction curves. When the film thickness is large, the shape of the suction curve becomes more rounded than shown in fig. 3.9. This causes a considerable uncertainty in the determination of the film flow rate. The explanation of the disagreement suggested above is supported by the data reported by Nigmatulin, Malyshenko and Shugaev (1976). They measured equilibrium film flow rates in a 13.3 mm tube at 10-100 bar. The results at 50 bar are shown in fig. 4.13, where the predictions are also included. It is seen that the data of these authors for low gas velocities give considerably higher values than those in figs. 4.10-4.12, and that the agreement with the predictions is excellent.

4.1.5.2. Predictions of Frictional Pressure Gradients. In figs. 4.14 and 4.15 the predicted values of $(dp/dz)_f$ are compared to the measurements in test sections 10 and 20. A similar comparison is made for the adiabatic data reported by Kirillov et al. (1973) in fig. 4.16. As was the case for the predictions of the film flow rate, a good agreement is observed except at low gas velocities. Also this discrepancy is supposed to result mainly from the above-mentioned incorrect interpretation of the suction curves at large film thicknesses. The underestimation of the experimental film flow rate at low gas velocities causes a too progressive roughness correlation (eq. (4.25)). This

overestimation of the equivalent sand roughness involves an overprediction of the frictional pressure gradient at large film thicknesses.

4.2. Diabatic Conditions in Tubular Geometries

The equilibrium situation described in the previous sections is never obtained for diabatic flows. The film flow is no longer simply controlled by a balance between deposition and entrainment. The evaporation of the water film to steam complicates the flow conditions.

In this section a mass balance on the film will be set up on the basis of the diabatic data. This enables us to calculate the axial position where the film flow rate vanishes, i.e. where burnout occurs.

4.2.1. Mass Balance on the Film

The total mass flow rate is given by (cf. eq. (2.1)):

$$m = m_f + m_e + m_g. \tag{4.35}$$

In the steady state (m is constant) we obtain:

$$\frac{dm_f}{dz} + \frac{dm_e}{dz} + \frac{dm_g}{dz} = 0. \tag{4.36}$$

When no superheating of the steam or water is assumed, a heat balance yields:

$$\frac{dm_g}{dz} = \frac{\pi d_2 q_2''}{r_{ev}}. \tag{4.37}$$

When all evaporation is assumed to take place in the film, the change in the flow rate of entrained liquid can be written as:

$$\frac{dm_e}{dz} = \pi d_2 (G_E - G_D). \tag{4.38}$$

Thus we find the following mass balance on the film:

$$\frac{dm_f}{dz} = \pi d_2 (G_D - G_E - \frac{q_2''}{r_{ev}}). \tag{4.39}$$

4.2.2. Entrainment and Deposition Rates

It is assumed that the entrainment rate, G_E, can be described, also under diabatic conditions, by eq. (4.34), which was developed from the adiabatic data. Thus it is postulated that the heat flux does not influence the entrainment process. This is presumably incorrect for very high heat fluxes, where the formation of steam inside the film and the bursting of bubbles at the film surface is believed to cause an increment of the entrainment rate (cf. Andersen (1972)). However, this enhancement is supposed to be negligible for the moderate heat fluxes ($q_2" < 200$ W/cm^2) considered here (cf. Andersen and Würtz (1975)).

The evaporation of the film is, however, supposed to diminish the deposition rate. The radial velocity of the steam at the film surface is given by :

$$v_{gi} = v_g(y = \delta) = \frac{q_2"}{r_{ev}\rho_g} . \tag{4.40}$$

This velocity decreases rapidly with y, the distance from the wall. At large film thicknesses, where the amplitude of the roll waves is large, the influence of the perpendicular gas stream on the deposition rate is assumed to be negligible, because the droplets are captured by the waves at relatively large distances from the wall. However, at small film thicknesses, where the film is relatively smooth, it is assumed that the radial gas stream has a significant influence on the mass transfer coefficient. To take some account of this effect, the deposition rate is calculated by

$$G_D = \begin{cases} (k_D - v_{gi}\, e^{-\delta/y_D})c \text{ when } v_{gi}\, e^{-\delta/y_D} < k_D \\ 0 \text{ when } v_{gi}\, e^{-\delta/y_D} \geq k_D \end{cases} \tag{4.41}$$

where a representative value of y_D was estimated from the diabatic film flow data:

$$y_D = 50\ \mu m. \tag{4.42}$$

The influence of incorporating eqs. (4.40) - (4.42) into the model will be demonstrated in sect. 4.2.4.

4.2.3. Initial Condition

The mass balance on the film (eq. (4.39)) can be integrated when the initial conditions are specified. Ideally, these values should represent the onset of annular flow. However, the transition between the churn and annular flow regime is a rather gradual transition (cf. Hewitt and Hall-Taylor (1970)), so the onset is a rather ill-defined concept.

However, Wallis (1969) quotes a value of 80% of the mean void fraction to be representative of the transition. At α=0.8 the influence of the heat flux on the film flow rates is rather small (cf. figs. 3.17 and 3.21), so the following initial condition was chosen:

$$m_f(\alpha = 0.8) = m_{f,eq}(\alpha = 0.8) \qquad (4.43)$$

where the equilibrium film flow rate, $m_{f,eq}$, is calculated from the adiabatic model presented in sect. 4.1.

4.2.4. Predictions of Data

As in the adiabatic case, comparisons between experiments and predictions of film flow rates and frictional pressure gradients will be given. However, in this section predictions of burnout heat fluxes, powers and steam qualities will also be compared to experimental data.

4.2.4.1. Predictions of Film Flow Rates. In figs. 4.17.**a-f** the calculated values are compared to the measurements of film flow rates and the values of x_{BO} that were estimated from the burnout experiments and eq. (3.18). It is seen that the model takes the variation of pressure, heat flux and mass flux into account in a reasonable way.

In fig.4.17.c the calculations performed with $y_D = 0$ (i.e. $G_D = k_D c$) are included. It is verified that the incorporation of eq. (4.41) in the model has a beneficial influence on the predictions of x_{BO} at high mass fluxes, where the mean droplet concentration is large.

As in the adiabatic case, it is supposed that the main reason for the underprediction of the film flow rates at G = 500

kg/m^2s is an incorrect interpretation of the suction curves (cf. sect. 4.1.5.1). The discrepancies between the experimental and predicted values of x_{BO} at $G = 500\ kg/m^2s$ can be explained, in any case partly, by the too insensitive determination of burnout, which was discussed in sect. 3.3.3.

Figure 4.18 shows another comparison between calculated and experimental film flow rates. The measurements were carried out by Bennet et al. (1969) in a tube with steam-water at 69 bar. The inner diameter was 12.7 mm and the heated length 3.66 m. In these experiments the inlet subcooling was kept (approximately) constant at 30^oC, while the heat flux was varied between 75 and 148 W/cm^2.

Also this figure demonstrates that the model reasonably predicts film flow rates in tubes under diabatic conditions.

4.2.4.2. Predictions of Frictional Pressure Gradients. The capability of the model to calculate frictional pressure gradients is demonstrated in figs. 4.19 and 4.20. In fig. 4.19 comparisons are made with the present measurements in test section 10, and in fig. 4.20 the predicted values are shown together with the experimental pressure gradients reported by Kirillov et al. (1973). It is seen that the characteristic drop in $(dp/dz)_f$, which is measured when burnout is approached, is also predicted by the model.

The observed general underprediction of $(dp/dz)_f$ indicates that the heat flux causes an increased roughness of the film surface. However, it is difficult to estimate whether or not this tendency is significant, because of the uncertainty in the determination of the frictional pressure gradient under diabatic conditions, which was discussed in sect. 3.3.2.

4.2.4.3. Predictions of Burnout. The calculation of the burnout steam quality and the corresponding burnout heat flux and power is carried out by an iterative procedure. The integration of eq. (4.39), from the initial point ($\alpha = 0.8$) to the position where the film flow rate vanishes, is first performed with the experimental value of q''_{BO} (i.e. $q''_{BO,exp} = q''^{(1)}$). The calculated value of $x_{BO} = x_{BO}^{(1)}$ gives the axial position of burnout (cf. eq. (3.2)):

$$L_{BO}^{(n)} = (x_{BO}^{(n)}\, r_{ev} + (h_2 - h_1))\frac{Gr_2}{2q''^{(n)}} \qquad (4.44)$$

where n = 1 in the first step.

If $L_{BO}^{(n)}$ differs more than 1% from L_d, a new calculation of $x_{BO} = x_{BO}^{(n+1)}$ is performed with the heat flux $q''^{(n+1)}$:

$$q''^{(n+1)} = (x_{BO}^{(n)} r_{ev} + (h_2 - h_1)) \frac{Gr_2}{2L_d} . \quad (4.45)$$

A new value $L_{BO}^{(n+1)}$ is then estimated from eq. (4.44), and the calculation is continued until

$$|L_d - L_{BO}^{(n)}|/L_d < 0.01. \quad (4.46)$$

Usually, only 2 or 3 iterations are necessary before the criterion (4.46) is fulfilled. The main reason for this fast convergence is that the calculation of x_{BO} is rather insensitive to the value of the heat flux (cf. figs. 4.17.c-e).

The results of the predictions of the burnout measurements presented in sect. 3.3.3 are shown in figs. 4.21-4.23.

Figure 4.21 shows the measured and calculated values of x_{BO} in test section 10 for L_d = 4.02 m and $\Delta T_{sub} = 10^{\circ}C$. It is seen that the characteristic maximum in x_{BO} is reproduced by the model, but the predicted extremum at high mass fluxes occurs at too high pressures. This discrepancy is associated with the observed overprediction of x_{BO} at high mass fluxes and pressures. The overestimation is a consequence of the initial condition eq. (4.43). It is evident that this condition limits the calculation of burnout to steam qualities beyond x_{init}:

$$x_{init} = x(\alpha_{init} = 0.8). \quad (4.47)$$

Because $m_{f,eq}$ is always greater than zero (when x is less than 1), it is evitable that the model overpredicts x_{BO}, when the difference between $x_{BO,exp}$ and x_{init} is small. This is the case for the points at high pressures and mass fluxes in fig. 4.21.

In fig. 4.22 the experimental burnout powers obtained in test section 10 for L_d = 4.02 m and $\Delta T_{sub} = 100^{\circ}C$ are compared to the calculated values. As in fig. 4.21, a good agreement is observed except at high pressures and mass fluxes. The pre-

diction of Q_{BO} for p = 90 bar and G =3000 kg/m^{2}s was not carried out because $x_{BO,exp}$ was less than x_{init}.

The influence of the heated length on the experimental burnout heat flux is shown in fig. 4.23 together with the predictions. These experiments in test section 10 were performed at 70 bar with a 10^{o}C subcooling. In general there was good agreement except at high heat fluxes. As mentioned in sect. 4.2.2, it is believed that the bursting of bubbles from the film, which occurs at high heat fluxes, causes an increment in the entrainment rate. This enhancement, which is not incorporated in the model, is supposed to be responsible for the overestimation of burnout at $q"_{BO} \approx 200$ W/cm^2.

The predictions of burnout in other test sections are summarized in table 4.3. It should be noted that only experiments were $q"_{BO,exp}$ was less than 200 W/cm^2 are included. It is seen that the best results are achieved at low heat fluxes where the diabatic length is long. The greatest discrepancies occur at tube diameters where no diabatic film flow data are available. Finally, it should be mentioned that the scattering due to differences in measuring equipment, experimental procedures, geometrical tolerances, etc., is assumed to be about 5% (cf. Nilsson and Larsson (1971)).

4.3. Equilibrium Conditions in Annular Geometries

The description of fully developed annular flow in annuli is somewhat more complicated than the corresponding description for tubular geometry treated in sect. 4.1. The additional complication arises principally because of the following two reasons:

1) The radius of zero shear stress is not known a priori.
2) It is found experimentally that the tube film carries considerably more liquid per unit perimeter than the rod film.

4.3.1. Shear Stress

The annulus is divided into two subchannels, where the surface of zero stress makes the boundary. The radial position of this surface is denoted r_s. For all symbols used, subscript 1 refers to the subchannel inside r_s, and 2 to the subchannel outside r_s.

Table 4.3

Predictions of Burnout in Tubes

d_2 m	L_d m	p bar	n -	$\bar{e}$ %	$(\sigma^2)^{\frac{1}{2}}$ %	Reference
0.0059	2.7-5.2	69	52	-9.8	11.6	Dell et al. (1969)
0.0100	2.0-8.0	30-90	70	-0.5	6.5	Present results
0.0100	2.0	30-90	43	8.0	12.2	Nilsson (1970)
0.0100	2.0	30-90	41	12.6	14.4	Becker et al.(1965)
0.0100	2.5	70-90	29	8.4	9.8	Becker et al.(1965)
0.0100	3.0	40-90	34	6.8	7.8	Becker et al.(1965)
0.0100	3.5	40-90	28	6.7	7.9	Becker et al.(1965)
0.0100	5.0	50-70	30	-2.3	7.7	Persson (1971)
0.0175	2.5	30-70	21	13.9	15.8	Becker et al.(1965)
0.0199	2.5	30-70	18	11.7	12.7	Becker et al.(1965)
0.0200	3.75	50-70	26	13.3	14.8	Becker et al.(1965)
0.0247	7.1	50-70	44	0.0	4.6	Becker and Ling (1970)
0.0250	2.5	30-70	13	11.3	11.6	Becker et al. (1965)

n: Number of data points analyzed

$\bar{e}$: Mean error $(Q_{BO,cal} - Q_{BO,exp})/Q_{BO,exp}$

$(\sigma^2)^{\frac{1}{2}}$: Standard deviation of errors.

The hydraulic radii for the two subchannels are given by:

$$r_{hj} = |r_s^2 - r_j^2|/r_j \tag{4.48}$$

where subscript j equals 1 or 2.

The shear stresses on the walls become

$$\tau_{wj} = \left(\frac{dp}{dz}\right)_f \frac{r_{hj}}{2} \ . \tag{4.49}$$

The shear stresses should by normal sign convention be of opposite signs, but for the sake of convenience the positive signs are adopted for both τ_{w1} and τ_{w2}.

The interfacial shear stresses are expressed by:

$$\tau_{ij} = \left(\frac{dp}{dz}\right)_f \frac{r_{hij}}{2} \tag{4.50}$$

where

$$r_{hij} = |r_s^2 - r_{ij}^2|/r_{ij} \tag{4.51}$$

and

$$r_{ij} = |r_j - \delta_j|. \tag{4.52}$$

4.3.2. Velocity Profiles in the Films

It is assumed that Prandtl's two-layer model, which was presented in sect. 4.1.2, is also valid for the films in annuli. Thus the following set of equations is obtained (cf. eqs. (4.4)-(4.17)):

$$u_{lj}^+ = u_{lj}/u_{lj}^* \tag{4.53}$$

$$u_{lj}^* = \sqrt{\tau_{wj}/\rho_l} \tag{4.54}$$

$$y_j^+ = y_j u_{lj}^*/\nu_l \tag{4.55}$$

$$y_j = |r_j - r| \tag{4.56}$$

$$u_{lj}^+ = \begin{cases} y_j^+ & y_j^+ \leq 11.5 \\ 2.5 \ln y_j^+ + 5.5 & y_j^+ > 11.5 \end{cases} \tag{4.57}$$

$$u_{ij} = u_{lj}(y_j = \delta_j) \tag{4.58}$$

$$Re_{fj} = \frac{m_{fj}}{2\pi r_j \mu_l} = \int_0^{\delta_j^+} u_{lj}^+ \, dy_j^+ \tag{4.59}$$

$$\delta_j^+ = \delta_j u_{lj}^*/\nu_l \tag{4.60}$$

$$\delta_j^+ = \begin{cases} \sqrt{2Re_{fj}} & Re_{fj} \leq 66.125 \\ \dfrac{Re_{fj} + 38.592}{2.5 \ln \delta_j^+ + 3} & Re_{fj} > 66.125 \end{cases} \tag{4.61}$$

A comparison between theoretical and experimental values has already been shown in fig. 4.1 for the thickness of the rod film.

Due to the lack of experimental values, it was impossible, as mentioned in sect. 3.3.5, to correlate the wavelength of the roll waves in the annular test section to the tube film thickness. In fig. 4.24 the experimental values of λ_w are shown versus the theoretical values of δ_2 calculated from the measurements of m_{f1}, m_{f2} and $(dp/dz)_f$. A good agreement is shown between the measurements in the two geometries, and the following empirical relationship is suggested:

$$\lambda_w = 320\, \delta_2 . \tag{4.62}$$

4.3.3. Velocity Profile in the Core

In the annular gap it is assumed that the position of maximum gas velocity is identical to r_s. For single-phase flows it has been experimentally shown that this is not necessarily true (cf. e.g. Lawn and Elliott (1971)). However, in this connection, the deviations are supposed to be negligible.

Inside and outside r_s we adopt the turbulent logarithmic profile for rough walls (cf. eq. (4.18)):

$$u_{gj}(r) = u_{ij} + u^*_{gj}\left(2.5 \ln \frac{|r_{ij} - r|}{k_{Sj}} + 8.5\right) \tag{4.63}$$

where

$$u^*_{gj} = \sqrt{\tau_{ij}/\rho_g} . \tag{4.64}$$

The mean velocities of the gas in the two subchannels are derived from:

$$\bar{u}_{gj} = 2\pi \left| \int_{r_{ij}}^{r_s} u_{gj}(r) r \, dr \right| / A_{cj} \tag{4.65}$$

where

$$A_{cj} = \pi |r_s^2 - r_{ij}^2| \ . \tag{4.66}$$

The continuity equation for the gas core then becomes:

$$\bar{u}_g = \frac{Gx}{\rho_g \alpha} = \frac{1}{A_c} \sum_j A_{cj} \bar{u}_{gj} \tag{4.67}$$

where

$$A_c = A_{c1} + A_{c2} = \pi (r_{i2}^2 - r_{i1}^2) \ . \tag{4.68}$$

Under the no-slip assumption, the mean void fraction can be calculated:

$$\alpha = \frac{A_c}{A} \frac{m_g/\rho_g}{\frac{m_g}{\rho_g} + \frac{m_e}{\rho_l}} \tag{4.69}$$

where

$$A = \pi (r_2^2 - r_1^2) . \tag{4.70}$$

The condition that the velocities defined by (4.63) have a common maximum velocity at $r = r_s$, may be expressed as:

$$u_{g1}(r_s) = u_{g2}(r_s) . \tag{4.71}$$

When an identical relationship for k_{S1} and k_{S2} is assumed, the equivalent sand roughness can now be determined from the experimental values of m_{f1}, m_{f2} and $(dp/dz)_f$. The variation of k_S with δ_{th} is shown in fig. 4.25. It is seen that the relationship is independent of the pressure (cf. sect. 4.1.3), but the correlation deviates from eq. (4.25), derived for tubular geometries. Due to the lack of experimental information on the velocity profile, it is impossible to determine whether or not

this difference has a physical background, or whether it is a result of an improper assumption (e.g. eq. (4.21), where κ is supposed to be a constant).

The correlating curve can be expressed as (valid for $\delta_{thj} < 800\mu m$):

$$k_{Sj} = 4.74\ \delta_{thj} + 0.80 \cdot 10^3\ m^{-1}\ \delta_{thj}^2 - 0.99 \cdot 10^6\ m^{-2}\ \delta_{thj}^3 + 5.32 \cdot 10^9\ m^{-3}\ \delta_{thj}^4 \quad (4.72)$$

4.3.4. Asymmetric Film Flow Condition

As in the tubular case, the deposition rate is described as (cf. eq. (4.26)):

$$G_{Dj} = k_{Dj}\ c \quad (4.73)$$

where c is the mean droplet concentration, calculated from eq. (4.27).

Thus, in the equilibrium situation, we have (cf. eq. (4.28)):

$$G_{Ej} = k_{Dj}\ c_{eq}\ . \quad (4.74)$$

As in sect. 4.1, it is assumed that the dimensionless ratio:

$$S_{uj} = \frac{k_{Sj}\tau_{ij}\bar{u}_{gj}\mu_l}{\sigma^2} \quad (4.75)$$

is a representative parameter for the entrainment process. Therefore the product $k_{Dj}\ c_{eq}$ is plotted for the rod and tube film versus S_{uj} in figs. 4.26.a-b. The mass transfer coefficients given in table 4.2 are used for both k_{D1} and k_{D2}.

It is seen that there is reasonable agreement between the relationship derived for tubular geometries (eq. (4.34)), and the result shown in fig. 4.26.b for the tube film in the annular geometry.

The disagreement shown in fig. 4.26.a for the rod film is a consequence of the experimental fact that the tube film carries more liquid per unit perimeter than the rod film (cf. sect. 3.3.1.1). It can be explained by an increased entrainment rate and/or a decreased deposition rate for the rod film.

Even if the curvatures of the rod and tube surfaces are of opposite sign, it is supposed that the effect of this relation-

ship on the entrainment rate is negligible, because the thicknesses of the films are much smaller than the radii of the annulus. Therefore, it is assumed that eq. (4.34) is also valid for the rod film:

$$G_{Ej} = 2.0\ S_{uj}\ kg/m^2s. \tag{4.76}$$

The asymmetric film flow in annuli has therefore to be explained by a decreased deposition rate for the rod film, i.e.,

$$k_{D1} < k_{D2}. \tag{4.77}$$

Usually it is supposed that the deposition process can be described by diffusion of the droplets. Thus the diffusion equation was solved for the tubular case by Hutchinson, Whalley and Hewitt (1973). They assumed that the entrainment process took place at the crests of the roll waves at the radial position:

$$r_e = r_2 - b\delta \tag{4.78}$$

where b was assumed to be a constant equal to 5 (cf. sect. 3.3.4). In the equilibrium situation, the following relationship between the diffusion coefficient for the droplets λ_D (m^2/s) and the mass transfer coefficient k_D was derived:

$$k_D = \frac{2\lambda_D}{r_2\left(1 - \frac{r_e^2}{r_2^2}\right)}\ . \tag{4.79}$$

When $b\delta << r_2$, eq. (4.79) reduces to:

$$k_D = \frac{\lambda_D}{b\delta}\ . \tag{4.80}$$

It can be shown that eq. (4.80) is also valid for an annular geometry when $b_j\delta_j << r_j$. Thus we have:

$$\frac{k_{D1}}{k_{D2}} = \frac{\lambda_{D1}}{\lambda_{D2}}\,\frac{\delta_2}{\delta_1} \tag{4.81}$$

where it is assumed that $b_1 = b_2$.

The diffusion coefficient λ_D is usally, by Reynolds analogy, assumed to be proportional to the turbulent eddy viscosity for the gas (cf. e.g. Soo (1967)). The eddy viscosity ε_g (m^2/s) is calculated by:

$$\varepsilon_g = \begin{cases} 0 & \text{for } y \leq y_{tr} \\ \tau/(\rho_g \frac{du_g}{dy}) & \text{for } y > y_{tr} \end{cases} \tag{4.82}$$

where $y_{tr} = y_{tr}^+ \; u_g^*/\nu_g$

By means of eq. (4.63) we obtain:

$$\bar{\varepsilon}_{gj} = \frac{2\pi}{A_{cj}} \left| \int_{r_{trj}}^{r_s} \varepsilon_g(r) r \, dr \right|$$

$$= \frac{2\kappa u_{gj}^* \, r_{ij}}{(r_s^2 - r_{ij}^2)^2} \left\{ \frac{r_s^4}{4} - \frac{2r_s^3 \, r_{ij}}{3} + \frac{r_{trj}^4}{4} \right. \tag{4.83}$$

$$\left. - \frac{r_{ij} r_{trj}^3}{3} - \frac{r_s^2 r_{trj}^2}{2} + r_s^2 r_{ij} r_{trj} \right\}$$

where $r_{trj} = r_{ij} - (-1)^j y_{tr}$

The ratio between the mass transfer coefficients thus becomes

$$\frac{k_{D1}}{k_{D2}} = \frac{\overline{\varepsilon_{g1}}}{\overline{\varepsilon_{g2}}} \frac{\delta_2}{\delta_1} \tag{4.84}$$

When representative values of r_s, δ_1, δ_2 are inserted in eqs. (4.83)-(4.84), we obtain a ratio greater than unity, which is in contradiction to the inequality (4.77). Therefore it must be concluded that the application of diffusion theory and/or Reynolds analogy is inadequate for the description of the deposition process in annular geometries.

The main reason for this insufficiency is believed to be the large size of the droplets. A characteristic droplet diameter in annular steam-water flow is 100 μm (cf. e.g. Tatterson, Dallman and Hanratty (1977)). This large size makes the droplets rather insensitive to the fluctuations of the gas, so that their mean free path becomes of the same order as the dimensions of the test sections (cf. Hewitt and Hall-Taylor (1970)).

However, the experimental asymmetry can be qualitatively understood by means of the relationship between the turbulent kinetic energy and the local void fraction derived by Lahey (1976). Assuming proportionality between the turbulent kinetic energy of the liquid and the gas phase, he derived the following relationship from the two-fluid momentum equations under isotropic conditions:

$$\frac{\alpha_{loc}^{t}}{1 - \alpha_{loc}} = C_2 \, T_l^{1-t} \tag{4.85}$$

where α_{loc} is the local void fraction and T_l (kg/ms^2) is the turbulent kinetic energy of the liquid per unit volume:

$$T_l = \frac{3}{2} \rho_l \overline{u'_l{}^2} \tag{4.86}$$

where $\overline{u'_l{}^2}$ is the mean value (in time) of the square of the fluctuating component of the liquid velocity.

The ratio between the turbulent kinetic energies is denoted t:

$$t = \frac{T_g}{T_l} = \frac{\frac{3}{2}\rho_g \overline{u'_g{}^2}}{\frac{3}{2}\rho_l \overline{u'_l{}^2}} = C_1 \frac{\rho_g}{\rho_l} . \tag{4.87}$$

C_1 and C_2 (in eq. (4.85)) are assumed to be constants.

For large droplet sizes, it is assumed that the influence of the turbulent gas is so weak that

$$\overline{u'_l{}^2} < \frac{\rho_l}{\rho_g} \overline{u'_g{}^2} \tag{4.88}$$

in the gas core. When (4.88) is fulfilled it appears from eq.

(4.87) that t is greater than unity. In this case it appears from eq. (4.85) that the local void fraction is greatest where the kinetic turbulent energy is smallest. From single-phase measurements in tubes and annuli, it appears that the turbulent kinetic energy decreases with the wall distance (cf. Laufer (1953), Lawn and Elliott (1971)). Thus eq. (4.85) can explain the existence of a gas core in annular flow under the assumption of inequality (4.88).

If $t < 1$, eq. (4.85) predicts that the local void fraction is largest at the walls. This is in fact the case in the bubbly flow regime, where the turbulence of the liquid phase is dominating (cf. Serizawa, Kataoka and Michiyoshi (1975)).

We will now return to the case where $t > 1$ and, by means of eq. (4.85), explain the asymmetric film flow in annuli by the existence of an asymmetric turbulence profile. From single-phase measurements in channels with a rough and a smooth wall, it appears that the turbulence level is higher in the region near the rough wall (cf. Hanjalic and Launder (1972)). This indicates that if an asymmetric film flow is first established, the asymmetry will be maintained due to the progressive relationship between the film thickness and roughness (eq. (4.72)). Measurements in smooth annuli imply that the turbulence level outside r_s is greater than the turbulence level inside r_s already in the single-phase (cf. Brighton and Jones (1964)). Thus it is probable that the tube film is thicker than the rod film in the fully developed, equilibrium situation.

The explanation suggested above is supported by the film flow measurements, which were performed at very low steam qualities (cf. fig. 3.19.b). Here it was shown that the ratio between the film flow rates per unit perimeter tends to unity, and the fraction of entrained liquid increases when the steam quality tends to zero, i.e. when t becomes less than unity.

From the experimental film flow rates it was evaluated that the introduction of

$$k_{D1} = 0.4\ k_{D2} \tag{4.89}$$

described the asymmetry in an adequate manner.

This condition closes our set of equations for calculation of the equilirbium conditions for annular flow in annuli.

4.3.5. Predictions of Data

As in the tubular case (sect. 4.1.5), we will now illustrate the capability of our model by comparisons between calculated and experimental film flow rates and frictional pressure gradients.

4.3.5.1. Predictions of Film Flow Rates. In figs. 4.27.a-b the predicted values of rod and tube film flow rates are compared to the adiabatic measurements in test section 17/26L at 70 bar. Similar comparisons are shown in fig. 4.28 for 30, 50 and 90 bar. It is seen that the agreement is in general good, but that the model overestimates the experimental tube film flow rates at low gas velocities. This was also the case in the tubular geometry (cf. sect. 4.1.5.1), and the main reason is also here supposed to be an incorrect interpretation of the suction curves.

The effect of geometry is illustrated in fig. 4.29, where data for developing, adiabatic film flow are compared to the calculations. The measurements were carried out by Moeck (1970) in an annulus (d_1 = 0.0197 m, d_2 = 0.0238 m) with a movable heater inside the rod, so the adiabatic length could be varied. The prediction was performed by means of eq. (4.92) with $q_1" = q_2" = 0$. The calculation was initiated with the experimental film flow rates at $L_a = 0$. The figure indicates that a higher ratio between the mass transfer coefficients than that given by eq. (4.89) would improve the agreement. An increment of the ratio seems reasonable for Moeck's narrower geometry because - for symmetrical reasons - k_{D1}/k_{D2} must tend to unity when d_1/d_2 does. However, due to the few equilibrium measurements (8) carried out by Moeck, it was impossible to establish a convincing relationship between the diameter ratio and k_{D1}/k_{D2}.

4.3.5.2. Predictions of Frictional Pressure Gradients. In fig. 4.30 the calculated values of $(dp/dz)_f$ are compared to the measurements in test section 17/26L. It is not surprising that the agreement is excellent, since the roughness correlation (eq. (4.72)) has been in fact deduced from these data. When a similar comparison was carried out for the equilibrium data by Moeck (1970), a general overprediction of about 10% appeared. However, this discrepancy is believed to result mainly from the

too low ratio between the mass transfer coefficients discussed above.

4.4. Diabatic Conditions in Annular Geometries

This final section of the analytical part of this report, treats the diabatic film flows in annuli.

The relationships derived in sect. 4.2 for diabatic films in tubes are assumed also to be valid for annuli.

4.4.1. Mass Balances on the Films

The differential changes in the flow rates of gas, entrained liquid, and films thus become (cf. eqs. (4.35)-(4.39)):

$$\frac{dm_g}{dz} = \frac{\pi(d_1 q_1'' + d_2 q_2'')}{r_{ev}} \tag{4.90}$$

$$\frac{dm_e}{dz} = \pi(d_1(G_{E1} - G_{D1}) + d_2(G_{E2} - G_{D2})) \tag{4.91}$$

$$\frac{dm_{fj}}{dz} = \pi d_j (G_{Dj} - G_{Ej} - \frac{q_j''}{r_{ev}}). \tag{4.92}$$

4.4.2. Entrainment and Deposition Rates

The entrainment rates are calculated from eq. (4.76), and the expression for the deposition rates becomes (cf. eqs. (4.40)-(4.42)):

$$G_{Dj} = (k_{Dj} - e^{-\delta_j/50\mu m} \frac{q_j''}{r_{ev}\ \rho_g}) c. \tag{4.93}$$

4.4.3. Initial Conditions

As in the tubular case, the initial condition was chosen as:

$$m_{fj}(\alpha = 0.8) = m_{fj,eq}(\alpha = 0.8) \tag{4.94}$$

where $m_{fj,eq}$ is calculated from sect. 4.3.

4.4.4. Predictions of Data

Finally, calculations of film flow rates, frictional pressure gradients, and burnout steam qualities will be compared to measurements in annuli under diabatic conditions.

4.4.4.1. Predictions of Film Flow Rates. In figs. 4.31.a-b examples are shown of predictions of the film flow measurements in test section 17/26S. It is seen that the agreement in general is good. Due to the existence of two walls, which can be heated individually, it is seen from fig. 4.31.b that the films are not so independent of the heat flux at the initial point as in the tubular case (cf. also figs. 3.20.a-b). Thus it appears from fig. 4.31.a that the best agreement is achieved when the two heat fluxes are equal.

4.4.4.2. Predictions of Frictional Pressure Gradients. The measurements of $(dp/dz)_f$ shown in fig. 3.26 are compared to the calculated values in fig. 4.32. From the results at G = 900 kg/m^2s it is seen that the model takes proper account of the measured variation of $(dp/dz)_f$ with the heat flux distribution.

4.4.4.3. Predictions of Burnout. The calculation of burnout is carried out as in the tubular case (cf. sect. 4.2.4.3), with a fixed ratio between the heat fluxes. The steam quality is set equal to x_{BO} when m_{f1} and/or m_{f2} vanishes. The axial position of burnout is then calculated (cf. eq. (4.44)):

$$L_{BO}^{(n)} = (x_{BO}^{(n)} \, r_{ev} + (h_2 - h_1)) \, \frac{G(r_2^2 - r_1^2)}{q_1''^{(n)} r_1 + q_2''^{(n)} r_2} \qquad (4.95)$$

and so on.

In figs. 4.33.a-b the burnout measurements performed by Jensen and Mannov (1974) in test section 17/26S are shown together with the predictions. It is seen that burnout takes place on the rod as long as the fraction of power on the tube is less than approximately 0.70. This relationship is, of course, a consequence of the asymmetric film flow conditions discussed in sect. 4.3.4. The figure shows a reasonably good agreement, even if the asymmetry seems to be overestimated.

The effect of geometry and pressure is illustrated in figs. 4.34.a-b. Similarly, examples of the burnout measurements of Becker and Letzter (1975) are shown together with the predic-

tions. The measurements were carried out in an annulus with a slightly smaller diameter ratio than test section 17/26S. Also these comparisons for 30 and 70 bar show a good agreement between experiments and theory.

A summary of the predictions is given in table 4.4.

Table 4.4

Predictions of Burnout in Annuli

d_1 m	d_2 m	L_d m	p bar	QF -	n -	$\bar{e}$ %	$(\sigma^2)^{\frac{1}{2}}$ %	Ref
0.0120	0.0213	3.0	30-70	0-1	38	1.4	7.6	a
0.0137	0.0222	2.6-2.8	42-69	0	26	4.2	10.3	b
0.0159	0.0210	3.7-4.6	52-69	0	49	-3.6	7.8	c
0.0170	0.0260	3.5	70	0-1	48	-5.6	10.9	d

QF: Power fraction $Q_{BO2}/(Q_{BO1} + Q_{BO2})$

n: Number of data points analyzed

$\bar{e}$: Mean error $(Q_{BO,cal} - Q_{BO,exp})/Q_{BO,exp}$

$(\sigma^2)^{\frac{1}{2}}$: Standard deviation of errors

References: a) Becker and Letzter (1975)
b) Janssen and Kervinen (1963)
c) Little (1970)
d) Jensen and Mannov (1974)

5. SUMMARY AND CONCLUSIONS

An experimental and theoretical investigation of the annular steam-water flow regime in tubes and annuli was performed.

More than 200 film flow measurements are presented in the report together with experimental data on pressure gradients, film thicknesses, wave frequencies and velocities, and burnout heat fluxes.

The adiabatic experiments were carried out under conditions that allow the data to be regarded as equilibrium data. The equilibrium measurements in annuli showed an asymmetric film flow condition, where the tube film carried considerably more liquid per unit perimeter than the rod film. It was shown that

the diabatic film flow is independent of the subcooling, as long as there is no steam at the inlet. It was demonstrated that burnout takes place at the axial position where the film flow rate vanishes. The wave measurements gave an indication of proportionality between the wavelength of the roll waves and the film thickness.

On the basis of the experimental data, a film-flow model for annular flow in tubes and annuli was set up. It was shown that the velocity profile in the film could be described adequately well by Prandtl's turbulent two-layer model. The velocity distribution in the gas core was described by the turbulent, logarithmic profile for completely rough walls. A general film roughness correlation between the equivalent sand roughness and the film thickness was derived. By the introduction of a new entrainment parameter, a general entrainment correlation was shown to be valid for both air-water at low pressures and steam-water at 30-90 bar. The asymmetric film flow in annuli was discussed, and the inability of diffusion theory to describe the deposition process was demonstrated. The main reason for this insuffiency was assumed to be the large droplet size, and assuming that the gas turbulence has only little influence on the droplets, the asymmetry was qualitatively explained by means of a relationship between the local void fraction and the turbulent kinetic energy.

The capability of the model was demonstrated by several comparisons between measurements and predictions of film flow rates, frictional pressure gradients, and burnout heat fluxes.

In general, good agreement was obtained especially under adiabatic conditions and at moderate heat fluxes, where the effect of enhanced entrainment due to bursting of bubbles from the film surface can be neglected.

Although the film-flow model has thus proved to describe annular steam-water flow in tubes and annuli reasonably well, it should be recognized that further investigation of several aspects are desirable.

It was indicated that the model overpredicts burnout at high heat fluxes; therefore it would be expedient to perform diabatic experiments at heat fluxes beyond 200 W/cm^2, so that the effect

of increased entrainment due to the bursting of bubbles could be implemented in the model.

An extension of the set of annular test sections would also be valuable to establish a convincing relationship between the diameter ratio and the mass transfer coefficients.

The asymmetric film flow condition in annuli demonstrates that a more fundamental physical knowledge of the deposition process is highly desirable. Therefore measurements of local properties (e.g. local velocities, turbulence levels, void fractions, and droplet sizes) would be a great advantage in a further development of the model.

ACKNOWLEDGEMENTS

I am deeply indebted to my supervisor Peter S, Andersen for fruitful discussions, kind guidance and encouragement, and also to the entire staff of SEHT for their invaluable help in the experimental work.

NOMENCLATURE

Main Symbols

A	m^2	Cross-sectional area
b	-	Ratio between mean film thickness and wave amplitude (cf. eq. (4.78))
B	-	Roughness function in the velocity profile
c	kg/m^3	Mean droplet concentration
$C(\kappa, B, y^+_{tr})$	-	Constant in eq. (4.15)
$C_v(t)$	V^2	Cross-correlation of needle signals (cf. fig. 3.36)
C_1	-	Constant in eq. (4.87)
C_2	ms^2/kg	Constant in eq. (4.85)
$(dp/dz)_{acc}$	Pa/m	Acceleration pressure gradient
$(dp/dz)_f$	Pa/m	Frictional pressure gradient
$(dp/dz)_{f,l}$	Pa/m	Single-phase frictional pressure gradient
$(dp/dz)_{hyd}$	Pa/m	Hydrostatic pressure gradient
$(dp/dz)_{tot}$	Pa/m	Total pressure gradient
d_1	m	Outer diameter of the rod in annular test sections
d_2	m	Inner tube diameter
$\bar{e}$	-	Mean error
f_w	s^{-1}	Wave frequency (cf. fig. 3.35)
F_E	kg/m^3	Constant in eq. (4.31)
G	kg/m^2s	Total mass flux
G_D	kg/m^2s	Deposition rate
G_E	kg/m^2s	Entrainment rate
h_i	J/kg	Enthalpy of water at temperature T_i
HB	-	Dimensionless heat balance
k_{BJ}	-	Constant in eq. (3.25)
k_D	m/s	Mass transfer coefficient
k_s	-	Constant in eq. (3.24)
k_S	m	Equivalent sand roughness
k_w	m^{-1}	Wavenumber for roll waves
l	m	Length of test section
L_a	m	Adiabatic length
L_d	m	Diabatic length
L_m	m	Needle distance (cf. eq. (3.34))
L_{BO}	m	Axial position of burnout

m	kg/s	Mass flow rate
p	Pa	System pressure
q''	W/m^2	Heat flux
Q_{th}	W	Thermal power
Q_0	W	Electrical power on the steam generator
Q_1	W	Electrical power on the rod
Q_2	W	Electrical power on the tube
r	m	Radial coordinate
r_e	m	Radial position of wave crest
r_{ev}	J/kg	Evaporation heat at saturation temperature
r_s	m	Radius of zero shear stress
r_1	m	Outer radius of the rod
r_2	m	Inner radius of the tube
R	-	Constant in eq. (3.26)
Re_f	-	Film Reynolds number
s_c	-	Slope of the suction curve (cf. fig. 3.9)
s_w	-	Slope of the suction curve (cf. fig. 3.9)
S	-	Mean slip ratio
S_k	-	Entrainment parameter (cf. eq. (4.32))
S_u	-	Entrainment parameter (cf. eq. (4.33))
$S_v(f)$	V^2s	Power spectrum of needle signal (cf. fig. 3.35)
S_δ	-	Entrainment parameter (cf. eq. (4.29))
t	-	Ratio between T_g and T_l
T	kg/ms^2	Turbulent kinetic energy per unit volume
T_{sat}	^oC	Saturation temperature
T_w	s	Time for a wave to pass between two probes (cf. fig. 3.26)
T_0	^oC	Temperature at the inlet of the steam generator
T_1	^oC	Temperature at the inlet of the test section
T_2	^oC	Temperature at the outlet of the test section
T_3-T_{10}	^oC	Temperatures in the heat balance unit (cf. fig. 3.2)
u	m/s	Axial velocity
$\bar{u}$	m/s	Mean value (in space) of u
u'	m/s	Fluctuating component of u
$\overline{u'^2}$	m^2/s^2	Mean value (in time) of the square of u'
u^+	-	Dimensionless velocity $u^+ = u/u^*$

u^*	m/s	Friction velocity $u^* = \sqrt{\tau/\rho}$
v	m/s	Radial velocity
v_w	m/s	Wave velocity
V_t	V	Trigger level (cf. fig. 3.8)
x	-	Steam quality
$x_{c,s}$	-	Steam quality in the core near the wall (cf. eq. (3.9))
y	m	Distance from wall
y_D	m	Constant in eq. (4.41)
y^+	-	Dimensionless wall distance $y^+ = yu^*/\nu$
z	m	Axial coordinate
z_i	m	Axial position of pressure tap i
z_{mi}	m	Midpoint between z_i and z_{i+1}
Z_E	-	Constant in eq. (4.31)
α	-	Mean void fraction
$\alpha_{c,m}$	-	Mean void fraction in the core (cf. eq. (3.12))
$\alpha_{c,s}$	-	Void fraction in the core near the wall
α_w	-	Void fraction in the wave region
δ	m	Film thickness
δ^+	-	Dimensionless film thickness $\delta^+ = \delta u^*_l/\nu_l$
Δf_w	s^{-1}	Frequency range (cf. fig. 3.25)
Δh_{sub}	J/kg	Enthalpy difference $h_{sub} = h_2 - h_1$
Δp_i	Pa	Pressure drop between z_i and z_{i+1}
ΔT_{sub}	^oC	Inlet subcooling $\Delta T_{sub} = T_2 - T_1$
$\Delta\alpha$	-	Void fraction difference $\Delta\alpha = \alpha_{c,m} - \alpha_{c,s}$
ε	m^2/s	Eddy viscosity
$\bar{\varepsilon}$	m^2/s	Mean value (in space) of ε
κ	-	von Kármáns constant
λ_w	m	Wavelength of the roll waves
λ_D	m^2/s	Droplet diffusion coefficient
μ	kg/ms	Dynamic viscosity
ν	m^2/s	Kinematic viscosity
ρ	kg/m^3	Density
ρ'	-	Density ratio $\rho' = \rho_l/\rho_g$
σ	N/m	Surface tension of water
$(\sigma^2)^{\frac{1}{2}}$	-	Standard deviation

τ	N/m^2	Shear stress
τ_{con}	-	Dimensionless needle contact time
τ_{min}	-	Minimum value of τ_{con}
ϕ^2	-	Two-phase multiplier (cf. eq. (3.31)).

Subscripts*

BO	Burnout
c	Core
cal	Calculated
cont	Containment
cr	Critical
curv	Curvature
e	Entrained liquid
eq	Equilibrium
ev	Evaporation
exp	Experimental
f	Film
g	Gas phase
h	Hydraulic
h.ex.	Heat exchanger
i	Interfacial
init	Initial
j	j = 1: Inside r_s j = 2: Outside r_s
l	Liquid phase
loc	Local
max	Maximal
min	Minimal
nom	Nominal
out	Outlet
p	Primary
s	Secondary
th	Theoretical
tr	Transition
w	Wall

*unless otherwise specified among the main symbols.

REFERENCES

Andersen, P.S. (1972). Developing film flow: An analysis of adiabatic data and a new model for diabatic films. Research Establishment Risø, Section of Experimental Technology. SDS-50, 13 pp. (internal report).

Andersen, P.S. and Würtz, J. (1975). A film-flow model for annular flow in an annulus. Paper presented at European Two-Phase Flow Group Meeting, Haifa, June 2-5, 1975. 22 pp.

Andersen, P.S., Jensen, A., Mannov, G., and Olsen, A. (1974). Burn-out, circumferential film flow distribution and pressure drop for an eccentric annulus with heated rod. Int. J. Multiphase Flow. 1, 585-600.

Becker, K.M. and Letzter, A. (1975). Burnout Measurements for flow of water in an annulus with two-sided heating. Paper presented at European Two-Phase Flow Group Meeting, Haifa, June 2-5, 1975. Royal Institute of Technology, Nuclear Engineering Lab. (Stockholm). KTH-NEL-23, 28 pp. (internal report).

Becker, K.M. and Ling, C.H. (1970). Burnout measurements in a round tube of 7100 mm heated length. Royal Institute of Technology, Nuclear Engineering Lab. (Stockholm). KTH-NEL-13 (internal report).

Becker, K.M., Hernborg, G., Bode, M., and Eriksson, O. (1965). Burnout data for flow of boiling water in vertical ducts, annuli and rod clusters. Aktiebolaget Atomenergi, (Stockholm). AE-177, 108 pp.

Bennet, A.W., Hewitt, G.F., Kearsey, H.A., Keeys, R.K.F., and Pulling, D.J. (1967). Studies of burnout in boiling heat transfer. Trans. Inst. Chem. Eng. 45, no. 8, T319-T333.

Bennet, A.W., Hewitt, G.F., Kearsey, H.A., and Keeys, R.K.F. (1968). Heat transfer to steam-water mixtures flowing in uniformly heated tubes in which the critical heat flux has been exceeded. Paper presented at: Thermodynamics and Fluid Mechanics Convention, Bristol, March 27-29, 1968, Institution of Mechanical Engineers, Paper no. 27. Also as: Atomic Energy Research Establishment, (Harwell). AERE-R-5373, 23 pp.

Bennet, A.W., Hewitt, G.F., Kearsey, H.A., Keeys, R.K.F., and Stinchcombe, R.A. (1969). Measurement of liquid film flow rates at 1.000 psia in upward steam water flow in a vertical heated tube. Atomic Energy Research Establishment (Harwell). AERE-R-5809, 10 pp.

Bennett, J.A.R. and Thornton, I.D. (1961). Data on the vertical flow of air-water mixtures in the annular and dispersed flow regions. Part I: Preliminary Study. Trans. Inst. Chem. Engrs. 39, 101-112.

Brighton, J.A. and Jones, J.B. (1964). Fully developed flow in annuli. J. Basic Eng. 86, 835-844.

Butterworth, D. (1968). Air-water climbing film flow in an eccentric annulus. Atomic Energy Research Establishment (Harwell). AERE-R-5787, 24 pp.

Collier, J.G. (1977). Steady state two-phase flow and heat transfer. Paper presented at the Ispra Courses, Thermohydraulic problems related to reactor safety. Part B: LWR related thermohydraulic problems. September 29-30th, 1977. Commision of the european communities. Joint Research Centre. Ispra, 77 pp.

Collier, J.G. and Hewitt, G.F. (1961). Data on the vertical flow of air-water mixtures in the annular and dispersed flow regions. Part II: Film thickness and entrainment data and analysis of pressure drop measurements. Trans. Inst. Chem. Engrs. 39, 127-136. Also as: Atomic Energy Research Establishment (Harwell). AERE-R-3455, 41 pp.

Cousins, L.B. and Hewitt, G.F. (1968). Liquid phase mass transfer in annular two-phase flow: droplet deposition and liquid entrainment. Atomic Energy Research Establishment (Harwell). AERE-R-5657, 36 pp.

Cortzen, F.W. (1976). Thyristor power supply filtering for a 0.5 MW heat transfer-loop. Risø National Lab. RISØ-M-1892, 16 pp.

Dell, F.R., Hewitt, G.F., Keeys, R.K.F., and Stinchcombe, R.A. (1969). Burnout heat flux measurements in a long tube. Atomic Energy Research Establishment (Harwell). AERE-M-2216.

Friedel, L. (1977). Mean void fraction and friction pressure drop: Comparison of same correlations with experimental data. Paper presented at European Two-Phase Flow Group Meeting, Grenoble, June 6-8, 1977. 24 pp.

Gill, L.E., Hewitt, G.F., and Lacey, P.M.C. (1965). Data on the upwards annular flow of air-water mixtures. Chem. Eng. Sci. 20, 71-88.

Gill, L.E., Hewitt, G.F., and Lacey, P.M.C. (1968). Sampling probe studies of the gas core in annular two-phase flow. Part 2. Studies of the effect of phase flow rates on phase and velocity distribution. Atomic Energy Research Establishment (Harwell). AERE-R-3955, 26 pp.
Also published in: Chem. Eng. (1964) 19, 665-682.

Hanjalic, K. and Launder, B.E. (1972). Fully developed asymmetric flow in a plane channel. J. Fluid Mech. 51, 301-335.

Hewitt, G.F. (1978). Critical heat flux in flow boiling. Paper presented at 6th International Heat Transfer Conference, Toronto, August 7-11, 1978. 28 pp.

Hewitt, G.F. and Hall-Taylor, N.S. (1970). Annular two-phase flow (Pergamon, Oxford) 310 pp.

Hewitt, G.F. and Pulling, D.J. (1969). Liquid entrainment in adiabatic steam-water flow. Atomic Energy Research Establishment (Harwell). AERE-R-5374, 9 pp.

Hewitt, G.F., Kearsey, H.A., Lacey, P.M.C. and Pulling, D.J. (1965). Burnout and film flow in the evaporation of water in tubes. Proc. Inst. Mech. Engrs. 180, Part 3C, 206-215.

Hutchinson, P. and Whalley, P.B. (1973). A possible characterisation of entrainment in annular flow. Chem. Eng. Sci. 28, 974-975.

Hutchinson, P., Whalley, P.B. and Hewitt, G.F. (1973). Transient flow redistribution in annular two-phase flow. Atomic Energy Research Establishment (Harwell). AERE-R-7522, 16 pp.

Isbin, H.S., Vanderwater, R, Fauske, H., and Singh, S. (1961). A model for correlating two-phase, steam-water, burnout heat transfer fluxes. J. Heat Transfer 83, 149-157.

Janssen, E. and Kervinen, J.A. (1963). Burnout conditions for single rod in annular geometry, water at 600 to 100 psia. General Electric Company (San Jose, Calif.). GEAP-3899, 154 pp.

Jensen, A. (1974). Description of loop and test sections for SDS-Annulus-experiments. Research Establishment Risø, Section of Experimental Heat Transfer. SDS-64, 8 pp. (internal report).

Jensen, A. and Mannov, G. (1974). Measurements of burnout, film flow, film thickness and pressure drop in a concentric annulus 3500 x 26 x 17 mm with heated rod and tube. Research Establishment Risø, Section of Experimental Heat Transfer. SDS-77, 11 pp. (internal report).

Jensen, A., Olsen, A., Mannov, G., Seir Olsen, J., and Hartig, A. (1971). Film flow experiments in an annulus geometry. Research Establishment Risø, Section of Experimental Heat Transfer. SDS-17, 9 pp. (internal report).

Keeys, R.K.F., Ralph, J.C., and Roberts, D.N. (1970a). Liquid entrainment in adiabatic steam-water flow at 500 and 1000 psia. Atomic Energy Research Establishment (Harwell) AERE-R-6293, 10 pp.

Keeys, R.K.F., Ralph, J.C., and Roberts, D.N. (1970b). The effect of heat flux on liquid entrainment in steam-water in a vertical tube at 1000 psia ($6.894 \times 10^6 N/m^2$). Atomic Energy Research Establishment (Harwell). AERE-6294, 10 pp.

Kirillov, P.L., Komarov, H.M., Subbotin, V.I., Smogalev, I.P., Suvorov, M.Ya., Shchteiĭ, Yu. Yu., Shchumskii, R.V., and Shchikovskii, Yu. D. (1973). Izmerenie nekotorykh kharakteristik parozhidkostnogo potoka v krugloj trube pri devlenii 68.6 bar. Fiziko-Ehnergeticheskij Inst. FEI 421, 104 pp.

Lahey, R.T. (1976). Two phase flow phenomena in nuclear reactor technology. Rensselaer Polytechnic Institute, Department of Nuclear Engineering (Troy, New York) RPI Research Project No. JBE43. Quarterly Progress Report No. 1, 28 pp.

Laufer, J. (1953). The structure of turbulence in fully developed pipe flow. National Advisory Committee for Aeronautics. NACA-TN-2954, 53 pp.

Lawn, C.J. and Elliott, C.J. (1971). Fully developed turbulent flow through concentric annuli. Great Britain Central Electricity Generating Board, Berkeley Nuclear Lab. RD-B-N-1878, 60 pp.

Little, R.B. (1970). Dryout tests on an internally heated annulus with variation of axial heat flux distribution. Atomic Energy Establishment (Winfrith, U.K.) AEEW-R-578, 76 pp.

Mannov, G. (1973a). Instrumentation and evaluation for film flow measurements by a heat balance unit. Research Establishment Risø, Section of Experimental Heat Transfer. SDS-63, 15 pp. (internal report).

Mannov, G. (1973b). Film flow measurements in concentric annulus 3500 x 27.2 x 17 mm with heated and unheated rod. Research Establishment Risø, Section of Experimental Technology. SDS-65, 7 pp. (internal report).

Moeck, E.O. (1970). Annular-dispersed two-phase flow and critical heat flux. Atomic Energy of Canada Ltd. AECL-3656, 337 pp.

Nigmatulin, B.I., Malyshenko, V.I., and Shugaev, Yu. Z. (1976). Investigation of liquid distribution between the core and the film in annular dispersed flow of steam/water mixture. Them. Eng. 23, no. 5, 66-68.

Nilsson, L. and Larsson, A. (1970). Burnoutdatabank. Innehåll och upläggning. Aktiebolaget Atomenergi (Stockholm). AE-RL-1274, 33 pp. (internal report).

Nilsson, L. (1970). Repeatability test of critical heat flux data for 1970 Meeting at the European Two-phase Flow Group. Comparison of results by Becker's burnout correlation. Aktiebolaget Atomenergi (Stockholm) AE-RL-1229 (internal report).

Paleev, I.I. and Filippovich, B.S. (1966). Phenomena of liquid transfer in two-phase dispersed annular flow. Int. J. Heat Mass Transfer 9, 1089-1093.

Persson, N.O. Investigation of burnout in a vertical round duct with a great length (Private communication).

Schlichting, H. (1968). Boundary-layer Theory. 6.ed. (McGraw-Hill, New York) 747 pp.

Schmidt, E. (editor) (1969). Properties of water and steam in SI-units (Springer, München) 205 pp.

Schaub, F.A., Simpson, R.L, and Janssen, E. (1969). Two-phase flow and heat transfer in multirod geometries. Air-water flow structure data for a round tube, concentric and eccentric annulus, and nine-rod bundle. General Electric. GEAP-5739, 214 pp.

Serizawa, A., Kataoka, I., and Michiyoshi, I. (1975). Turbulence structure of air-water bubbly flow - 2. Local Properties. Int. J. Multiphase Flow 2, 235-246.

Singh, K., Pierre, C.C.St., Crago, W.A., and Moeck, E.O. (1969). Liquid film flow rates in two-phase flow of steam and water at 1000 Lb./Sq. in.abs.. AIChE J. 15, 51-56.

Soo, S.L. (1967). Fluid dynamics of multiphase systems (Blaisdell, Waltham, Mass.) 524 pp.

Tatterson, D.F., Dallman, J.C., and Hanratty, T.J. (1977). Drop sizes in annular gas-liquid flow. AIChE J. 23, 68-76.

Wallis, G.B. (1969). One-dimensional two-phase flow (McGraw-Hill, New York) 408 pp.

Webb, D. (1970). Studies of the characteristics of downward annular two phase flow. Atomic Energy Research Establishment (Harwell) AERE-R-6426, 138 pp.

Whalley, P.B., Hewitt, G.F., and Hutchinson, P. (1973). Experimental Wave and entrainment measurements in vertical annular two-phase Flow. Atomic Energy Research Establishment (Harwell) AERE-R7521, 13 pp.

Whalley, P.B., Hutchinson, P., and Hewitt, G.F. (1974). The calculation of critical heat flux in forced convection boiling. Paper presented at 5th International Heat Transfer Conference, Tokyo, September 3-7, 1974, 5 pp.

APPENDIX

Tables

Table A1. Film Flow Measurements. Test Section 17/26S. Diabatic. L_a = 0.1 m. L_d = 3.5 m .

	Main System Parameters					Experimental Data				Entr.	Voids			
Run	p	G	m	q"	x_{out}	m_f/m		s_c	s_w	m_e/m	Core			Wave
						Min.	Max.				$\alpha_{c,s}$	$\alpha_{c,m}$	$\Delta\alpha/\alpha_{c,s}$	α_w
	bar	kg/m²s	kg/s	W/cm²	%	%	%	-	-	%	%	%	%	%
101	70	500	0.152	0	20	10.6	15.7	0.72	3.45	20.7	96.5	95.1	-1.4	85.4
				50		38.0	43.6	0.62	4.30		97.0		-1.9	82.4
102				10	20	9.6	14.9	0.66	3.05	21.4	96.8	94.9	-1.9	86.9
				40		42.2	43.7	0.96	2.90		95.4		-0.5	87.4
103				20	20	10.1	13.7	0.63	4.68	20.6	96.9	95.1	-1.8	81.2
				30		41.5	45.7	0.86	7.15		95.9		-0.7	73.9
104				30	20	9.2	12.8	0.57	2.63	18.8	97.2	95.5	-1.7	88.5
				20		41.5	48.4	0.82	2.75		96.1		-0.5	88.0
105				40	20	8.6	12.2	0.46	2.40	19.8	97.7	95.3	-2.4	89.4
				10		42.8	48.0	1.00	5.40		95.2		0.04	78.9
106				50	20	9.5	11.2	0.70	2.25	21.2	96.6	95.0	-1.6	90.0
				0		43.2	47.6	1.44	4.65		93.3		1.7	81.3
107		600	0.182	40	60	3.6	4.8	0.01	2.13	16.9	99.9	98.6	-1.3	90.4
				40		12.9	18.3	0.08	4.55		99.6		-0.9	81.6
108				60	60	3.5	4.0	0.08	1.53	16.2	99.6	98.6	-0.9	92.9
				60		12.4	19.8	0.12	5.50		99.4		-0.7	78.6
109				66	60	3.8	4.5	0.01	1.05	16.4	99.9	98.6	-1.2	95.0
				66		16.1	19.1	0.16	3.85		99.2		-0.5	84.0
110		900	0.274	0	20	11.7	16.2	0.70	3.95	22.0	96.6	94.8	-1.8	83.6
				85		32.4	41.8	0.34	13.4		98.3		-3.5	60.2
111				0	30	7.8	13.2	0.30	6.05	28.4	98.5	95.5	-3.0	77.0
				85		25.6	28.4	0.68	3.60		96.7		-1.2	84.9
112				0	40	7.6	11.7	0.06	3.15	30.1	99.7	96.4	-3.2	86.5
				85		11.8	18.2	0.08	5.85		99.6		-3.1	77.6
113				0	50	6.2	8.8	0.16	3.35	33.7	99.2	96.7	-2.4	85.8
				85		8.0	7.5	0.10	2.00		99.5		-2.7	91.0
114				85	20	5.4	8.8	0.36	3.65	19.0	98.2	95.5	-2.7	84.7
				0		44.8	52.2	1.32	12.40		93.8		1.7	62.0
115				85	25	5.7	7.5	0.26	1.90	20.6	98.7	96.0	-2.6	91.4
				0		41.0	46.9	1.26	12.4		94.1		2.0	62.0
116				85	30	4.3	4.5	0.64	2.15	24.0	96.9	96.2	-0.7	90.4
				0		40.2	41.5	1.18	2.80		94.4		1.8	87.8
117		1000	0.304	0	20	8.6	13.3	0.47	3.90	24.7	97.7	94.2	-3.5	83.8
				50		29.6	42.0	0.56	13.9		97.3		-3.1	59.3
118				0	20	11.8	16.8	0.69	4.00	24.2	96.7	94.3	-2.4	83.5
				100		33.6	39.0	0.60	7.80		97.1		-2.8	72.2
119				30	20	8.2	11.7	0.34	4.73	13.2	98.3	96.8	-1.5	81.0
				30		40.5	45.1	0.92	6.55		95.6		1.2	75.5
120				45	2	14.0	18.4	5.8	11.0	47.2	77.7	46.2	-40.5	64.8
				45		29.5	32.4	11.85	19.10		63.1		-26.7	51.4
121				45	5	12.0	16.1	2.92	7.20	37.3	87.4	73.0	-16.3	73.7
				45		38.8	41.6	4.04	8.90		83.3		-12.3	69.4
122				45	10	11.4	15.2	1.32	4.85	27.4	93.8	88.0	-6.1	80.6
				45		39.6	47.4	1.48	8.20		93.1		-5.4	71.1
123				45	20	8.8	13.2	0.28	2.80	21.7	98.6	94.9	-3.7	87.8
				45		35.4	45.1	0.78	15.6		96.2		-1.4	56.5
124				45	40	3.3	4.7	0.08	1.78	33.0	99.6	96.0	-3.5	91.9
				45		14.5	22.3	0.38	8.40		98.1		-2.1	70.7
125				60	40	3.8	4.9	0.07	1.25	30.7	99.6	96.3	-3.3	94.1
				60		12.2	24.4	0.08	10.65		99.6		-3.2	65.5
126				100	20	7.1	9.4	0.08	3.00	21.6	99.6	94.9	-4.6	87.1
				0		44.2	49.0	1.48	7.30		93.1		1.8	73.5

The upper values apply to the rod, the lower apply to the tube

Table A2. Film Flow Measurements. Test Section 10. Adiabatic. L_a = 9.0 m.

Main System Parameters					Experimental Data				Entr.	Voids			
Run	p	G	m	x_{out}	m_f/m		s_c	s_w	m_e/m	Core			Wave
					Min.	Max.				$\alpha_{c,s}$	$\alpha_{c,m}$	$\Delta\alpha/\alpha_{c,s}$	α_w
	bar	kg/m^2s	kg/s	%	%	%	-	-	%	%	%	%	%
201	30	1000	0.0785	16	40.0	46.5	1.7	3.5	37.5	97.0	95.9	-1.1	94.0
202				24	36.2	38.4	1.41	2.15	37.6	97.5	97.2	-0.3	96.2
203				32	31.6	33.2	0.43	0.8	34.8	99.2	98.1	-1.1	98.6
204				40	20.7	20.7	0.6	?	39.3	98.9	98.2	-0.7	?
205				50	13.2	16.0	0.27	1.48	34.0	99.5	98.8	-0.7	97.4
206				60	7.5	12.4	0.4	4.5	27.6	99.3	99.2	-0.1	92.4
207		2000	0.157	8	26.8	?	?	11.1	?	?	?	?	83.2
208				16	24.0	27.5	1.65	4.1	56.5	97.1	99.5	2.5	93.0
209				20	21.8	23.8	0.38	2.6	56.2	99.3	95.1	-4.2	95.5
210				24	14.8	14.8	0.68	?	61.2	98.8	95.6	-3.2	?
211				32	6.9	9.0	0.59	2.3	59.0	98.9	96.7	-2.2	96.0
212				40	5.0	8.1	0.14	3.8	51.9	99.7	97.7	-2.0	93.5
213				50	4.5	6.7	0.11	3.9	43.3	99.8	98.4	-1.4	93.4
214	50	500	0.0393	24	48.6	?	?	4.47	?	?	?	?	87.3
215				32	44.8	49.4	1.48	2.88	18.6	95.4	98.1	2.8	91.4
216				40	41.9	44.7	1.09	2.60	15.3	96.6	98.8	2.3	92.2
217				50	39.9	44.0	0.38	0.99	6.0	98.8	99.6	0.8	96.9
218				60	35.0	35.0	0.65	?	5.0	97.9	99.7	1.8	?
219		1000	0.0785	8	?	42.2	5.95	?	49.8	83.8	83.1	-0.8	?
220				16	38.4	41.5	1.83	15.1	42.5	94.4	92.0	-2.5	67.0
221				24	36.5	38.8	1.46	3.10	37.2	95.5	95.2	-0.3	90.8
222				32	32.8	34.3	1.06	1.78	33.7	96.7	96.7	0.0	94.5
223				40	29.0	31.0	0.10	0.85	29.0	99.7	97.7	-2.0	97.3
224				50	21.0	21.0	0.34	?	29.0	98.9	98.1	-0.8	?
225				60	12.9	15.1	0.69	1.65	24.9	97.8	98.7	0.9	94.9
226		2000	0.1571	8	24.4	33.0	3.95	18.1	59.0	88.6	80.6	-9.0	62.9
227				16	22.2	?	?	4.65	?	?	?	?	86.8
228				20	20.4	24.3	1.35	4.95	55.7	95.8	91.7	-4.3	86.1
229				24	19.5	21.4	0.76	?	54.6	94.5	92.9	-1.7	?
230				32	14.0	14.0	0.20	?	54.0	99.4	94.8	-4.6	?
231				40	8.4	9.8	0.23	2.60	50.2	99.3	96.1	-3.2	92.2
232				50	4.2	6.6	0.17	4.1	43.4	99.4	97.2	-2.2	88.2
233				60	2.5	5.5	0.08	4.85	34.5	99.7	98.2	-1.5	86.3

Table A2 (continued). Film Flow Measurements. Test Section 10. Adiabatic. L_a = 9.0 m.

Main System Parameters					Experimental Data				Entr.	Voids			
Run	p	G	m	x_{out}	m_f/m		s_c	s_w	m_e/m	Core			Wave
					Min.	Max.				$\alpha_{c,s}$	$\alpha_{c,m}$	$\Delta\alpha/\alpha_{c,s}$	α_w
	bar	kg/m^2s	kg/s	%	%	%	-	-	%	%	%	%	%
234	70	500	0.0393	24	49.2	54.4	1.64	6.0	21.6	92.5	95.7	3.5	77.2
235				32	42.9	47.6	1.21	3.04	20.4	94.4	97.0	2.8	87.0
236				40	40.5	43.0	1.1	1.79	17.0	94.9	97.9	3.2	91.9
237				50	37.3	42.2	0.28	1.64	7.8	98.6	99.2	0.6	92.5
238				60	30.6	35.4	0.30	3.0	4.6	98.5	99.6	1.1	87.1
239		750	0.0589	16	47.0	?	?	5.40	?	?	?	?	79.0
240				24	42.0	44.3	2.35	6.0	31.7	89.6	93.9	4.8	77.2
241				32	39.9	43.2	0.95	1.95	24.8	95.5	96.3	0.8	91.2
242				40	39.1	40.7	0.38	0.61	19.3	98.2	97.7	-0.5	97.1
243				50	32.4	33.5	0.27	1.50	16.5	98.7	98.4	-0.3	93.1
244				60	25.7	28.4	0.24	0.52	11.6	98.8	99.1	0.3	97.5
245		1000	0.0785	8	36.8	?	?	8.10	?	?	?	?	71.4
246				16	37.2	47.8	1.20	6.60	36.2	94.4	90.0	-4.7	75.4
247				24	33.8	38.3	1.34	7.10	37.7	93.8	92.8	-1.1	74.1
248				32	31.7	34.2	0.61	1.25	33.8	97.1	95.0	-2.2	94.2
249				40	27.0	28.8	0.31	3.70	31.2	98.5	96.3	-2.2	84.6
250				50	19.0	21.6	0.09	5.80	28.4	99.6	97.3	-2.3	77.8
251				60	14.7	14.7	0.70	?	25.3	96.7	98.0	1.3	?
252		2000	0.157	8	34.2	?	?	3.13	?	?	?	?	86.6
253				12	22.0	26.0	4.00	9.25	62.0	83.5	79.7	-4.6	68.7
254				16	20.0	23.2	2.20	9.30	60.8	84.4	84.0	-0.5	68.5
255				20	20.0	22.0	2.00	3.30	58.0	95.0	88.0	-7.9	86.0
256				24	18.0	18.9	1.33	3.10	57.1	93.8	89.5	-4.6	86.7
257				32	?	13.3	0.38	?	54.7	98.2	92.2	-6.1	?
258				40	9.0	10.0	0.13	1.40	50.0	99.4	94.2	-5.2	93.5
259				50	5.0	7.3	0.04	1.33	42.7	99.8	96.0	-3.8	93.8
260				60	3.5	5.3	0.05	2.00	34.7	99.8	97.2	-2.6	91.0
261		3000	0.2356	8	18.5	23.1	3.23	7.15	68.9	86.3	70.2	-18.7	73.9
262				16	14.3	17.0	1.64	3.50	67.0	92.5	82.9	-10.4	85.3
263				24	11.5	11.5	1.08	?	64.5	94.9	88.3	-7.0	?
264				32	7.3	9.0	0.26	0.75	59.0	98.7	91.7	-7.1	96.4
265				40	5.0	7.7	0.10	1.35	52.3	99.5	93.9	-5.6	93.8
266	90	500	0.0393	50	37.0	39.1	0.62	1.30	10.9	95.9	98.5	2.7	91.7
267				60	33.1	35.2	0.28	0.94	4.8	98.1	99.4	1.3	93.9
268		1000	0.0785	16	39.7	41.8	2.36	4.8	42.2	86.0	84.6	-1.6	75.1
269				24	29.2	34.5	0.84	3.38	41.5	94.5	89.3	-5.5	81.0
270				32	25.7	28.0	0.45	1.75	40.0	97.0	92.0	-5.2	89.2
271				40	22.5	24.2	0.25	1.25	35.8	98.3	94.2	-4.2	92.0
272				50	18.2	18.2	0.12	?	31.8	99.2	95.8	-3.4	?
273				60	13.5	13.5	0.14	?	26.5	99.0	97.0	-2.0	?
274		2000	0.157	8	27.7	31.9	4.76	6.65	60.1	75.2	65.8	-12.5	68.5
275				16	17.8	?	?	3.91	?	?	?	?	78.7
276				20	16.7	?	?	1.95	?	?	?	?	88.1
277				24	15.3	16.9	0.925	2.6	59.1	94.0	85.4	-9.1	84.8
278				32	10.7	?	?	0.48	?	?	?	?	96.8
279				40	7.3	9.5	0.16	0.75	50.5	98.9	92.0	-7.0	95.1
280				50	6.9	6.9	0.03	?	43.1	99.8	94.4	-5.4	?
281				60	3.6	5.3	0.07	1.05	34.7	99.5	96.2	-3.3	93.2

Table A3. Film Flow Measurements. Test Section 10. Diabatic. L_a = 0.1 m.

Run	Main System Parameters						Experimental Data				Entr.	Voids				
							m_f/m		s_c	s_w	m_e/m	Core			Wave	Predict.
							Min.	Max.				$\alpha_{c,s}$	$\alpha_{c,m}$	$\Delta\alpha/\alpha_{c,s}$	α_w	x_{BO}
	bar	kg/m²s	kg/s	W/cm²	m	%	%	%	-	-	%	%	%	%	%	%
301	30	1000	0.0785	100	4.020	50	15.0	17.6	0.58	1.44	32.4	98.9	98.8	-0.1	97.4	67.9
302		2000	0.157	100	4.020	24	21.8	24.5	0.64	1.94	51.5	98.8	96.2	-2.6	96.5	45.0
303		3000	0.236	100	4.020	24	13.6	14.5	0.44	1.35	61.5	99.2	95.5	-3.2	97.5	36.6
304	50	1000	0.0785	100	4.020	50	18.3	18.3	0.86	?	31.7	97.2	97.9	0.7	?	74.2
305		2000	0.157	100	4.020	24	21.4	24.3	0.96	2.38	51.7	96.9	93.4	-3.6	92.8	49.7
306		3000	0.236	100	4.020	24	13.8	13.8	0.83	?	62.2	97.3	92.2	-5.2	?	40.7
307	70	500	0.0393	50	2.000	24	47.9	52.9	1.98	4.15	23.1	91.1	95.4	4.7	83.0	(102.6)
308				50	2.000	32	45.1	46.7	1.65	2.93	21.3	92.4	96.8	4.7	87.3	(102.6)
309				50	4.020	40	40.4	43.2	0.83	2.25	16.8	96.0	97.9	1.9	90.0	103.8
311				50	4.020	80	15.2	15.2	?	?	4.8	?	99.7	?	?	103.8
312				100	2.000	60	30.1	30.1	?	?	9.9	?	99.1	?	?	(102.1)
313				100	2.000	80	17.9	17.9	?	?	2.1	?	99.8	?	?	(102.1)
314		1000	0.0785	50	4.020	16	42.7	51.8	1.15	6.03	32.2	93.0	93.0	0.0	77.0	75.8
315				50	4.020	24	37.6	43.7	1.38	2.47	32.3	93.6	93.7	0.1	89.1	75.8
316				50	6.000	24	37.4	46.0	0.55	2.27	30.0	97.3	94.1	-3.2	89.9	77.6
317				50	4.020	40	27.8	28.8	0.43	0.75	31.2	97.9	96.2	-1.6	96.4	75.8
318				50	6.000	40	26.4	28.2	0.35	0.93	31.8	98.3	96.2	-2.1	95.6	77.6
319				50	6.000	60	10.2	14.8	0.12	1.55	25.2	99.4	97.9	-1.4	92.8	77.6
320				100	2.000	16	47.4	53.5	1.25	7.6	30.5	94.1	91.4	-2.9	72.7	(73.9)
321				100	2.000	24	38.0	49.3	0.88	3.85	26.7	95.8	94.7	-1.0	84.0	(73.9)
322				100	2.000	32	34.2	36.4	1.13	3.05	31.6	94.7	95.3	0.6	86.9	(73.9)
323				100	4.020	40	27.5	27.5	0.39	?	32.5	98.1	96.1	-2.0	?	70.8
324				100	4.020	50	19.4	19.4	0.05	?	30.6	99.7	97.0	-2.6	?	70.8
325				100	4.020	60	10.0	12.4	0.05	0.90	27.6	99.7	97.7	-1.9	95.7	70.8
326		2000	0.157	50	4.020	16	24.7	29.2	1.62	5.15	54.8	92.5	85.5	-7.6	79.7	50.7
327				50	4.020	24	19.2	22.4	0.72	1.78	53.6	96.5	90.0	-6.7	91.9	50.7
328				100	2.000	16	26.7	30.7	3.20	6.50	53.3	86.3	85.8	-0.5	75.7	45.0
329				100	2.000	24	20.4	23.4	1.00	2.35	52.6	95.2	90.2	-5.3	89.6	45.0
330				100	4.020	24	21.0	22.1	1.24	1.70	53.9	94.2	90.0	-4.4	92.2	46.9
331				100	6.000	24	19.5	22.5	0.85	1.77	53.5	95.9	90.0	-6.1	91.9	48.4
332				100	4.020	32	13.2	13.2	0.35	?	54.8	98.3	92.2	-6.1	?	46.9
333				100	4.020	40	6.6	6.6	0.63	?	53.4	96.9	93.8	-3.2	?	46.9
334				100	6.000	40	6.6	6.6	0.24	?	53.4	98.8	93.8	-5.0	?	48.4
335				150	4.020	16	28.6	36.2	1.15	6.40	47.8	94.6	87.1	-7.9	76.0	43.2
336				150	4.020	24	19.4	22.0	0.97	2.13	54.0	95.4	90.0	-5.6	90.4	43.2
337				150	4.020	32	11.8	12.2	0.19	1.68	55.8	99.0	92.0	-7.0	92.3	43.2
338		3000	0.236	100	4.020	24	11.7	11.7	0.98	?	64.3	95.3	88.3	-7.4	?	39.0
339				100	4.020	32	5.5	5.5	1.30	?	62.5	93.9	91.2	-2.9	?	39.0
340				150	4.020	16	18.0	20.5	2.32	4.65	63.5	89.7	83.6	-6.8	83.3	35.0
341				150	4.020	24	11.5	11.5	0.65	?	64.5	96.8	88.2	-8.8	?	35.0
342				150	6.000	24	10.4	10.4	0.95	?	65.6	95.4	88.1	-7.7	?	36.1
343				150	4.020	29	7.5	7.5	0.20	?	63.5	99.0	90.2	-8.8	?	35.0
344	90	1000	0.0785	100	4.020	50	9.6	13.8	0.18	1.40	36.2	98.7	95.2	-3.5	91.1	58.9
345		3000	0.236	100	4.020	24	9.0	9.0	0.97	?	67.0	93.7	83.8	-10.5	?	33.4

Table A4. Film Flow Measurements. Test Section 10. Diabatic. L_a = 0.5 m.

	Main System Parameters						Experimental Data				Entr.	Voids			
Run	p	G	m	q"	L_d	x_{out}	m_f/m Min.	m_f/m Max.	s_c	s_w	m_e/m	Core $\alpha_{c,s}$	Core $\alpha_{c,m}$	Core $\Delta\alpha/\alpha_{c,s}$	Wave α_w
	bar	kg/m^2s	kg/s	W/cm^2	m	%	%	%	-	-	%	%	%	%	%
346	30	1000	0.0785	100	4.000	50	12.1	14.7	0.090	0.75	35.3	99.8	98.7	-1.1	98.6
347		2000	0.157	100	4.000	24	21.1	23.2	0.53	1.04	52.8	99.0	96.1	-2.9	98.1
348	50	1000	0.0785	100	4.000	50	18.4	19.6	0.045	0.36	30.4	99.8	98.0	-1.7	98.8
349		2000	0.157	100	4.000	24	20.6	24.0	0.84	2.64	52.0	97.3	93.4	-4.0	92.0
350	70	500	0.0393	50	4.000	60	30.7	34.0	0.060	0.99	6.0	99.7	99.5	-0.1	95.3
351		1000	0.0785	100	4.000	60	12.0	14.0	0.17	0.58	26.0	99.1	97.9	-1.2	97.2
352		2000	0.157	150	4.000	16	28.0	30.5	1.98	3.50	53.5	91.1	85.8	-5.7	85.2
353		2000	0.157	100	4.000	40	8.5	9.0	0.30	0.93	51.0	98.5	94.0	-4.5	95.6
354		3000	0.236	100	4.000	32	8.2	8.2	0.58	?	59.8	97.2	91.5	-5.8	?
355	90	1000	0.785	100	4.000	50	11.7	13.5	0.017	0.53	36.5	99.8	95.1	-4.6	96.4
356		2000	0.157	100	4.000	24	16.4	18.0	1.00	2.07	58.0	93.5	85.6	-8.3	87.4

Table A5. Film Flow Measurements. Test Section 10. Diabatic. L_a = 1.0 m.

	Main System Parameters						Experimental Data				Entr.	Voids			
Run	p	G	m	q"	L_d	x_{out}	m_f/m Min.	m_f/m Max.	s_c	s_w	m_e/m	Core $\alpha_{c,s}$	Core $\alpha_{c,m}$	Core $\Delta\alpha/\alpha_{c,s}$	Wave α_w
	bar	kg/m^2s	kg/s	W/cm^2	m	%	%	%	-	-	%	%	%	%	%
357	30	1000	0.0785	100	4.000	50	13.0	16.6	0.038	1.06	33.4	99.9	98.7	-1.1	98.1
358		2000	0.157	100	4.000	24	19.9	22.1	0.24	0.71	53.9	99.5	96.0	-3.5	98.7
359	50	1000	0.0785	100	4.000	50	19.2	21.3	0.33	0.68	28.7	98.9	98.1	-0.7	97.8
360		2000	0.157	100	4.000	24	19.9	23.7	0.66	2.80	52.3	97.8	93.3	-4.6	91.6
361	70	500	0.0393	50	4.000	60	30.0	36.4	0.24	1.44	3.6	98.8	99.7	0.8	93.3
362		1000	0.0785	50	4.000	16	39.0	50.0	1.20	4.25	34.0	95.5	90.7	-5.0	82.6
363		1000	0.0785	100	4.000	60	12.5	18.3	0.29	1.80	21.7	98.5	98.2	-0.3	91.8
364		2000	0.157	150	4.000	16	24.5	30.4	1.54	4.25	53.6	92.9	85.8	-7.6	82.6
365		2000	0.157	100	4.000	40	9.8	11.5	0.25	0.68	48.5	98.7	94.3	-4.4	96.7
366		3000	0.236	100	4.000	32	8.0	8.0	0.63	?	60.0	96.9	91.5	-5.6	?
367	90	1000	0.0785	100	4.000	50	13.2	17.1	0.15	0.88	32.9	98.9	95.6	-3.3	94.2
368		2000	0.157	100	4.000	24	16.2	16.2	0.91	?	59.8	94.0	85.2	-9.3	?

Table A6. Film Flow Measurements. Test Section 10. Diabatic. L_a = 2.0 m.

Run	Main System Parameters						Experimental Data				Entr.	Voids			
	p	G	m	q"	L_d	x_{out}	m_f/m		s_c	s_w	m_e/m	Core			Wave
							Min.	Max.				$\alpha_{c,s}$	$\alpha_{c,m}$	$\Delta\alpha/\alpha_{c,s}$	α_w
	bar	kg/m^2s	kg/s	W/cm^2	m	%	%	%	-	-	%	%	%	%	%
369	30	1000	0.0785	100	4.000	50	12.2	15.2	0.035	0.89	34.8	99.9	98.7	-1.1	98.4
370		2000	0.157	100	4.000	24	17.0	18.2	0.44	2.58	57.8	99.2	95.7	-3.4	95.5
371	50	1000	0.0785	100	4.000	50	19.4	20.0	0.080	0.18	30.0	99.7	98.0	-1.6	99.4
372		2000	0.157	100	4.000	24	20.3	22.2	0.77	1.32	53.8	97.5	93.1	-4.4	95.8
373	70	500	0.0393	50	4.000	60	29.6	33.8	0.11	1.03	6.2	99.4	99.4	0.03	95.1
374		1000	0.0785	100	4.000	60	13.0	20.2	0.10	1.65	19.8	99.5	98.3	-1.1	92.4
375		2000	0.157	150	4.000	16	22.4	26.3	1.85	5.15	57.7	91.6	84.8	-7.3	79.7
376		2000	0.157	100	4.000	40	9.3	11.3	0.35	0.93	48.7	98.3	94.3	-4.0	95.6
377		3000	0.236	100	4.000	32	7.7	7.7	0.68	?	60.3	96.2	91.4	-5.4	?
378	90	1000	0.0785	100	4.000	50	16.2	16.2	0.20	?	33.8	98.6	95.5	-3.1	?
379		2000	0.157	100	4.000	24	15.3	15.3	1.09	?	60.7	92.9	85.1	-8.4	?

Table A7. Film Flow Measurements. Test Section 17/26L. Adiabatic. L_a = 8.0 m.

Run	Main System Parameters				Experimental Data				Entr.	Voids			
	p	G	m	x_{out}	m_f/m		s_c	s_w	m_e/m	Core			Wave
					Min.	Max.				$\alpha_{c,s}$	$\alpha_{c,m}$	$\Delta\alpha/\alpha_{c,s}$	α_w
	bar	kg/m^2s	kg/s	%	%	%	-	-	%	%	%	%	%
501	30	500	0.152	20	9.1	13.6	0.60	4.05	16.3	98.9	98.5	-0.3	93.1
					45.7	50.1	0.94	2.85		98.3		0.2	95.0
502				40	6.8	11.2	0.22	3.10	16.8	99.6	99.2	-0.3	94.6
					21.9	32.0	0.16	4,85		99.7		-0.4	91.8
503				50	5.9	8.8	0.16	3.25	17.9	99.7	99.3	-0.3	94.3
					14.1	23.3	0.06	5.95		99.8		-0.5	90.2
504		1000	0.304	20	6.6	10.2	0.34	4.55	31.3	99.3	97.2	-2.1	92.3
					26.1	38.5	0.62	10.30		98.8		-1.6	84.1
505				40	2.2	3.3	0.04	2.40	46.3	99.9	97.9	-1.9	95.8
					6.2	10.4	0.04	2.70		99.9		-1.9	95.3
506	50	500	0.152	40	7.2	11.8	0.16	2.10	11.4	99.4	99.0	-0.4	93.5
					28.0	36.8	0.32	4.20		98.9		0.1	87.9
507		1000	0.304	20	7.6	10.9	0.42	2.20	26.3	98.6	95.8	-2.7	93.3
					31.6	42.8	1.04	13.4		96.7		-0.8	69.6
508				40	3.4	5.8	0.08	3.5	38.3	99.7	96.9	-2.7	90.9
					9.8	15.9	0.18	4.40		99.4		-2.4	87.4
509				55	2.14	2.31	0.014	0.11	34.2	99.9	98.0	-1.9	99.6
					3.4	8.5	0.10	5.20		99.6		-1.6	85.5

The upper values apply to the rod, the lower apply to the tube.

Table A7 (continued). Film Flow Measurements. Test Section 17/26L. Adiabatic. L_a = 8.0 m.

Run	Main System Parameters				Experimental Data				Entr.	Voids			
	p	G	m	x_{out}	m_f/m		s_c	s_w	m_e/m	Core			Wave
					Min.	Max.				$\alpha_{c,s}$	$\alpha_{c,m}$	$\Delta\alpha/\alpha_{c,s}$	α_w
	bar	kg/m^2s	kg/s	%	%	%	-	-	%	%	%	%	%
510	70	400	0.122	61	6.9	11.1	0.020	2.15	-0.8	99.9	100.0	0.1	90.4
					26.6	28.7	0.16	2.30		99.2		0.8	89.8
511		500	0.152	20	8.3	13.1	0.86	3.25	21.9	95.9	94.8	-1.0	86.1
					43.3	45.0	1.56	6.25		92.8		2.1	76.9
512				30	7.8	11.0	0.60	2.90	13.5	97.1	97.8	0.7	87.4
					38.8	45.5	0.38	6.00		98.1		-0.3	77.1
513				40	7.4	11.2	0.24	2.40	9.7	98.8	98.8	0	89.4
					35.2	39.1	0.40	1.80		98.0		0.7	91.8
514				50	6.1	9.3	0.24	2.25	10.7	98.8	98.9	0.1	90.0
					23.1	30.0	0.060	4.10		99.7		-0.7	83.1
515				60	5.3	8.7	0.14	2.10	7.2	99.3	99.4	0.1	90.6
					17.3	24.1	0.12	4.00		99.4		0	83.5
516		800	0.243	30	6.6	9.3	0.42	2.45	22.2	97.9	96.4	-1.5	89.2
					33.2	38.5	0.54	4.70		97.4		-0.9	81.1
517				50	4.0	6.7	0.060	2.05	25.6	99.7	97.5	-2.1	90.8
					11.9	17.7	0.060	3.40		99.7		-2.1 *	85.6
518		1000	0.304	20	6.2	9.8	0.52	3.35	24.0	97.4	94.4	-3.1	85.8
					37.2	46.2	0.72	4.60		96.5		-2.2	81.5
519				30	5.3	8.2	0.16	2.15	29.8	99.2	95.3	-3.9	90.4
					23.6	32.0	0.16	9.75		99.2		-3.9	67.5
520				40	4.2	6.4	0.12	1.90	35.0	99.4	95.8	-3.5	91.4
					12.8	18.6	0.060	3.15		99.7		-3.8	86.5
521				50	2.0	3.4	0.20	2.00	34.8	99.0	96.6	-2.3	91.0
					7.1	11.8	0.040	3.45		99.8		-3.1	85.4
522				60	0.94	1.45	0.078	0.49	30.7	99.6	97.5	-2.0	97.6
					4.6	7.9	0.020	2.35		99.9		-2.3	89.6
523		1400	0.426	15	6.4	8.7	0.98	4.05	36.5	95.3	89.2	-6.4	83.3
					34.0	39.8	2.06	7.60		90.7		-1.6	72.7
524				20	5.7	7.2	0.62	1.75	33.5	97.0	92.3	-4.8	92.0
					30.1	39.3	0.46	6.30		97.7		-5.5	76.2
525		2000	0.608	20	4.60	5.50	0.11	0.65	49.8	99.4	89.0	-10.4	96.8
					22.0	24.7	0.62	3.85		97.0		-8.2	84.0
526				28	2.00	2.90	0.21	1.38	55.4	98.9	91.1	-7.9	93.6
					9.3	13.7	0.22	3.85		98.9		-7.9	84.0
527				35	0.65	1.23	0.25	1.18	55.5	98.7	92.7	-6.1	94.4
					5.6	8.3	0.32	2.40		98.4		-5.7	89.4
528	90	1000	0.304	20	6.2	9.2	0.48	2.90	29.0	96.7	90.8	-6.1	83.2
					34.8	41.8	1.40	5.85		91.1		-0.3	71.1
529				40	3.4	5.6	0.12	1.90	39.4	99.1	93.6	-5.6	88.3
					12.0	15.0	0.16	2.80		98.9		-5.3	83.7

The upper values apply to the rod, the lower apply to the tube.

Table A8. Film Flow Measurements. Test Section 20. Adiabatic. L_a = 9.0 m.

Run	Main System Parameters				Experimental Data				Entr.	Voids			
	p	G	m	x_{out}	m_f/m		s_c	s_w	m_e/m	Core			Wave
					Min.	Max.				$\alpha_{c,s}$	$\alpha_{c,m}$	$\Delta\alpha/\alpha_{c,s}$	α_w
	bar	kg/m^2s	kg/s	%	%	%	-	-	%	%	%	%	%
601	70	500	0.1571	20	29.0	40.1	1.75	6.85	39.9	92.0	91.0	-1.1	74.7
602				30	22.4	34.8	1.70	10.80	35.2	92.2	94.5	2.4	65.2
603				40	20.0	29.8	1.30	3.73	30.2	93.9	96.4	2.5	84.4
604				50	16.8	26.0	0.70	3.20	24.0	96.6	97.6	1.0	86.3
605				60	15.2	21.5	0.48	2.27	18.5	97.6	98.5	0.8	89.9
606				70	13.5	18.7	0.20	1.65	11.3	99.0	99.2	0.1	92.4
607		750	0.236	20	21.6	34.4	1.87	10.0	45.6	91.5	89.8	-1.8	66.9
608				30	17.6	30.0	1.08	8.20	40.0	94.9	93.8	-1.1	71.1
609				40	16.0	25.2	0.53	4.15	34.8	97.4	95.8	-1.6	83.0
610				50	13.7	17.7	0.45	2.03	32.3	97.8	96.9	-0.9	90.8
611				60	11.9	14.3	0.18	1.25	25.7	99.1	97.9	-1.1	94.1
612				70	8.9	10.3	0.12	0.65	19.7	99.4	98.6	-0.7	96.8
613		1000	0.314	20	20.2	29.4	1.65	5.55	50.6	92.4	88.9	-3.8	78.5
614				30	13.8	23.5	0.83	6.30	46.5	96.0	92.8	-3.2	76.2
615				40	12.0	16.3	0.45	1.82	43.7	97.8	94.8	-3.0	91.7
616				50	9.5	11.8	0.25	2.22	38.2	98.7	96.3	-2.4	90.1
617				60	7.1	7.7	0.22	1.10	32.3	98.9	97.4	-1.5	94.8
618				70	4.3	4.7	0.18	1.35	25.3	99.1	98.2	-0.8	93.7
619		2000	0.628	20	9.7	16.3	1.50	9.00	63.7	93.1	86.4	-7.1	69.2
620				30	7.3	8.8	0.77	3.08	61.2	96.3	90.8	-5.6	86.8
621				40	4.3	4.9	0.42	1.13	55.1	97.9	93.6	-4.4	94.7

Table A9. Pressure Drop Measurements. Test Section 17/26S. Diabatic.

Run	p	G	$q_1"$	$q_2"$	x_{out}	$(\frac{dp}{dz})_{tot}$	$(\frac{dp}{dz})_f$	ϕ^2
	bar	kg/m^2s	W/cm^2	W/cm^2	%	kPa/m	kPa/m	-
101	70	500	0	50	20	7.0	4.0	8.0
102			10	40	20	6.6	3.8	7.7
103			20	30	20	6.7	3.8	7.7
104			30	20	20	6.6	3.8	7.7
105			40	10	20	6.4	3.7	7.4
106			50	0	20	6.1	3.4	6.8
107		600	40	40	60	14.6	11.8	17.0
108			60	60	60	16.1	12.3	17.7
109			66	66	60	16.6	12.3	17.8
110		900	0	85	20	15.0	10.5	7.5
111					30	19.2	15.0	10.7
112					40	22.6	18.7	13.0
113					50	24.8	20.5	14.5
114			85	0	20	13.3	9.7	6.9
115					25	15.0	11.6	8.1
116					30	16.0	12.8	9.0
117		1000	0	50	20	16.7	13.2	7.9
118			0	100	20	18.8	13.5	7.9
119			30	30	30	16.3	12.5	7.4
120			45	45	2	11.1	3.5	2.0
121					5	11.7	5.1	2.9
122					10	13.1	7.8	4.5
123					20	17.3	12.8	7.5
124					40	24.3	20.2	11.9
125			60	60	40	25.7	20.5	12.2
126			100	0	20	16.5	12.3	7.2

Table A10. Pressure Drop Measurements. Test Section 10. Adiabatic.

Run	p	G	x_{out}	$(\frac{dp}{dz})_{tot}$ (1 m)	$(\frac{dp}{dz})_{f}$ (4 m)	$(\frac{dp}{dz})_{f}$ (1 m)	ϕ^2 (1 m)
	bar	$kg/m^2 s$	%	kPa/m	kPa/m	kPa/m	-
201	30	1000	16	15.2	14.1	13.7	9.8
202			24	22.4	21.4	21.3	15.1
203			32	27.2	26.6	26.3	18.7
204			40	30.4	29.9	29.6	21.0
205			50	35.9	35.4	35.1	24.9
206			60	42.8	42.0	41.9	29.8
207		2000	8	25.9	23.5	23.5	5.0
208			16	42.5	40.7	40.6	8.6
209			20	46.8	45.0	44.9	9.5
210			24	48.8	47.2	46.9	9.9
211			32	57.7	55.6	55.5	11.7
212			40	68.5	65.8	65.8	13.9
213			50	85.7	81.8	81.9	17.3
214	50	500	24	5.3	3.1	3.5	8.1
215			32	6.1	4.6	4.6	10.7
216			40	7.6	6.5	6.5	15.0
217			50	9.1	8.2	8.1	18.8
218			60	10.7	10.1	9.9	23.0
219		1000	8	7.6	4.7	4.6	3.2
220			16	10.5	8.8	8.5	5.9
221			24	14.6	13.3	13.2	9.1
222			32	18.1	16.7	16.9	11.7
223			40	21.5	20.6	20.5	14.2
224			50	25.1	24.5	24.3	16.8
225			60	29.6	29.1	28.9	19.9
226		2000	8	17.7	15.2	14.8	3.0
227			16	27.6	26.0	25.6	5.3
228			20	32.1	30.5	30.4	6.2
229			24	34.7	33.5	33.1	6.8
230			32	41.4	40.2	39.9	8.1
231			40	50.5	49.2	49.1	10.1
232			50	59.5	58.3	58.0	11.9
233			60	71.0	69.3	69.3	14.3
234	70	500	24	4.8	2.3	2.7	6.1
235			32	4.9	3.0	3.2	7.3
236			40	5.5	3.8	4.1	9.3
237			50	6.6	5.3	5.4	12.4
238			60	7.4	6.5	6.4	14.5
239		750	16	6.2	3.7	3.8	4.3
240			24	7.2	5.4	5.3	5.9
241			32	8.6	7.3	7.1	8.0
242			40	9.9	8.8	8.7	9.7
243			50	12.0	11.1	10.9	12.3
244			60	13.9	13.3	13.0	14.6

Table A10 (continued). Pressure Drop Measurements. Test Section 10. Adiabatic.

Run	p	G	x_{out}	$(\frac{dp}{dz})_{tot}$ (1 m)	$(\frac{dp}{dz})_{f}$ (4 m)	$(\frac{dp}{dz})_{f}$ (1 m)	ϕ^2 (1 m)
	bar	kg/m^2s	%	kPa/m	kPa/m	kPa/m	-
245	70	1000	8	7.3	3.8	3.9	2.6
246			16	8.6	6.3	6.2	4.2
247			24	10.5	8.8	8.7	5.9
248			32	12.7	11.4	11.2	7.6
249			40	14.7	13.6	13.5	9.1
250			50	17.6	16.7	16.6	11.2
251			60	20.4	19.8	19.6	13.3
252		2000	8	13.2	9.6	9.5	1.9
253			12	17.5	14.9	14.8	3.0
254			16	20.0	18.0	17.7	3.6
255			20	22.3	20.8	20.3	4.1
256			24	24.7	23.3	22.9	4.6
257			32	29.3	28.2	27.8	5.6
258			40	34.9	34.0	33.6	6.8
259			50	42.7	41.9	41.5	8.4
260			60	50.5	49.7	49.3	9.8
261		3000	8	25.5	22.0	22.0	2.2
262			16	35.7	33.8	33.2	3.3
263			24	44.3	42.6	42.2	4.2
264			32	51.4	49.9	49.4	4.9
265			40	61.5	59.8	59.5	5.9
266	90	500	50	5.2	3.5	3.8	8.4
267			60	5.8	4.3	4.6	10.2
268		1000	16	7.6	4.9	4.9	3.2
269			24	8.2	6.1	6.1	4.0
270			32	9.1	7.4	7.4	4.8
271			40	10.5	9.1	9.0	5.9
272			50	12.2	11.2	11.0	7.3
273			60	14.4	13.5	13.4	8.8
274		2000	8	13.2	9.6	9.5	1.9
275			16	15.7	13.1	13.1	2.6
276			20	16.4	14.3	14.2	2.8
277			24	17.1	15.2	15.1	3.0
278			32	21.1	19.7	19.4	3.8
279			40	24.9	23.9	23.5	4.6
280			50	31.0	30.0	29.7	5.8
281			60	35.9	34.9	34.8	6.8

Table A11. Pressure Drop Measurements. Test Section 10. Diabatic.

Run	p	G	q"	x_{out}	$(\frac{dp}{dz})_{tot}$	$(\frac{dp}{dz})_{f}$	ϕ^2
	bar	kg/m^2 s	W/cm^2	%	kPa/m	kPa/m	-
309	70	500	50	40	8.3	5.6	12.4
310				60	10.2	7.2	16.5
311				80	12.3	9.3	19.6
314		1000	50	16	12.6	7.7	5.4
315				24	15.0	10.6	7.2
317				40	19.6	15.2	10.3
323			100	40	25.6	18.1	12.3
324				50	28.2	20.3	13.8
325				60	28.7	20.4	14.0
326		2000	50	16	36.2	28.0	5.8
327				24	39.7	32.0	6.5
330			100	24	44.7	31.5	6.4
332				32	48.8	35.3	7.2
333				40	47.0	33.0	6.6
335			150	16	41.0	22.0	4.4
336				24	53.4	34.7	7.0
337				32	58.0	38.3	7.8
338		3000	100	24	68.8	48.8	4.9
339				32	71.5	51.5	5.1
340			150	16	69.6	41.8	4.1
341				24	80.5	52.3	5.2
343				29	79.8	49.7	4.9

Table A12. Pressure Drop Measurements. Test Section 17/26L. Adiabatic.

Run	p	G	x_{out}	$(\frac{dp}{dz})_{tot}$ (1 m)	$(\frac{dp}{dz})_{f}$ (3.5 m)	$(\frac{dp}{dz})_{f}$ (1 m)	ϕ^2 (1 m)
	bar	$kg/m^2 s$	%	kPa/m	kPa/m	kPa/m	-
501	30	500	20	7.6	6.0	6.0	12.6
502			40	14.0	13.0	13.2	27.4
503			50	17.2	16.3	16.5	34.2
504		1000	20	22.6	21.4	21.4	13.2
505			40	34.8	33.1	33.9	20.9
506	50	500	40	9.3	8.1	8.1	16.4
507		1000	20	15.7	13.9	14.0	8.4
508			40	24.3	22.8	23.4	14.0
509			55	31.8	30.4	31.1	18.6
510	70	400	61	7.0	5.7	5.9	17.4
511		500	20	5.1	2.7	2.9	5.7
512			30	6.1	4.1	4.3	8.6
513			40	7.0	5.5	5.6	11.2
514			50	8.5	7.2	7.3	14.6
515			60	9.3	8.2	8.4	16.7
516		800	30	11.4	9.6	9.8	8.5
517			50	15.4	14.1	14.4	12.6
518		1000	20	12.1	9.8	10.1	5.9
519			30	15.0	13.3	13.5	8.0
520			40	17.4	15.9	16.3	9.6
521			50	20.7	19.4	19.8	11.7
522			60	23.7	22.5	22.9	13.5
523		1400	15	16.3	13.6	14.0	4.6
524			20	18.8	16.4	16.9	5.5
525		2000	20	30.0	27.6	28.0	4.9
526			28	36.1	33.8	34.5	6.1
527			35	42.1	39.8	40.7	7.1
528	90	1000	20	10.2	7.7	7.9	4.5
529			40	13.0	11.3	11.6	6.7

Table A13. Pressure Drop Measurements. Test Section 20. Adiabatic.

Run	p	G	x_{out}	$(\frac{dp}{dz})_{tot}$ (1 m)	$(\frac{dp}{dz})_{f}$ (4 m)	$(\frac{dp}{dz})_{f}$ (1 m)	ϕ^2 (1 m)
	bar	$kg/m^2 s$	%	kPa/m	kPa/m	kPa/m	-
601	70	500	20	3.6	1.1	1.3	6.9
602			30	3.3	1.4	1.6	8.6
603			40	3.5	1.9	2.1	11.3
604			50	3.7	2.3	2.5	14.0
605			60	4.0	2.8	3.1	16.6
606			70	4.4	3.3	3.6	19.4
607		750	20	4.1	1.8	2.0	5.3
608			30	4.4	2.6	2.8	7.4
609			40	4.9	3.4	3.7	9.7
610			50	5.5	4.2	4.5	11.9
611			60	6.1	5.1	5.3	14.1
612			70	7.0	6.1	6.4	16.8
613		1000	20	5.4	3.2	3.5	5.6
614			30	6.1	4.3	4.6	7.4
615			40	6.9	5.4	5.8	9.3
616			50	8.0	6.6	7.0	11.3
617			60	9.2	8.0	8.5	13.6
618			70	10.6	9.5	10.0	16.0
619		2000	20	11.8	9.4	10.0	4.7
620			30	14.1	11.8	12.7	6.0
621			40	17.3	15.0	16.1	7.7

Table A14. Burnout Measurements. Test Section 10.

Run	L_d	p	ΔT_{sub}	G	Q_{BO}	q''_{BO}	x_{BO}
	m	bar	°C	kg/m² s	kW	W/cm²	%
401	2.02	70	10	500	62.4	97.4	98.6
402				1000	87.4	136.4	70.1
403				1500	99.6	155.4	52.0
404				2000	109.8	171.3	42.5
405				2500	117.9	183.9	36.2
406				3000	124.7	194.6	31.4
407	4.02	30	10	500	70.6	55.3	94.3
408				1000	99.9	78.3	67.1
409				1500	116.2	91.1	51.7
410				2000	134.2	105.2	44.9
411				2500	150.9	118.3	40.2
412				3000	166.7	130.7	36.6
413			100	500	85.4	67.0	91.8
414				1000	130.7	102.5	66.6
415				1500	166.3	130.4	51.8
416				2000	197.3	154.7	44.8
417				2500	230.7	180.9	40.3
418				3000	263.2	206.3	36.5
419		50	10	500	69.4	54.4	100.2
420				1000	101.9	79.9	75.2
421				1500	119.4	93.6	58.3
422				2000	135.4	106.2	49.3
423				2500	149.2	117.0	43.3
424				3000	165.1	129.4	39.1
425			100	500	84.4	66.2	97.7
426				1000	131.5	103.1	72.8
427				1500	163.0	127.8	56.0
428				2000	196.6	154.1	47.5
429				2500	222.3	174.3	41.5
430				3000	253.0	198.3	36.6
431		70	10	500	63.6	49.9	100.8
432				1000	91.1	71.4	73.7
433				1500	106.2	83.3	56.2
434				2000	120.3	94.3	47.4
435				2500	134.4	105.4	41.8
436				3000	146.5	114.9	38.3
437			100	500	76.9	60.3	96.2
438				1000	121.8	95.5	70.7
439				1500	152.0	119.2	51.7
440				2000	179.3	140.6	44.3
441				2500	205.8	161.3	38.2
442				3000	229.0	179.5	33.1

Table A14 (continued). Burnout Measurements. Test Section 10.

Run	L_d	p	ΔT_{sub}	G	Q_{BO}	q''_{BO}	x_{BO}
	m	bar	°C	kg/m² s	kW	W/cm²	%
443	4.02	90	10	500	54.6	42.8	92.7
444				1000	72.6	56.9	61.7
445				1500	83.8	65.7	46.8
446				2000	96.9	76.0	40.1
447				2500	110.2	86.4	36.2
448				3000	123.8	97.1	33.8
449			100	500	72.0	56.4	91.0
450				1000	104.7	82.1	60.4
451				1500	131.9	103.4	45.7
452				2000	157.3	123.3	37.8
453				2500	183.1	143.5	31.6
454				3000	200.1	157.7	25.4
455	6.00	70	10	500	62.6	32.9	100.7
456				1000	95.7	50.3	76.9
457				1500	115.1	60.5	61.2
458				2000	135.3	71.1	53.5
459				2500	148.2	77.8	47.2
460				2885	163.2	85.7	44.0
461			100	500	80.3	42.2	98.2
462				1000	127.7	67.1	74.9
463				1500	159.1	83.6	59.4
464				2000	190.0	99.8	49.4
465				2500	222.6	116.9	42.4
466				3000	248.2	130.4	38.8
467	8.00	70	10	1000	98.3	38.7	78.6
468				1500	123.5	48.7	64.9
469				2000	147.0	57.9	58.5
470				2500	170.4	67.1	53.7
471				2900	186.6	73.5	50.1

Table A15. Measurements of Rod Film Thic ness, Wave Frequency and Velocity
Test Section 17/26L. Adiabatic.

Main System Parameters				Rod Film Thickness Measurements						Wave Measurements				
Run	p	G	x_{out}	y(90%)	y(50%)	y(10%)	$y(\tau_{min})$	τ_{min}	δ_l	f_l	Δf_l	v_{wl}	k_{wl}	λ_{wl}
	bar	kg/m^2s	%	µm	µm	µm	µm	%	µm	s^{-1}	s^{-1}	ms^{-1}	m^{-1}	m
501	30	500	20	40	130	400	1200	0.6	182	30	5-95	4.0	47	0.133
502			40	35	75	280	900	0.1	126	70	10-270	4.8	91	0.069
503			50	15	35	190	700	0.1	77	100	30-450	-	-	-
504		1000	20	35	170	470	1300	1.4	212	40	10-95	5.8	43	0.145
505			40	10	20	90	350	0.0	36	360	50-800	-	-	-
506	50	500	40	45	130	400	1300	0.1	181	40	10-75	4.0	63	0.100
507		1000	20	60	240	700	1300	4.8	278	26	8-60	5.6	29	0.215
508			40	15	50	165	600	0.2	73	150	0-450	-	-	-
509			55	5	15	60	250	0.0	25	400	0-1000	-	-	-
511	70	500	20	50	195	-	1200	13.5	242	10	0-30	2.6	24	0.260
512			30	35	155	660	1200	4.6	221	16	0-55	2.9	35	0.181
513			40	35	120	410	1300	0.7	172	30	0-100	2.8	67	0.093
514			50	25	90	340	1200	0.4	137	40	0-150	3.3	76	0.083
515			60	25	65	240	1000	0.0	106	75	25-215	-	-	-
518		1000	20	45	245	1000	1200	9.4	264	27	10-50	4.8	35	0.178
519			30	30	115	320	750	1.3	150	40	15-90	4.3	58	0.108
520			40	15	65	190	500	0.4	85	100	70-190	4.3	146	0.043
521			50	20	30	110	400	0.1	47	150	0-500	-	-	-
522			60	10	15	60	300	0.0	26	400	0-800	-	-	-
525		2000	20	30	110	280	500	3.5	125	-	-	8.3	-	-
526			28	15	45	130	350	0.2	61	-	-	-	-	-
527			35	5	30	85	400	0.2	41	-	-	-	-	-
528	90	1000	20	40	275	-	1100	18.3	265	22	9-45	4.0	35	0.182
529			40	15	70	230	450	4.0	91	95	25-200	-	-	-

Table A16. Measurements of Film Thickness, Wave Frequency and Velocity . Test Section 20. Adiabatic.

Main System Parameters				Film Thickness Measurements				Wave Measurements				
Run	p	G	x_{out}	y(90%)	y(50%)	y(10%)	δ	f	Δf	v_w	k_w	λ_w
	bar	kg/m^2s	%	µm	µm	µm	µm	s^{-1}	s^{-1}	ms^{-1}	m^{-1}	m
601	70	500	20	250	1050	4000	1570	7	0-18	1.8	23	0.257
602			30	150	620	2100	940	12	3-20	2.2	35	0.183
603			40	100	420	1400	620	18	5-27	2.5	45	0.139
604			50	80	330	1150	500	23	15-30	2.8	52	0.122
605			60	60	280	1000	420	33	18-44	3.1	67	0.094
606			70	50	220	700	320	35	0-65	3.2	69	0.092
607		750	20	250	850	3000	1250	15	5-20	2.6	36	0.173
608			30	170	530	1800	820	21	15-32	3.2	41	0.152
609			40	110	400	1250	580	32	20-40	3.6	56	0.113
610			50	90	290	900	410	45	25-60	3.9	73	0.087
611			60	50	200	570	265	-	-	4.3	-	-
612			70	45	130	400	185	-	-	-	-	-
613		1000	20	270	910	3400	1380	20	12-33	3.5	36	0.175
614			30	170	570	1900	850	33	26-47	4.0	52	0.121
615			40	100	340	950	450	47	8-66	4.4	67	0.094
616			50	50	200	530	250	-	-	4.8	-	-
617			60	35	130	350	170	-	-	-	-	-
618			70	25	80	220	105	-	-	-	-	-
619		2000	20	160	650	2300	985	16	0-36	6.0	17	0.375
620			30	80	220	520	270	-	-	9.4	-	-
621			40	30	90	220	110	-	-	-	-	-

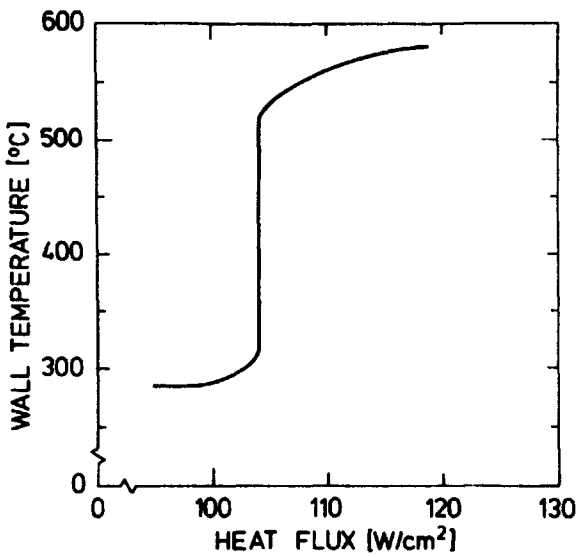

Fig. 1.1. Variation of Wall Temperature with Heat Flux at Burnout. Bennet et al. (1967). Pressure 70 bar. Tube Diameter 12.5 mm. Heated Length 5.56 m. Mass Flux 2560 kg/m^2s. Inlet Subcooling 20°C.

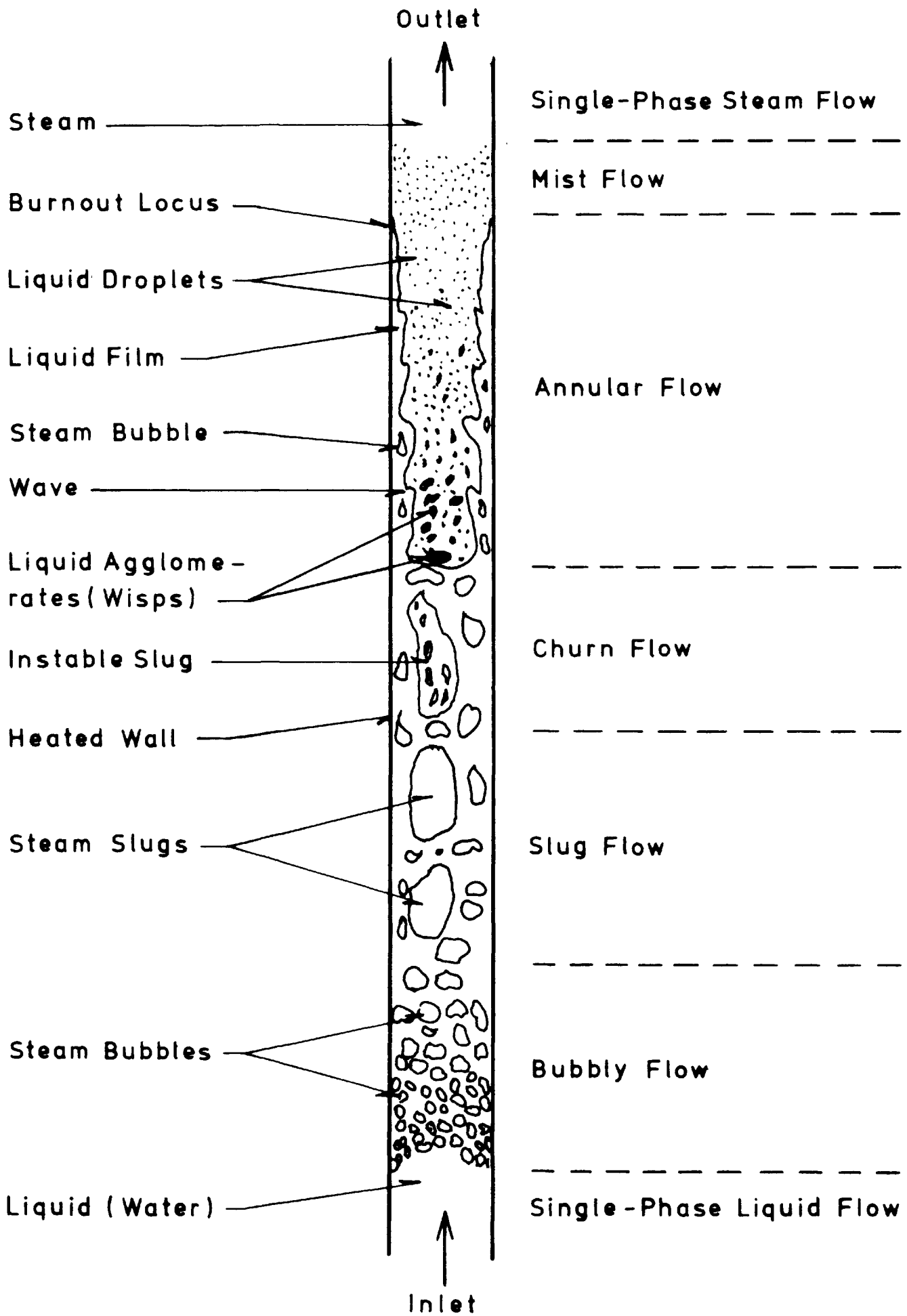

Fig. 2.1. Regimes of Flow in a Boiling Channel
Hewitt and Hall-Taylor (1970).

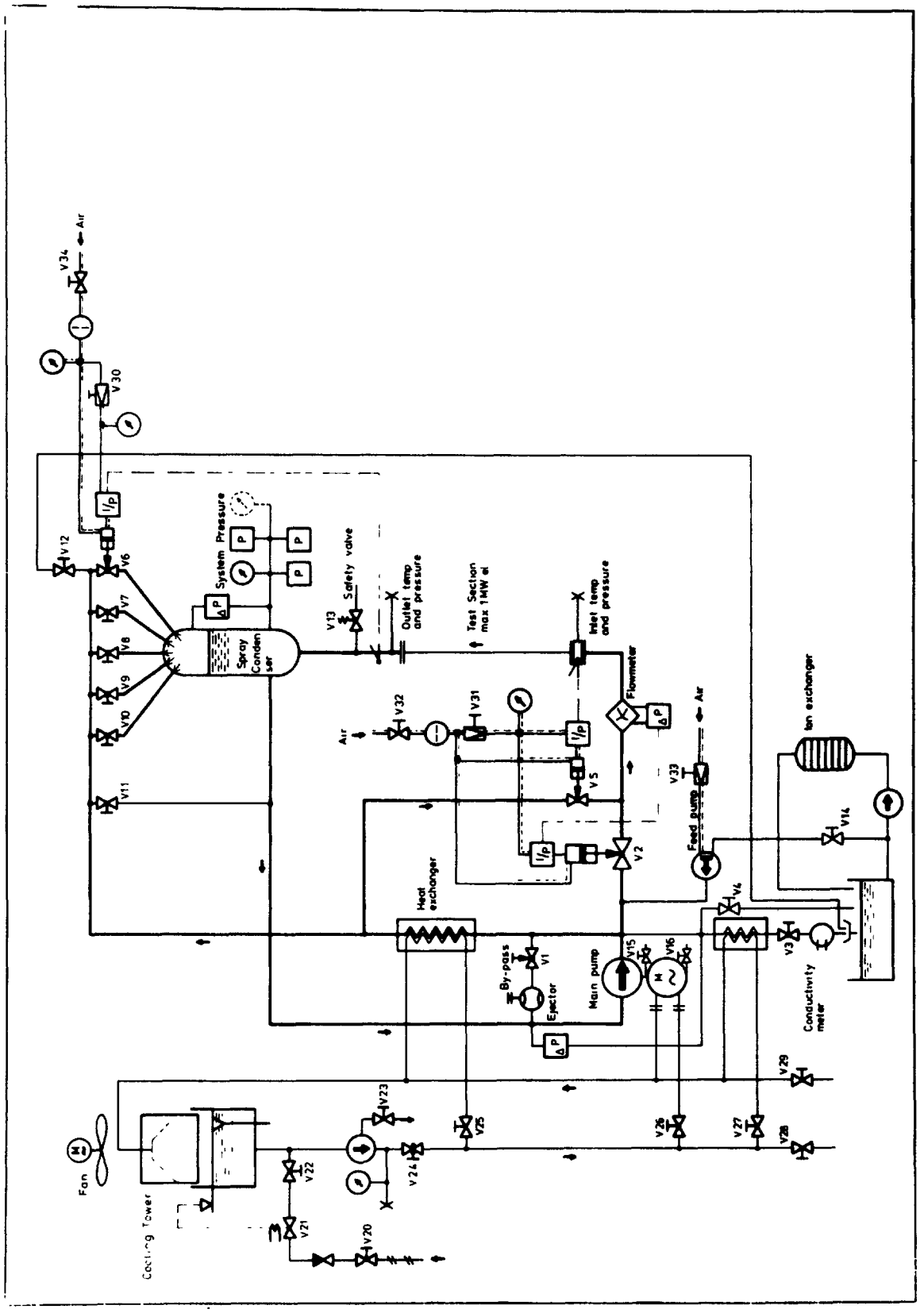

Fig. 3.1. RISØ High Pressure Water Loop.

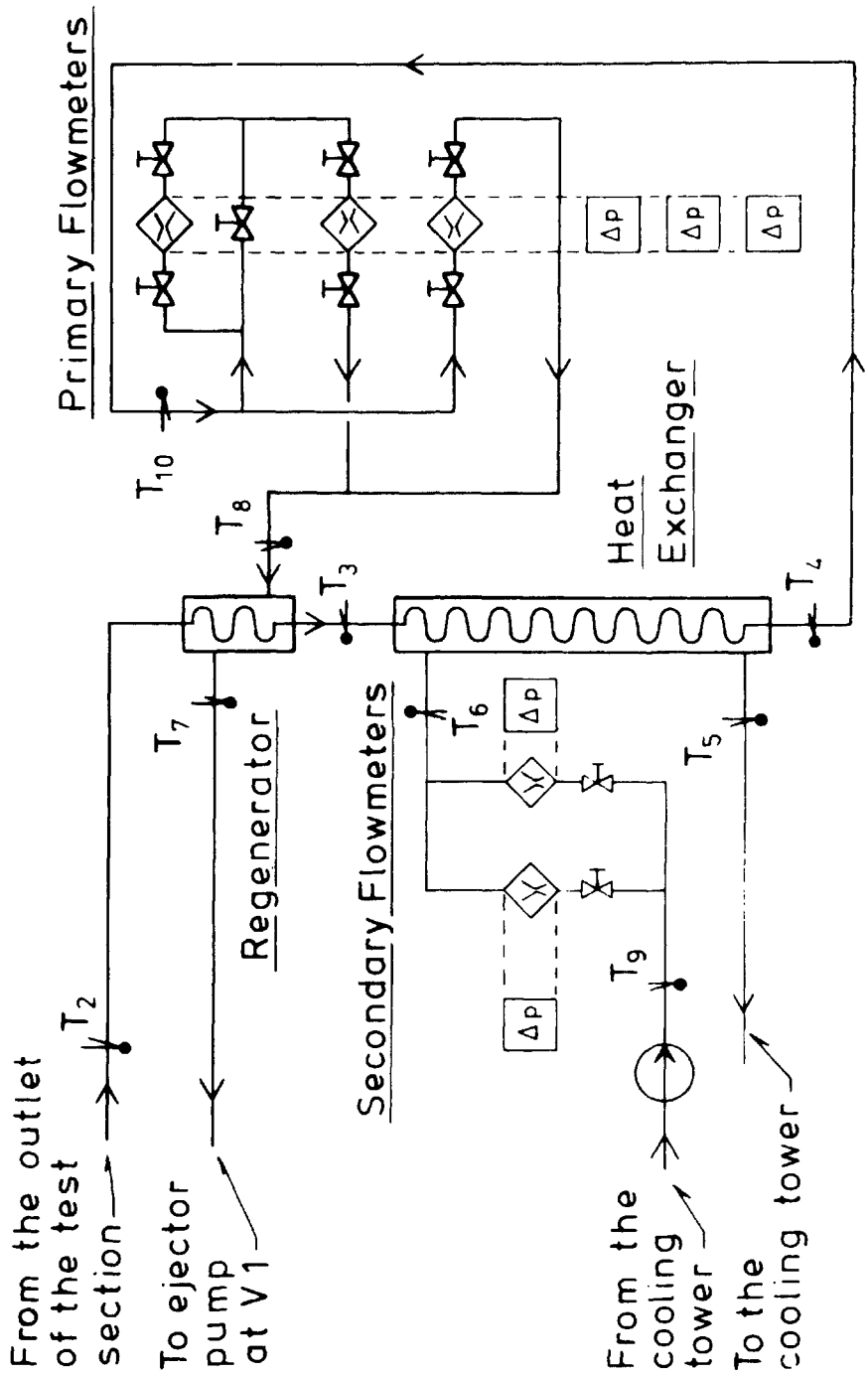

Fig. 3.2. Heat Balance Unit.

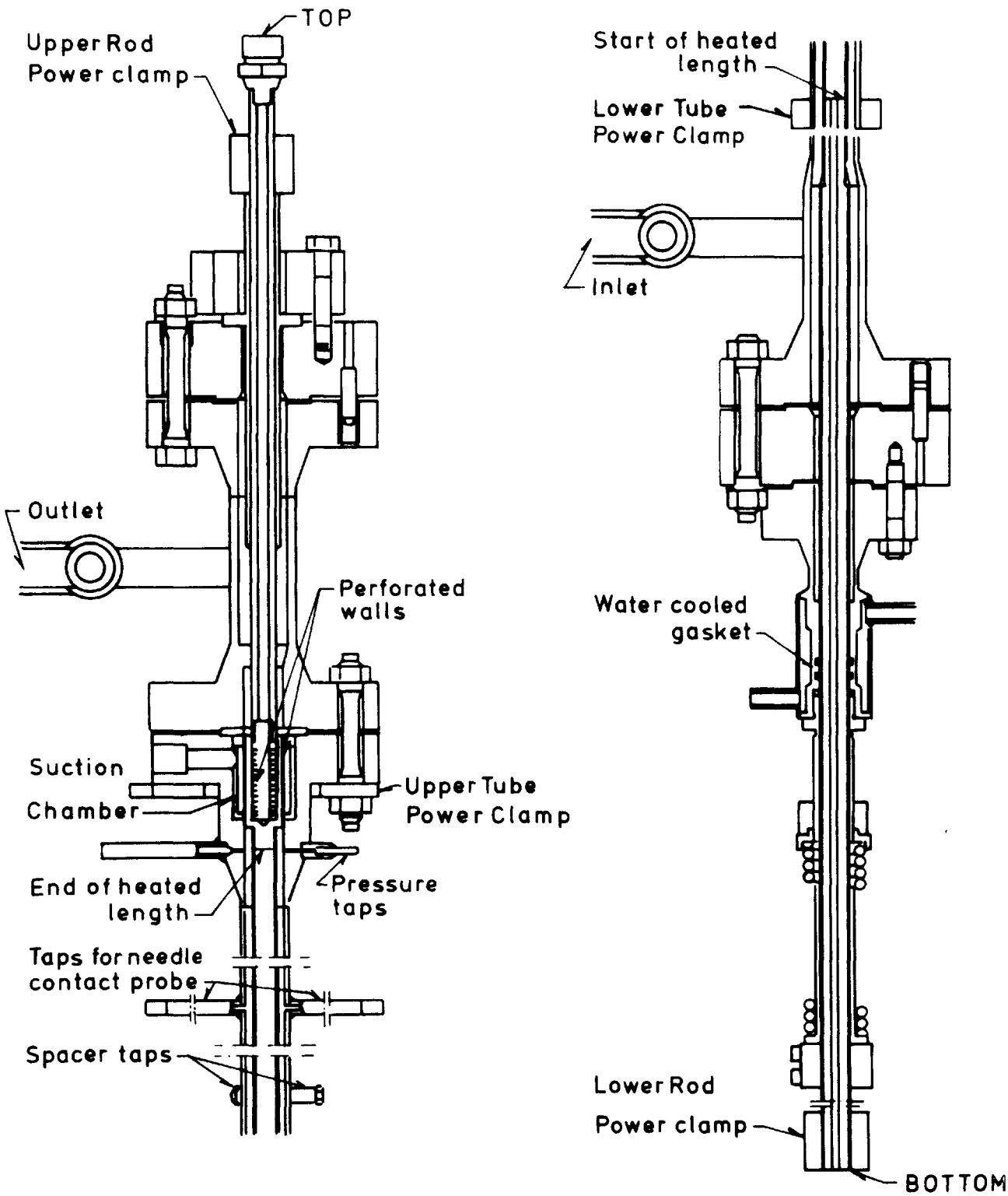

Fig. 3.3. Annular Test Section 17/26S.

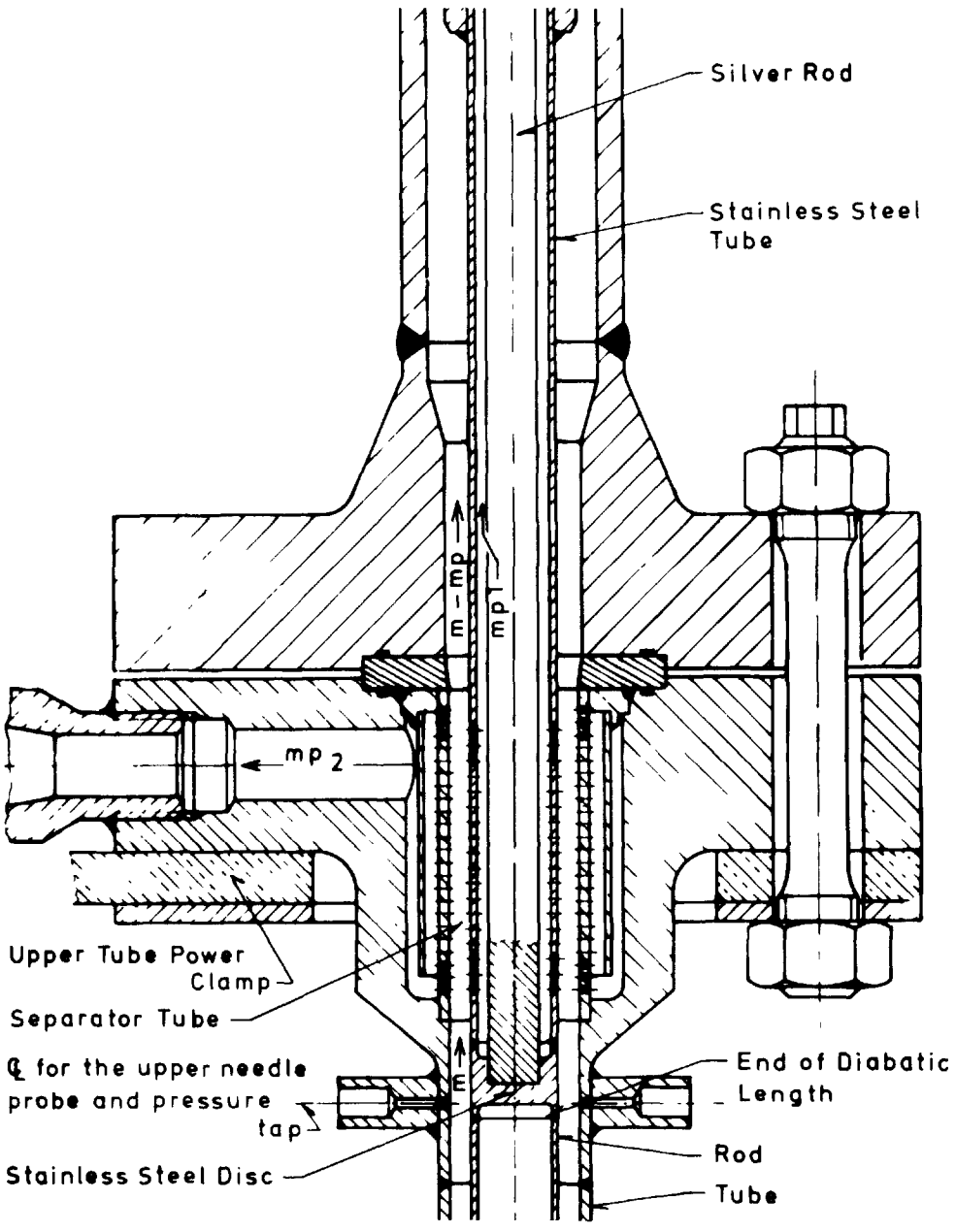

Fig. 3.4.a. Suction Chamber in Annular Test Sections 17/26S and L.

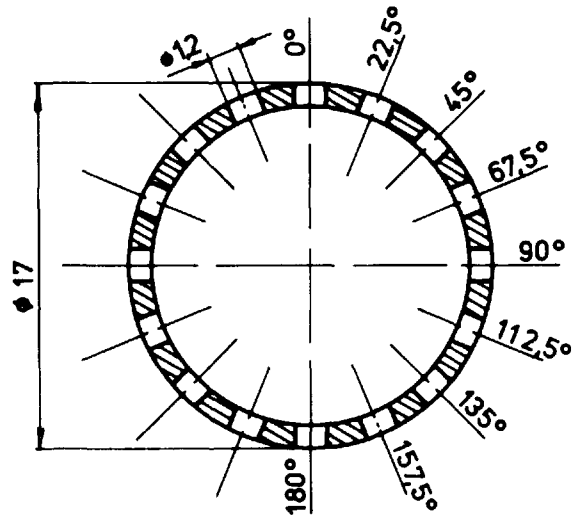

Cross section of filter

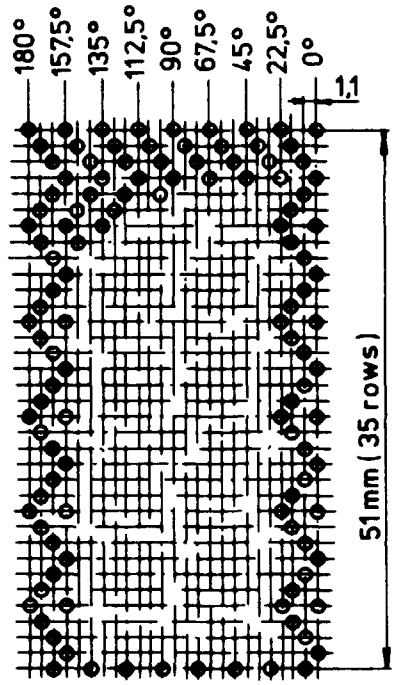

Filter hole pattern

Fig. 3.4.b. Rod Suction Area in Annular Test Sections 17/26S and L.

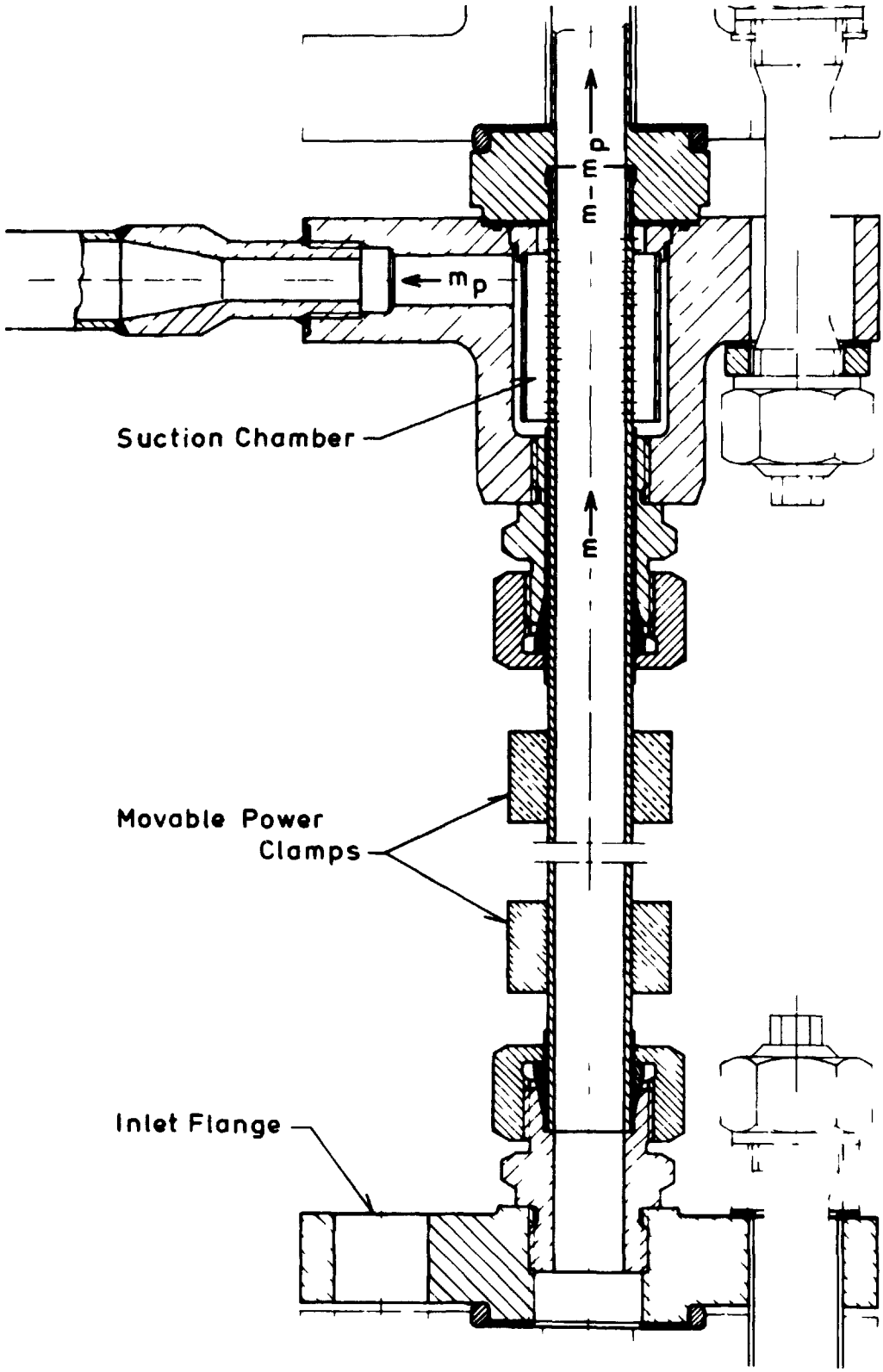

Fig. 3.5. Tubular Test Section 20.

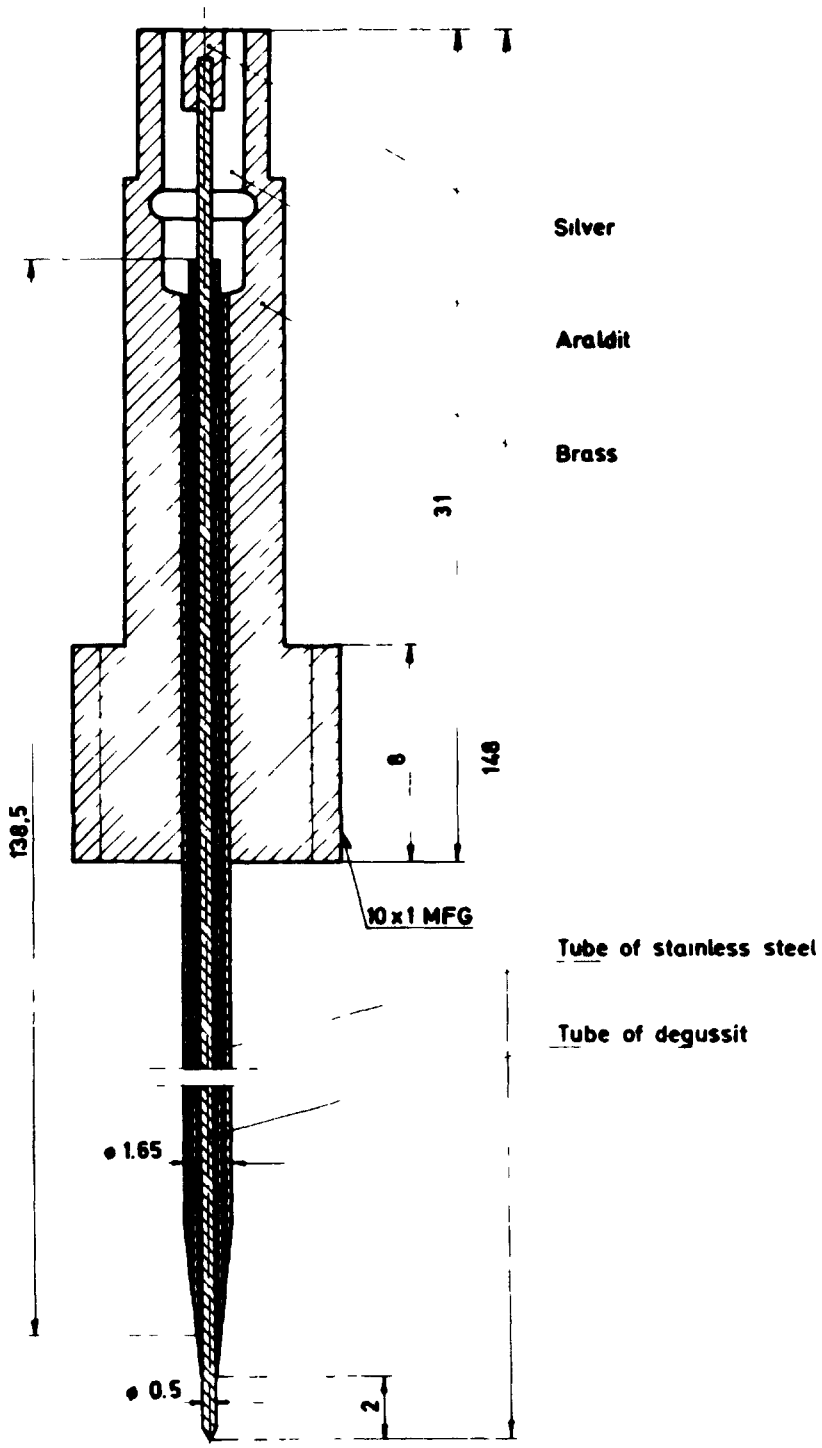

Fig. 3.6. Needle Contact Probe.

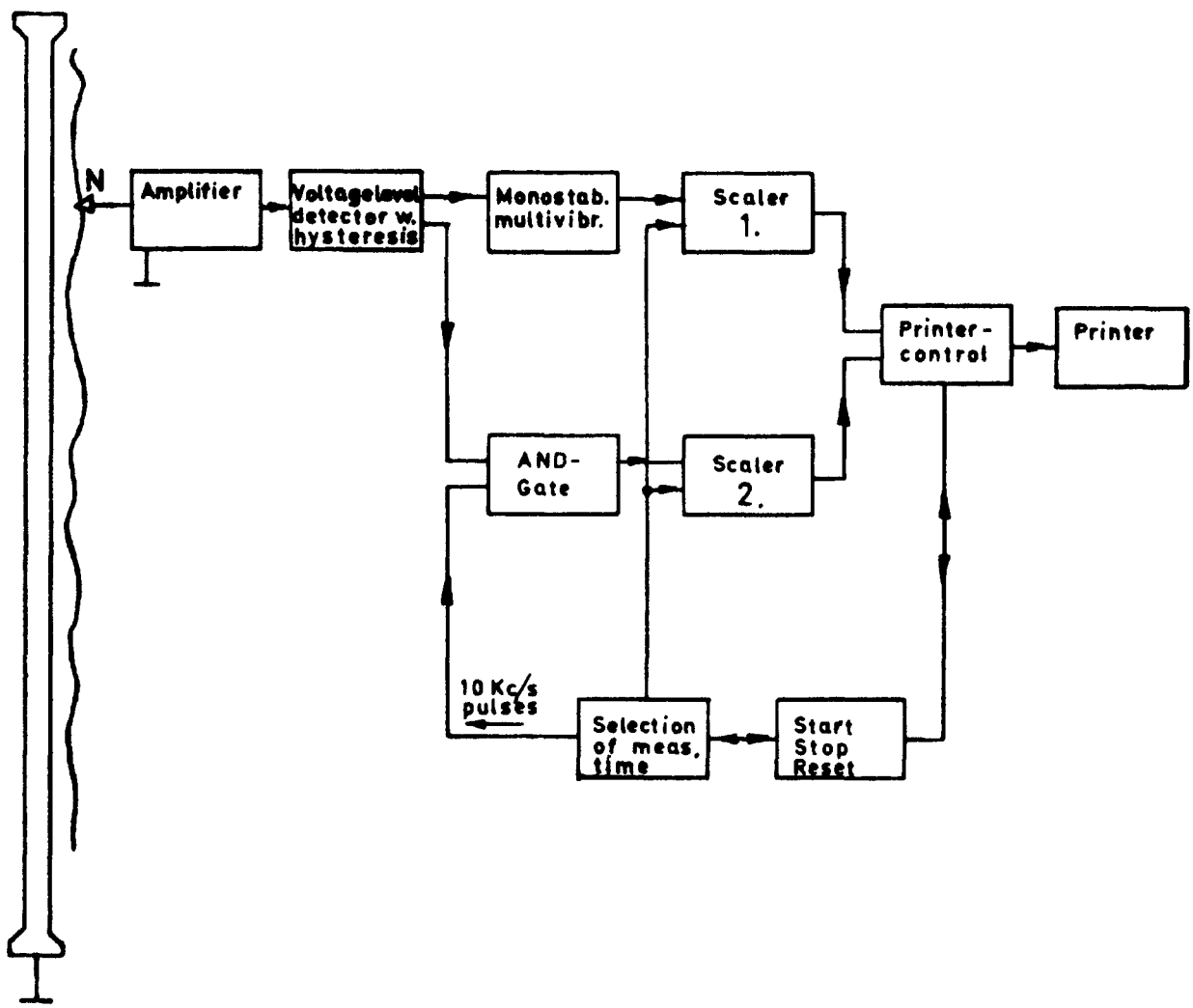

Fig. 3.7. Instrumentation for Film-Thickness Measurements.

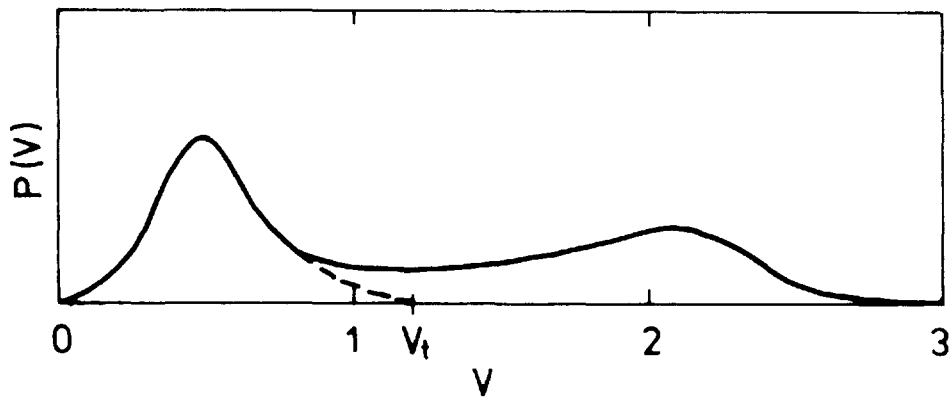

Fig. 3.8. Example of a Probability Density Curve for the Signal from the Needle Contact Probes.

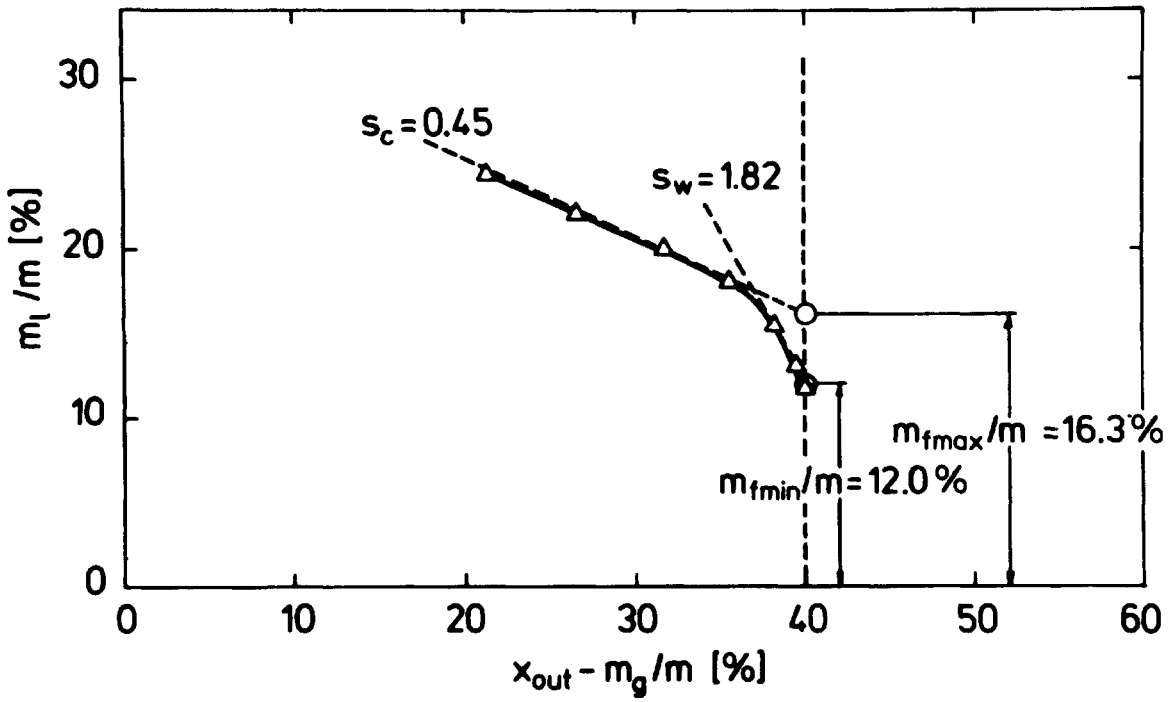

Fig. 3.9. Example of Suction Curve.
Test Section 20. Adiabatic. p = 70 bar. G = 1000 kg/m^{2}s.
x_{out} = 40%.

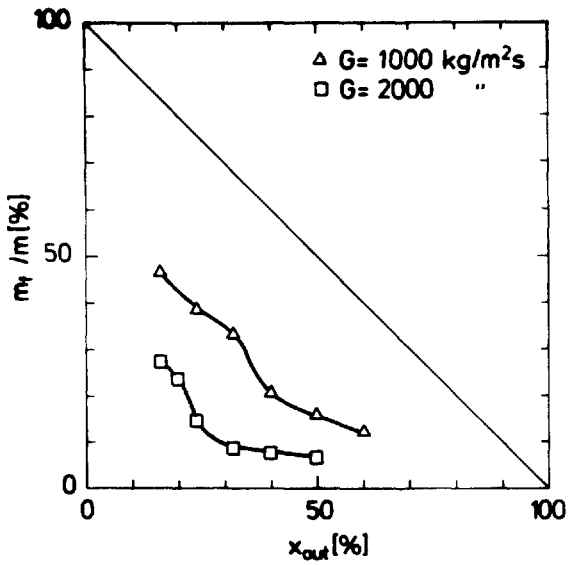

Fig. 3.10.a. Film Flow Measurements.
Test Section 10. Adiabatic. p = 30 bar.

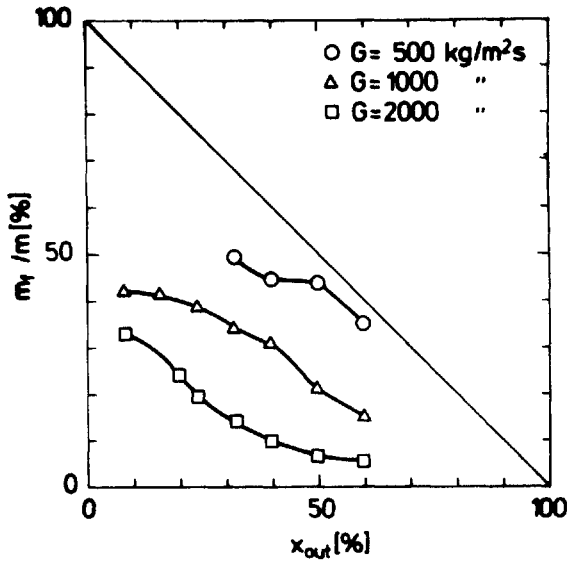

Fig. 3.10.b. Film Flow Measurements.
Test Section 10. Adiabatic. p = 50 bar.

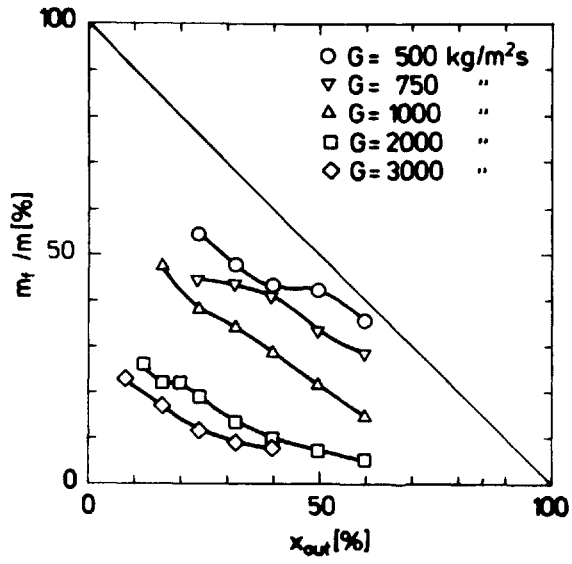

Fig. 3.10.c. Film Flow Measurements.
Test Section 10. Adiabatic. p = 70 bar.

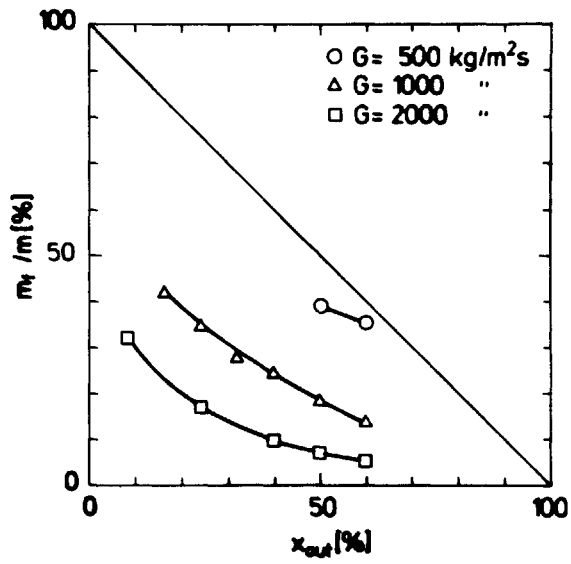

Fig. 3.10.d. Film Flow Measurements.
Test Section 10. Adiabatic. p = 90 bar.

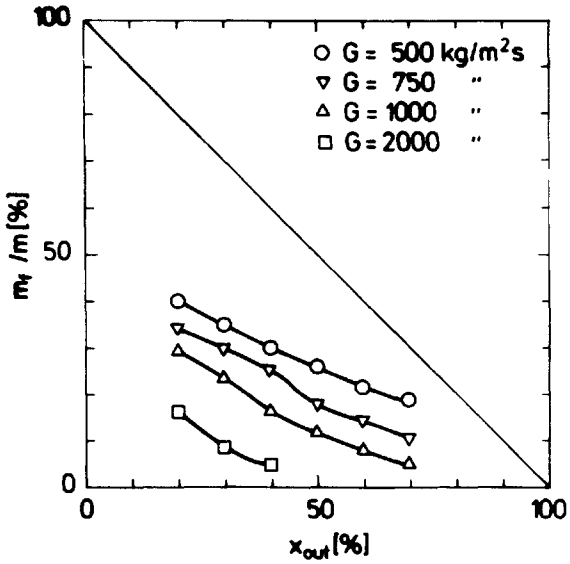

Fig. 3.11. Film Flow Measurements.
Test Section 20. Adiabatic. p = 70 bar.

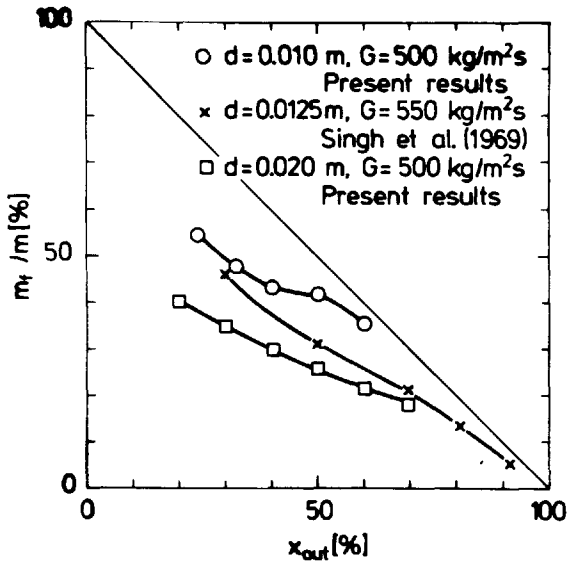

Fig. 3.12.a. Film Flow Measurements.
Comparison with Other Measurements.
G ≈ 500 kg/m²s. p = 70 bar.

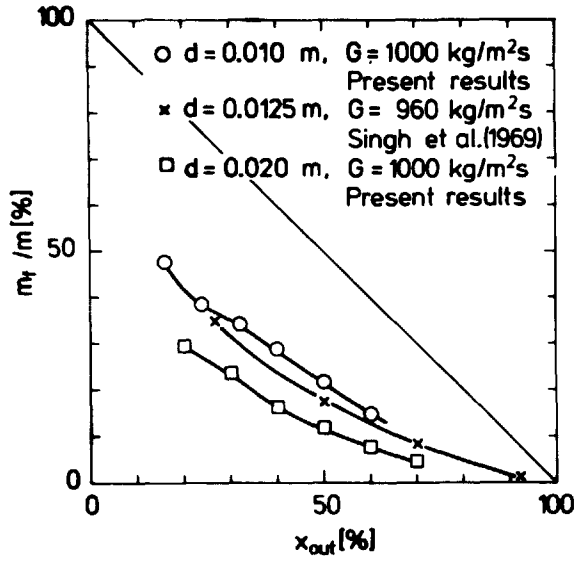

Fig. 3.12.b. Film Flow Measurements.
Comparison with Other Measurements.
G ≈ 1000 kg/m²s. p = 70 bar.

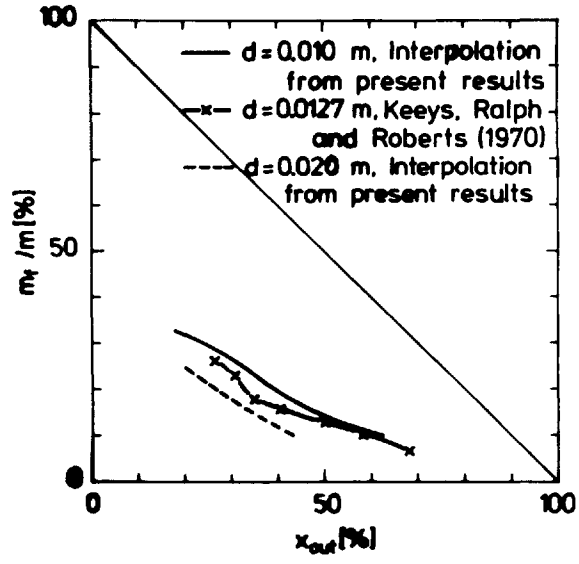

Fig. 3.12.c. Film Flow Measurements.
Comparison with Other Measurements.
G = 1360 kg/m²s. p = 70 bar.

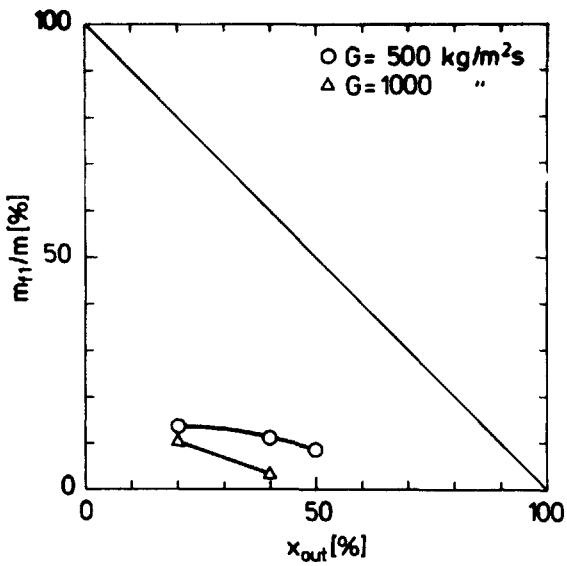

Fig. 3.13.a. Rod Film Flow Measurements.
Test Section 17/26L. Adiabatic. p = 30 bar.

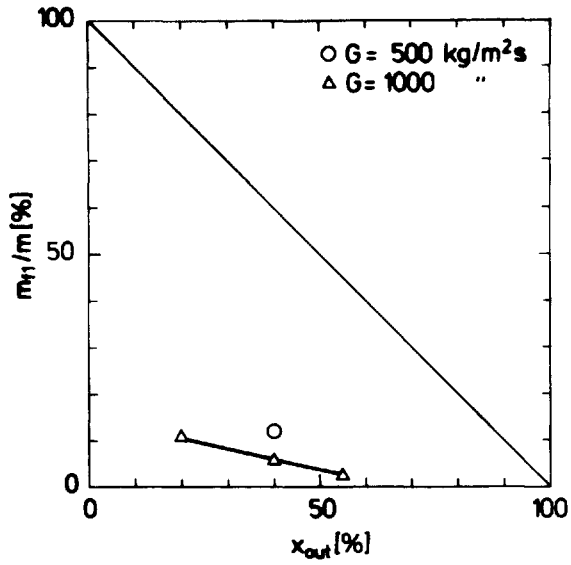

Fig. 3.13.b. Rod Film Flow Measurements.
Test Section 17/26L. Adiabatic. p = 50 bar.

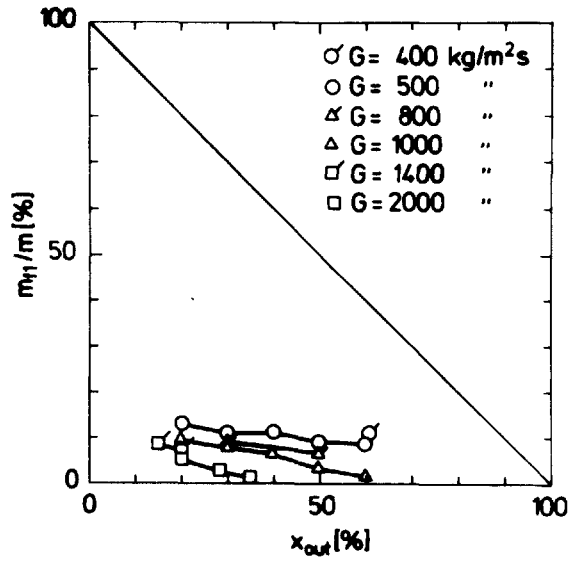

Fig. 3.13.c. Rod Film Flow Measurements.
Test Section 17/26L. Adiabatic. p = 70 bar.

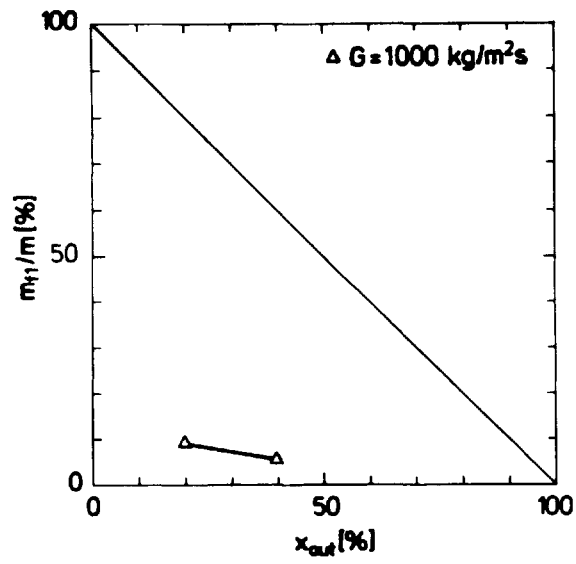

Fig. 3.13.d. Rod Film Flow Measurements.
Test Section 17/26L. Adiabatic. p = 90 bar.

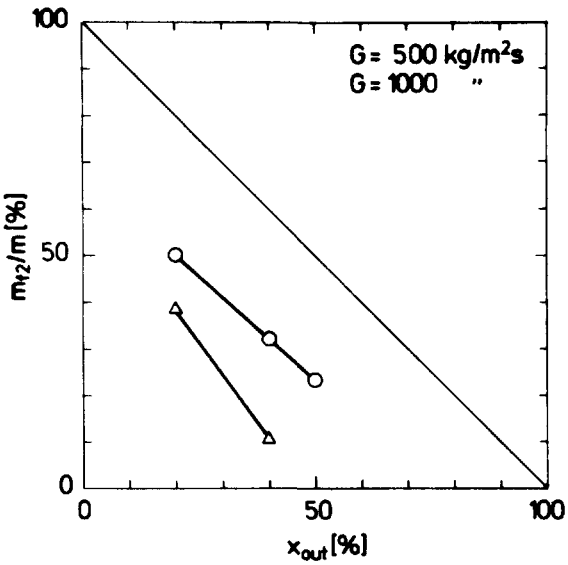

Fig. 3.14.a. Tube Film Flow Measurements. Test Section 17/26L. Adiabatic. p = 30 bar.

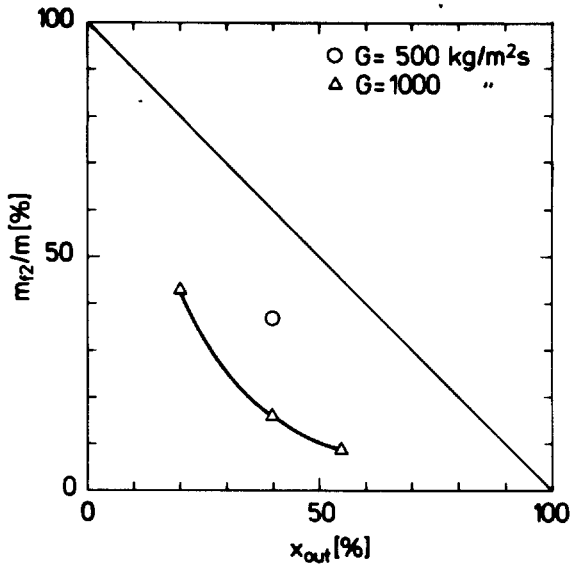

Fig. 3.14.b. Tube Film Flow Measurements. Test Section 17/26L. Adiabatic. p = 50 bar.

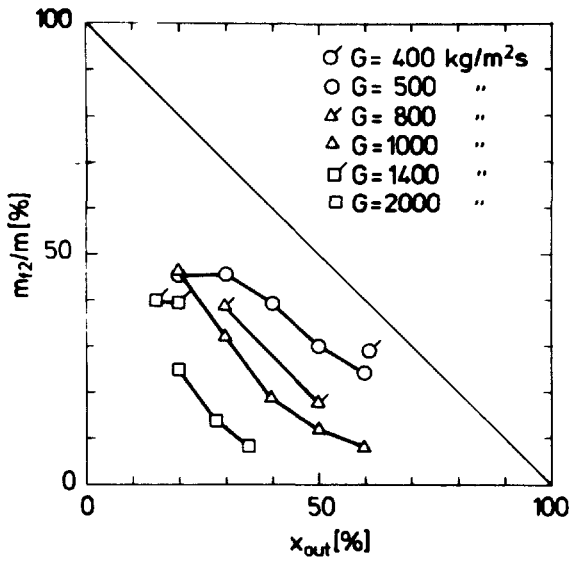

Fig. 3.14.c. Tube Film Flow Measurements. Test Section 17/26L. Adiabatic. p = 70 bar.

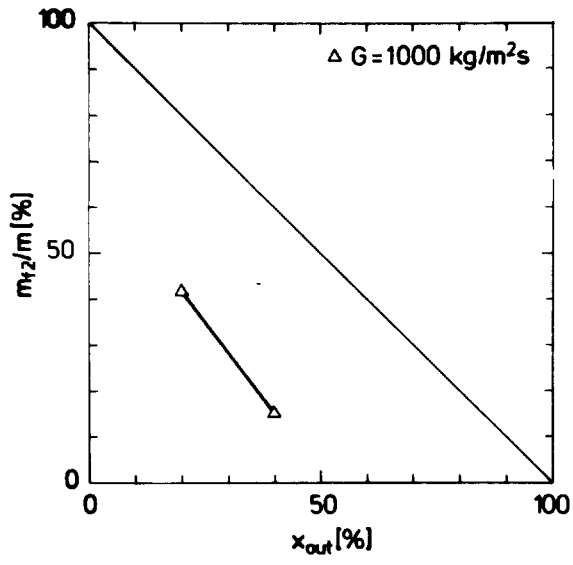

Fig. 3.14.d. Tube Film Flow Measurements. Test Section 17/26L. Adiabatic. p = 90 bar.

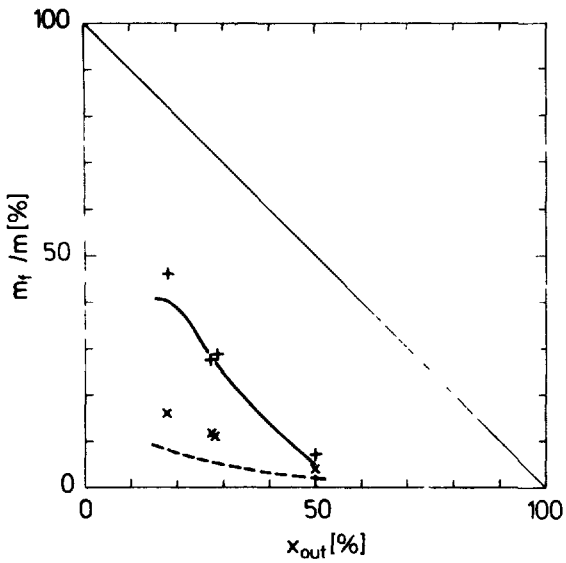

Fig. 3.15. Film Flow Measurements.
Comparison with Other Measurements.
G = 1360 kg/m^{2}s. p = 70 bar.

\+ m_{f1}/m } Moeck (1970). d_1=0.0197m,
× m_{f2}/m } d_2=0.0238m, L_a=2.9m.

--- m_{f1}/m } Interpolations from Present
—— m_{f2}/m } Results. Test Section 17/26L.

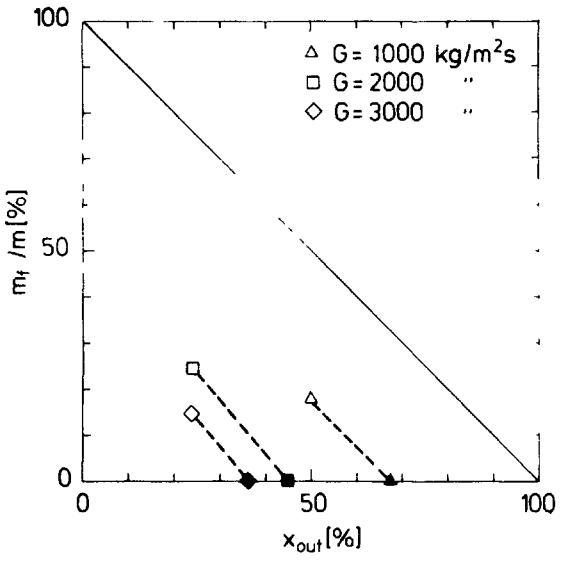

Fig. 3.16.a. Film Flow and Burnout Measurements.
Test Section 10. Diabatic. P = 30 bar.
q" = 100 W/cm^2. L_d = 4.02 m.
The Solid Symbols Designate x_{BO} Derived from Burnout Measurements.
(Cf.eq. (3.18)).

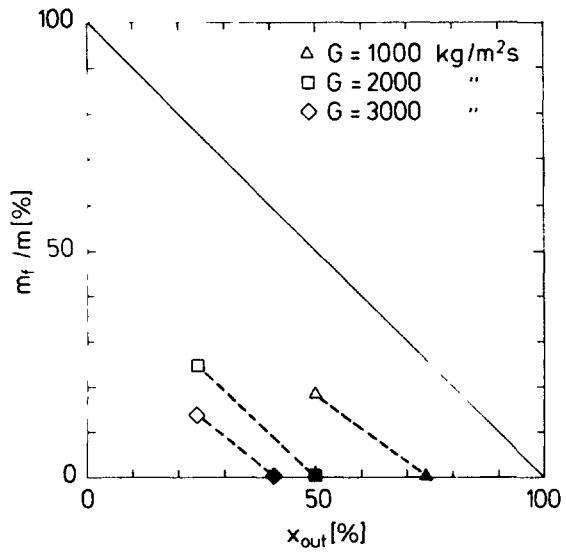

Fig. 3.16.b. Film Flow and Burnout Measurements.
Test Section 10. Diabatic. P = 50 bar.
q" = 100 W/cm^2. L_d = 4.02 m.
The Solid Symbols Designate x_{BO} Derived from Burnout Measurements.
(Cf. eq. (3.18)).

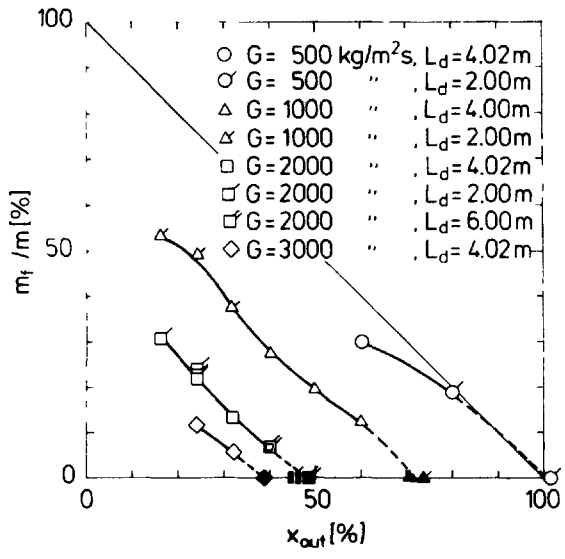

Fig. 3.16.c. Film Flow and Burnout Measurements.
Test Section 10. Diabatic. P = 70 bar.
q" = 100 W/cm^2. L_d = 2.00-6.00 m.
The Solid Symbols Designate x_{BO} Derived from Burnout Measurements.
(Cf. eq. (3.18)).

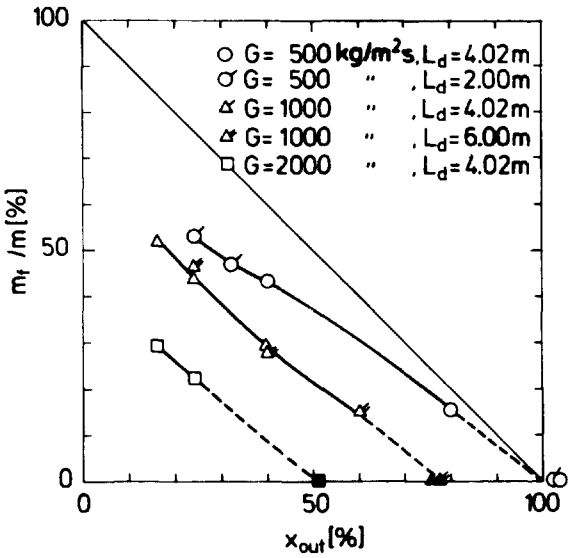

Fig. 3.16.d. Film Flow and Burnout Measurements.
Test Section 10. Diabatic. P = 70 bar
q" = 50 W/cm^2. L_d = 2.00-6.00 m
The Solid Symbols Designate x_{BO}
Derived from Burnout Measurements.
(Cf. eq. (3.18)).

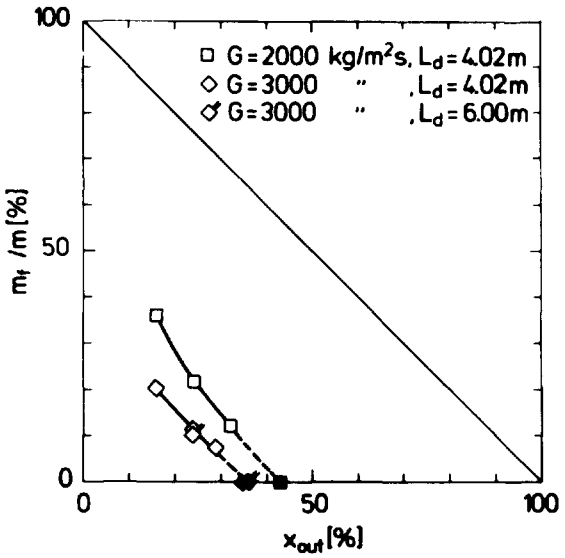

Fig. 3.16.e. Film Flow and Burnout Measurements.
Test Section 10. Diabatic. P = 70 bar.
q" = 150 W/cm^2. L_d = 4.02-6.00 m.
The Solid Symbols Designate x_{BO}
Derived from Burnout Measurements.
(Cf. eq. (3.18)).

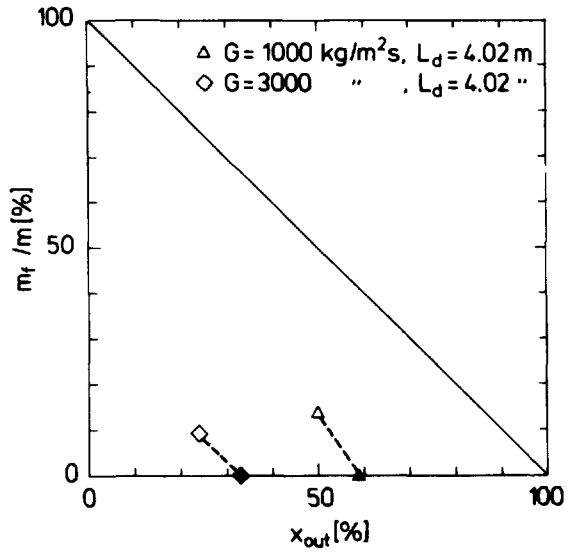

Fig. 3.16.f. Film Flow and Burnout Measurements.
Test Section 10. Diabatic. P = 90 bar.
q" = 100 W/cm^2. L_d = 4.02 m.
The Solid Symbols Designate x_{BO}
Derived from Burnout Measurements.
(Cf. eq. (3.18)).

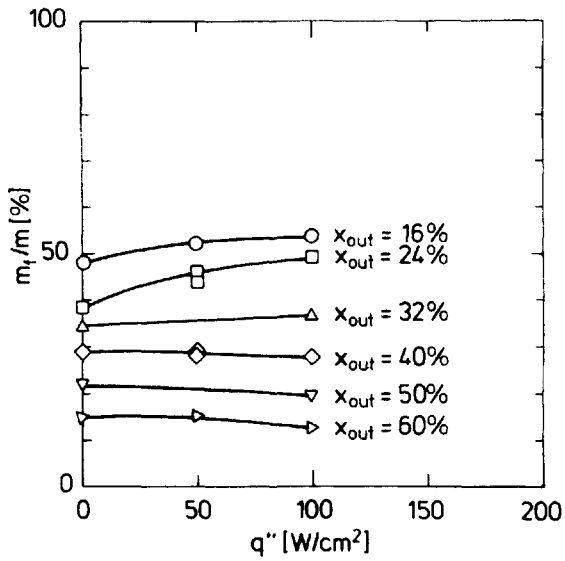

Fig. 3.17.a. Film Flow Measurements. Influence of Heat Flux and Boiling Length. Test Section 10. Adiabatic and Diabatic. P = 70 bar. G = 1000 kg/m^{2}s.

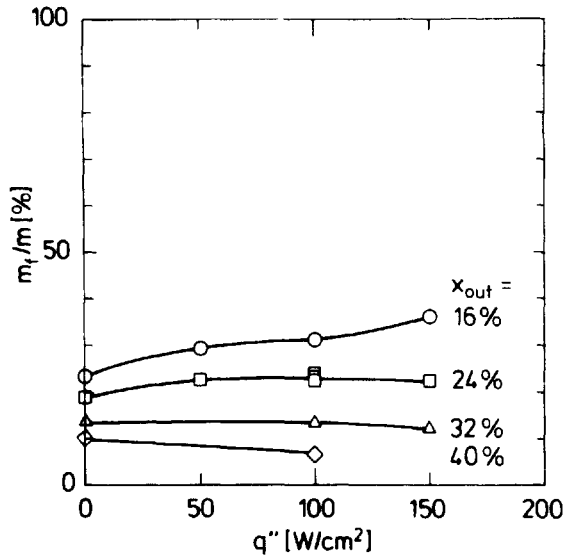

Fig. 3.17.b. Film Flow Measurements. Influence of Heat Flux and Boiling Length. Test Section 10. Adiabatic and Diabatic. P = 70 bar. G = 2000 kg/m^{2}s.

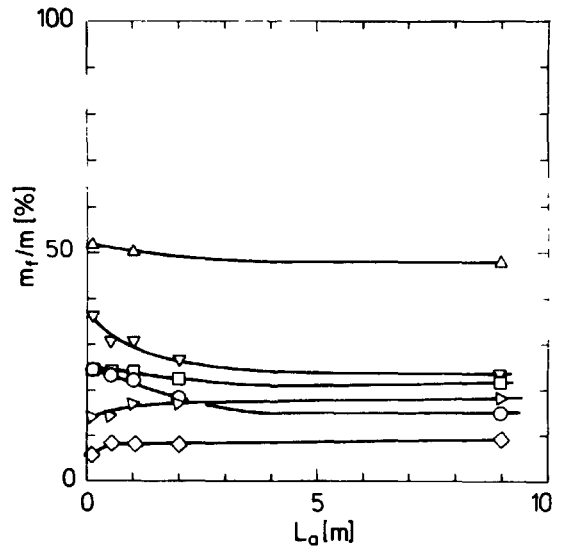

Fig. 3.18. Film Flow Measurements. Influence of Adiabatic Length L_a. Test Section 10.

o p=30,G=2000,q"=100,x_{out}=24

□ p=50,G=2000,q"=100,x_{out}=24

Δ p=70,G=1000,q"= 50,x_{out}=16

▽ p=70,G=2000,q"=150,x_{out}=16

◇ p=70,G=3000,q"=100,x_{out}=32

▷ p=90bar,G=1000kg/m^{2}s,q"=100W/cm^2, x_{out}= 50%.

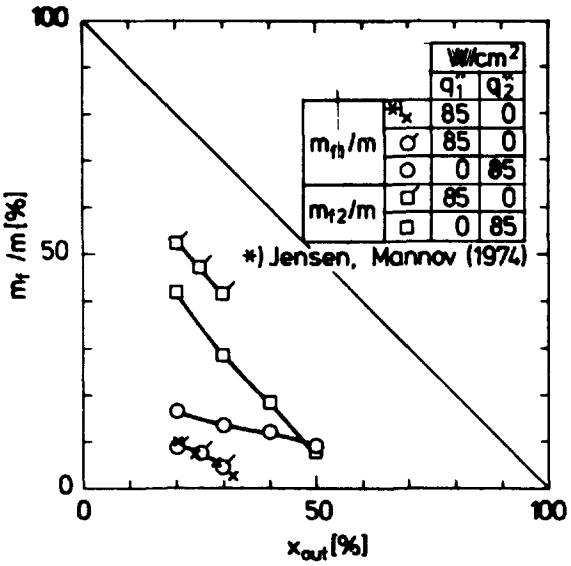

Fig. 3.19.a. Film Flow Measurements. Test Section 17/26S. Diabatic. p = 70 bar. G = 900 kg/m²s.

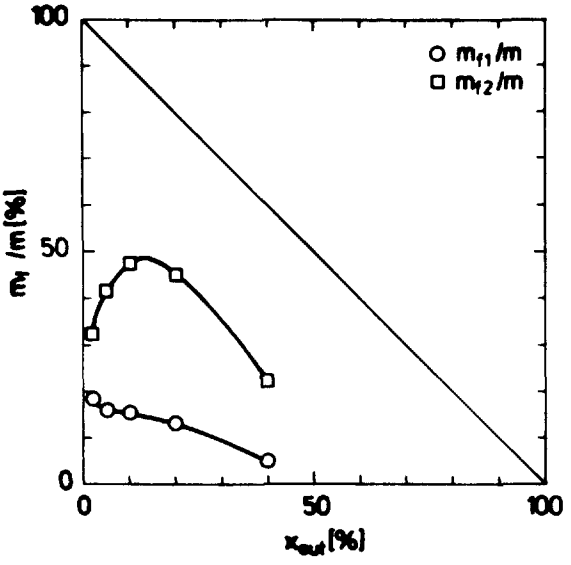

Fig. 3.19.b. Film Flow Measurements. Test Section 17/26S. Diabatic. p = 70 bar. G = 1000 kg/m²s. $q'' = q''_2 = 45$ W/cm².

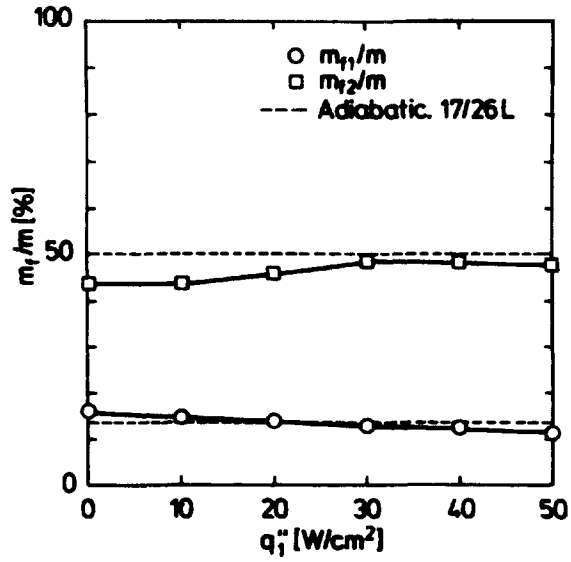

Fig. 3.20.a. Film Flow Measurements. Influence of Relative Heat Flux Distribution and Boiling Length. Test Sections 17/26S and L. Diabatic and Adiabatic. P = 70 bar. G = 500 kg/m²s. $q_1''+q_2''$ = 50 W/cm². x_{out} = 20%.

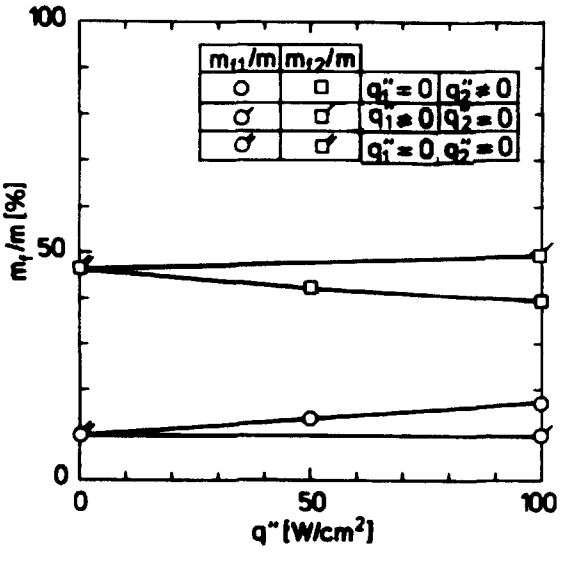

Fig. 3.20.b. Film Flow Measurements. Influence of Relative Heat Flux Distribution and Boiling Length. Test Sections 17/26S and L. Diabatic and Adiabatic. P = 70 bar. G = 1000 kg/m²s. x_{out} = 20%.

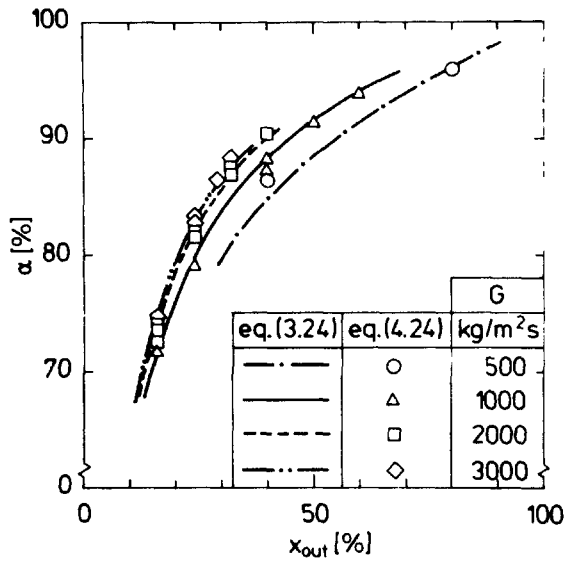

Fig. 3.21.a. Comparison between Mean Void Fractions Calculated from Eq. (3.24) and Eq. (4.24).
Test Section 10. Diabatic. p = 70 bar.

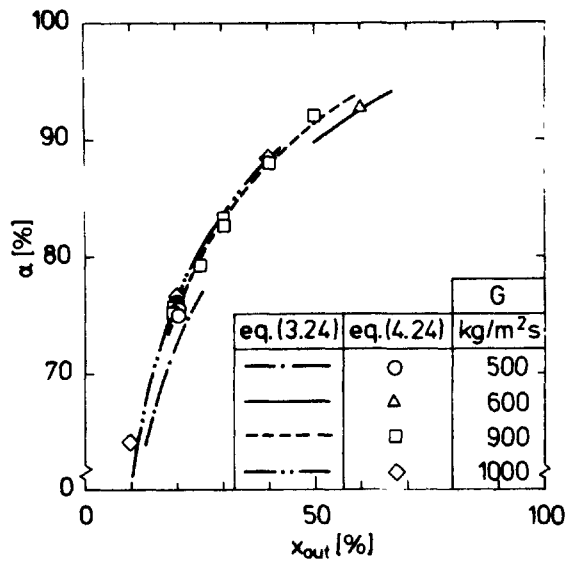

Fig. 3.21.b. Comparison between Mean Void Fractions Calculated from Eq. (3.24) and Eq. (4.24).
Test Section 17/26S. Diabatic. p = 70 bar.

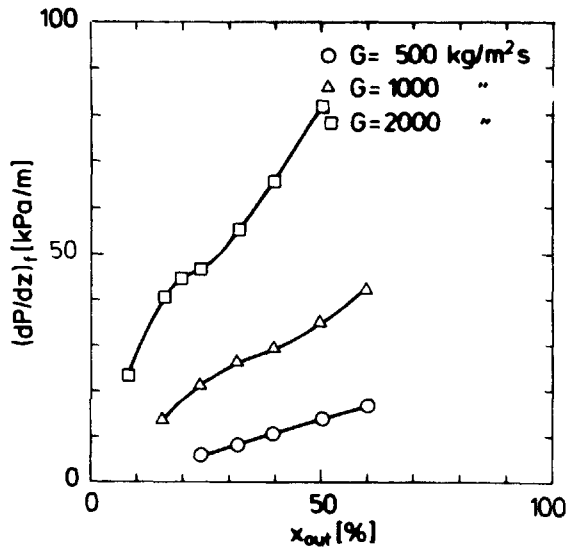

Fig. 3.22.a. Pressure Drop Measurements.
Test Section 10. Adiabatic. p = 30 bar.

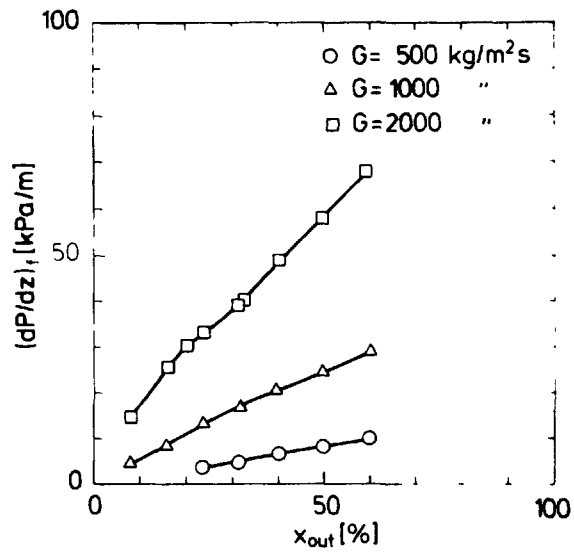

Fig. 3.22.b. Pressure Drop Measurements.
Test Section 10. Adiabatic. p = 50 bar.

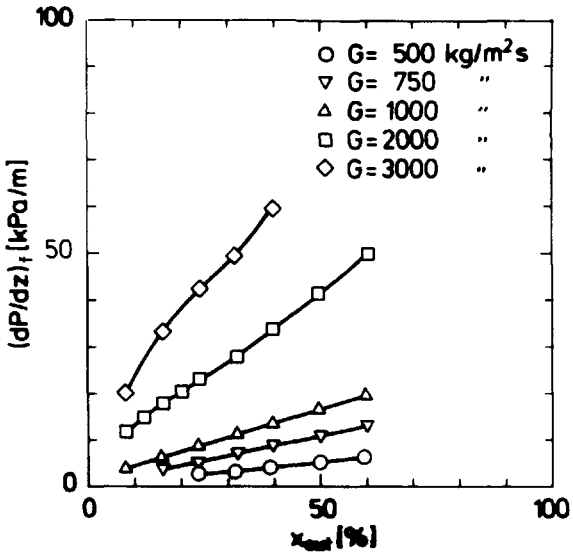

Fig. 3.22.c. Pressure Drop Measurements. Test Section 10. Adiabatic. p = 70 bar.

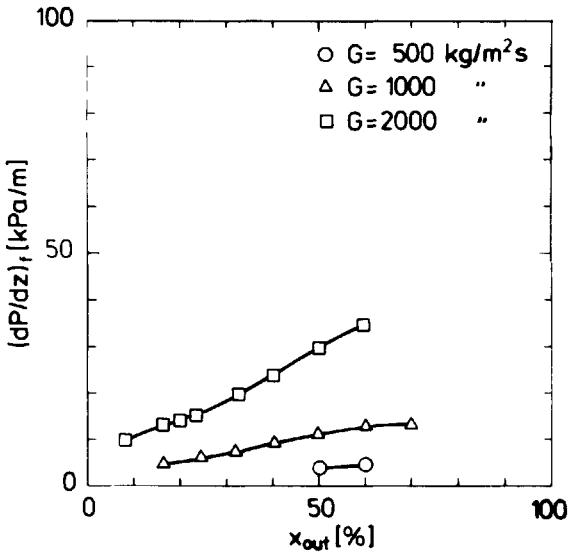

Fig. 3.22.d. Pressure Drop Measurements. Test Section 10. Adiabatic. p = 90 bar.

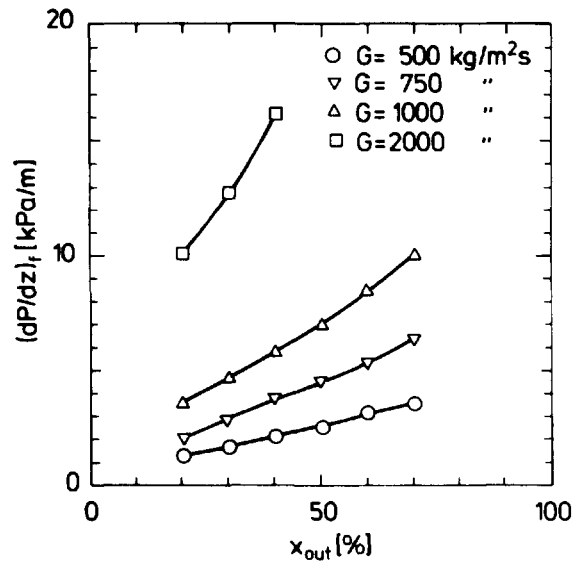

Fig. 3.23. Pressure Drop Measurements. Test Section 20. Adiabatic. p = 70 bar.

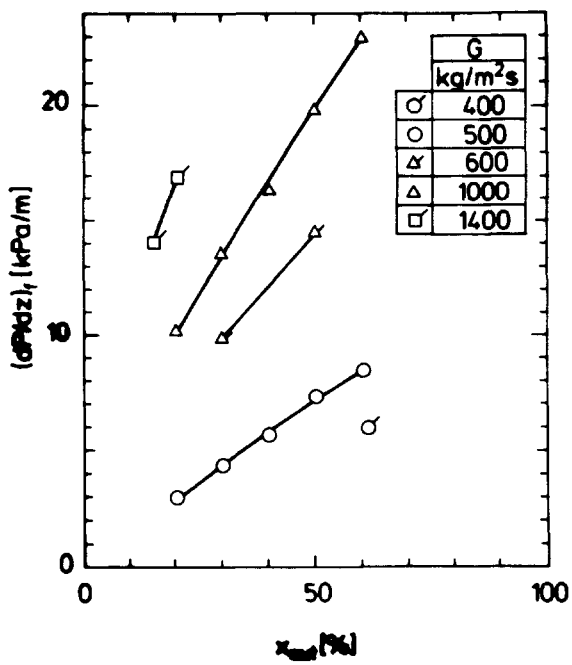

Fig. 3.24. Pressure Drop Measurements. Test Section 17/26L. Adiabatic. p = 70 bar.

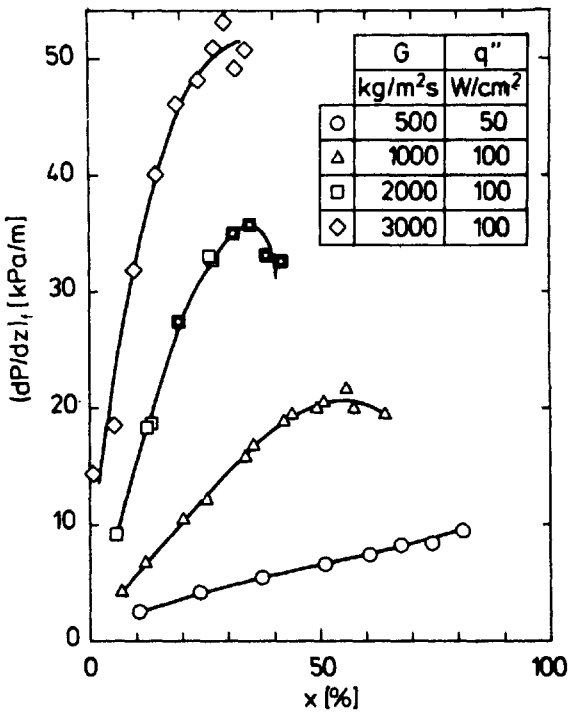

Fig. 3.25. Pressure Drop Measurements.
Test Section 10. Diabatic. p = 70 bar.

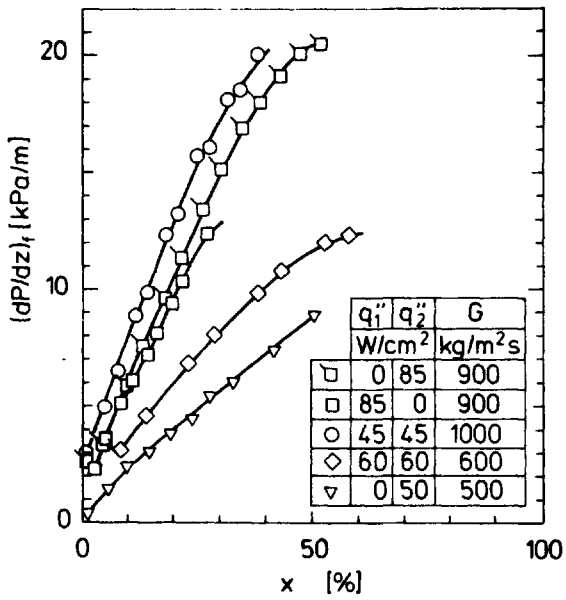

Fig. 3.26. Pressure Drop Measurements.
Test Section 17/26S. Diabatic. p = 70 bar.

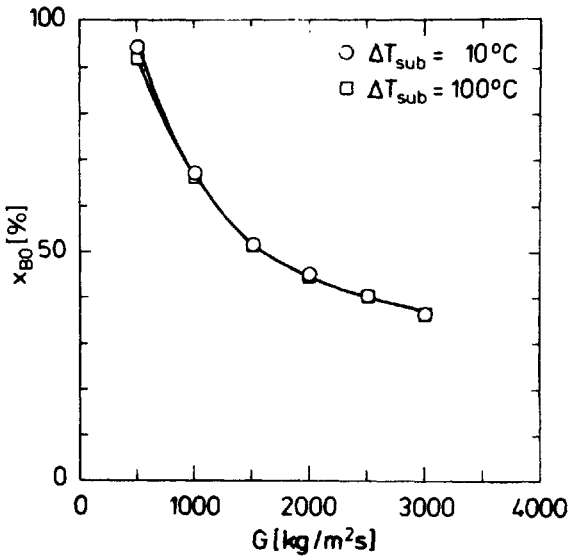

Fig. 3.27.a. Burnout Measurements.
Influence of Inlet Subcooling.
Test Section 10. Diabatic.
P = 30 bar. L_d = 4.02 m.

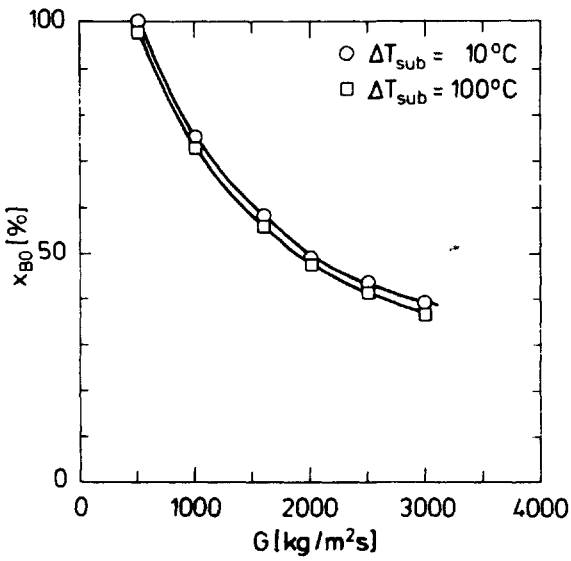

Fig. 3.27.b. Burnout Measurements.
Influence of Inlet Subcooling.
Test Section 10. Diabatic. P = 50 bar.
L_d = 4.02 m.

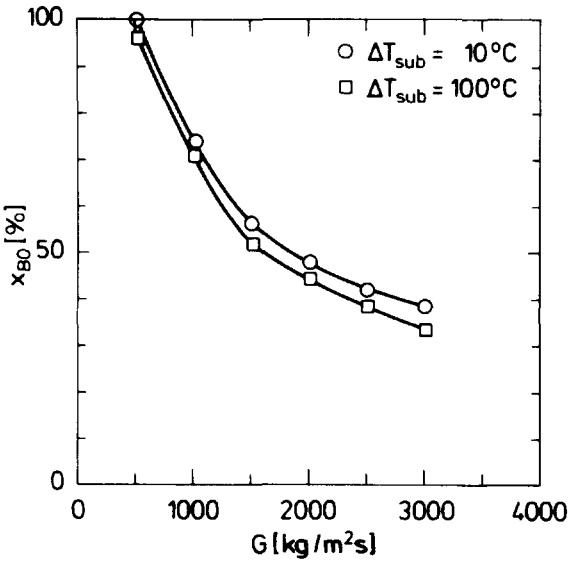

Fig. 3.27.c. Burnout Measurements.
Influence of Inlet Subcooling.
Test Section 10. Diabatic. P = 70 bar.
L_d = 4.02 m.

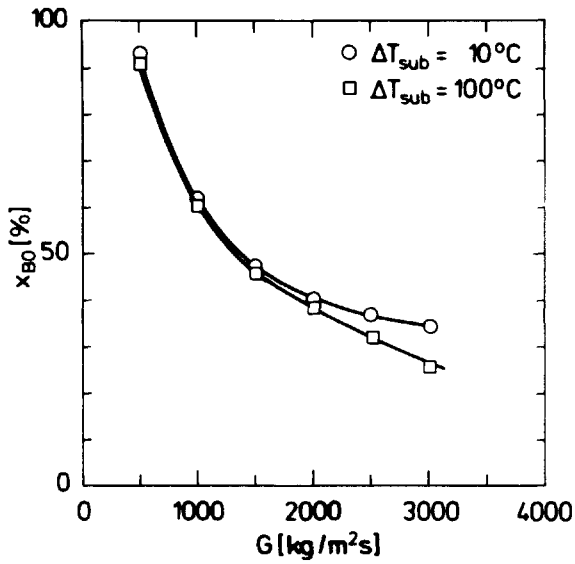

Fig. 3.27.d. Burnout Measurements.
Influence of Inlet Subcooling.
Test Section 10. Diabatic. P = 90 bar.
L_d = 4.02 m.

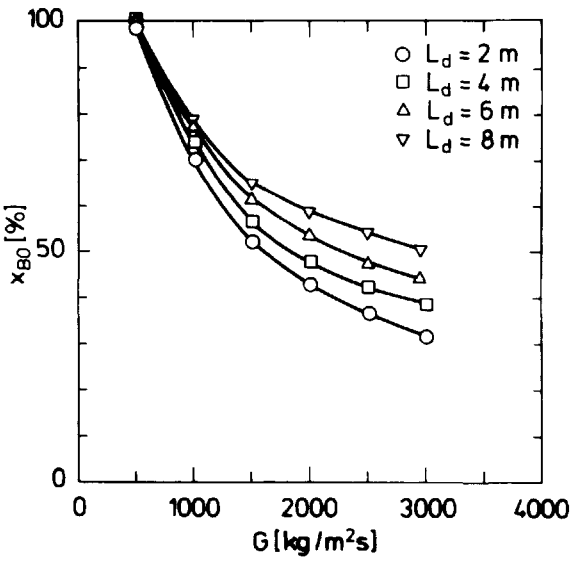

Fig. 3.28. Burnout Measurements.
Influence of Diabatic Length.
Test Section 10. p = 70 bar. ΔT_{sub} = 10°C.

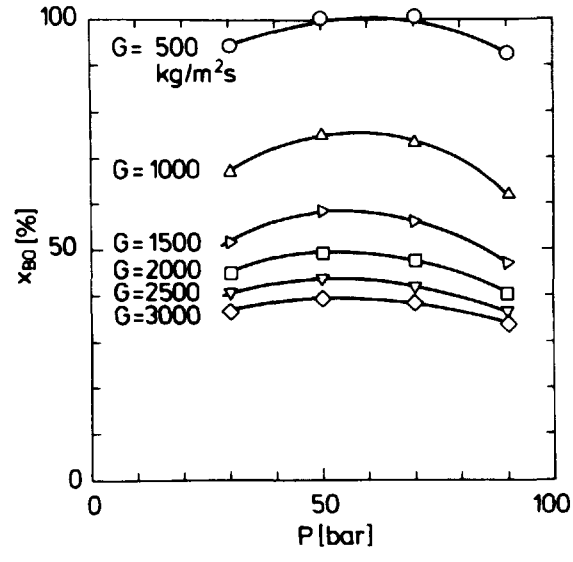

Fig. 3.29. Burnout Measurements.
Influence of System Pressure.
Test Section 10. L_d = 4.02 m. ΔT_{sub} = 10°C.

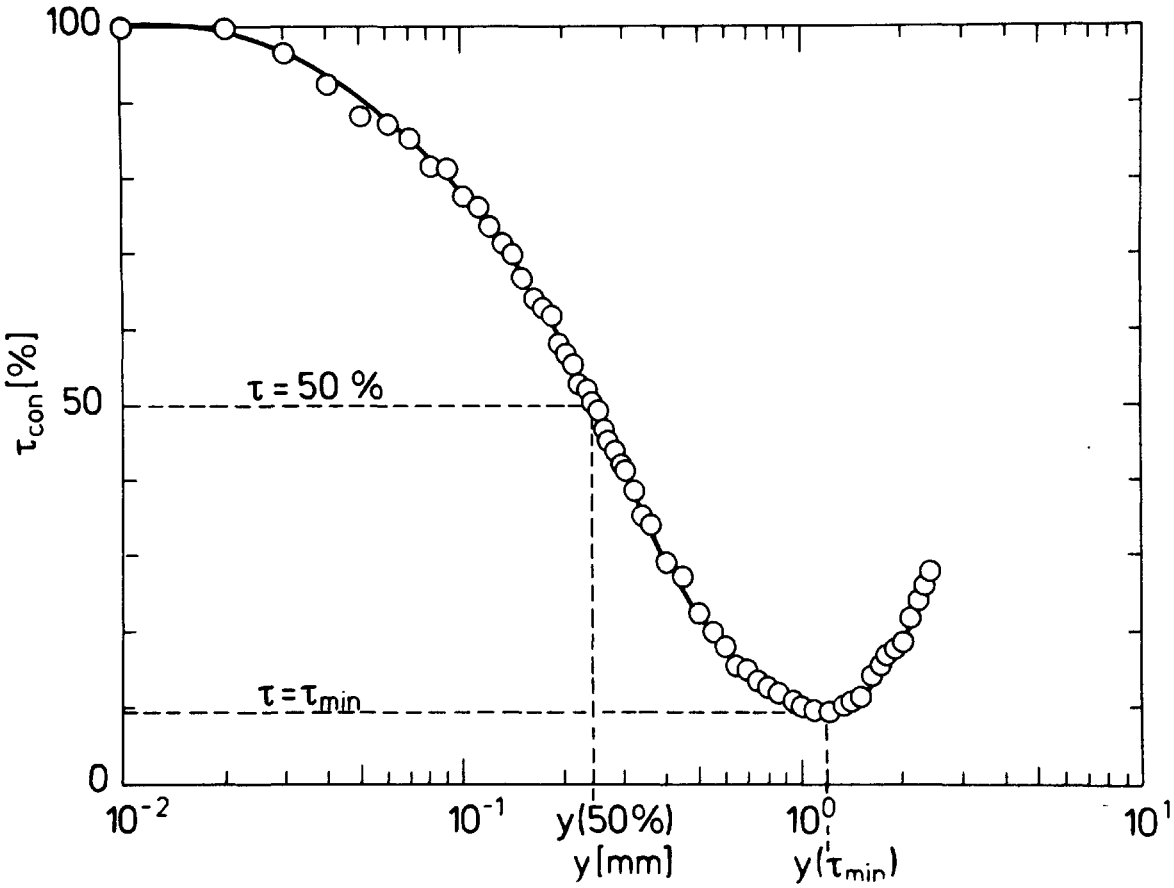

Fig. 3.30. Example of Needle Contact Time Curve.
Test Section 17/26L. Adiabatic. p = 70 bar. G = 1000 kg/m^{2}s.
x_{out} = 20 %.

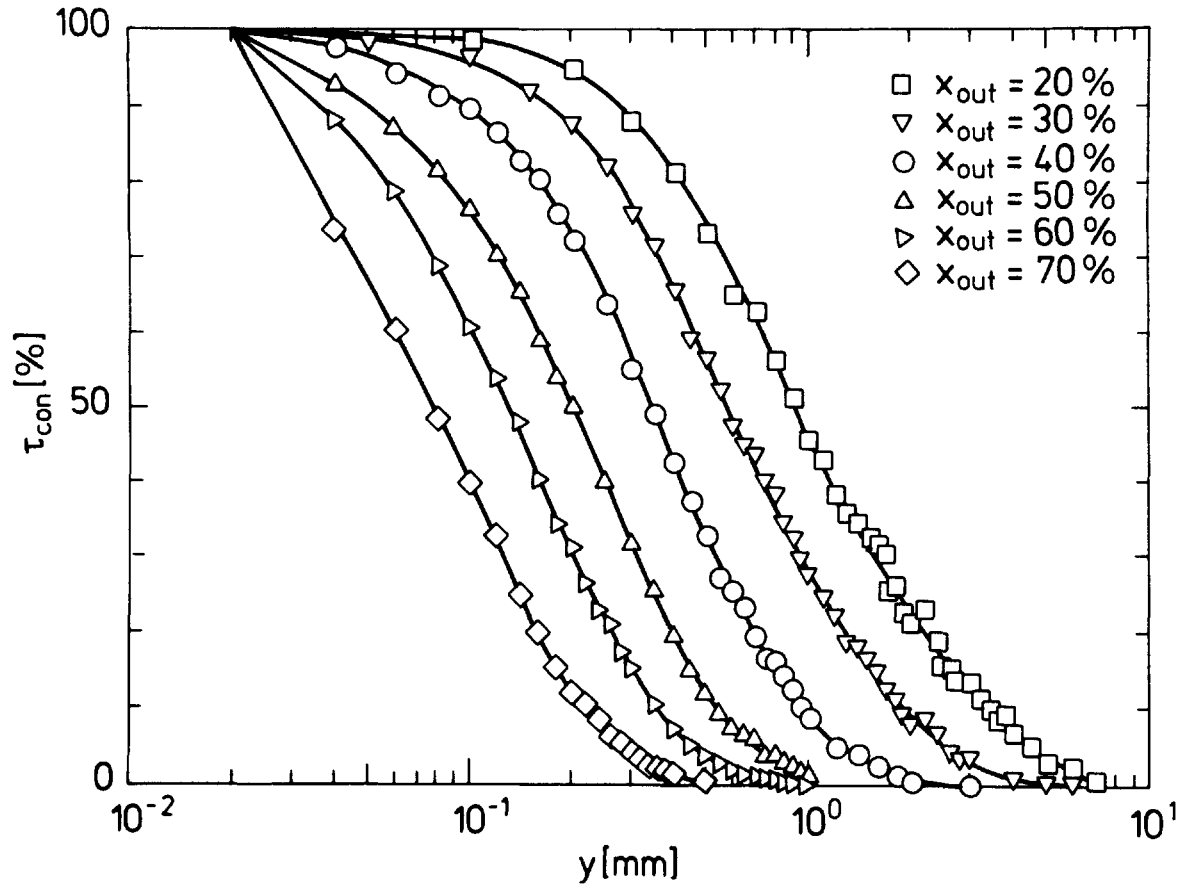

Fig. 3.31. Examples of Needle Contact Time Curves.
Test Section 10. Adiabatic. p = 70 bar. G = 1000 kg/m^{2}s.

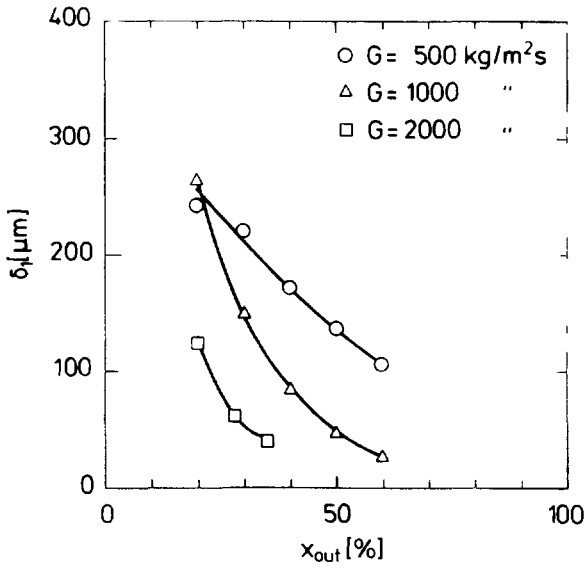

Fig. 3.32. Rod Film Thickness Measurements. Test Section 17/26L. Adiabatic. p = 70 bar.

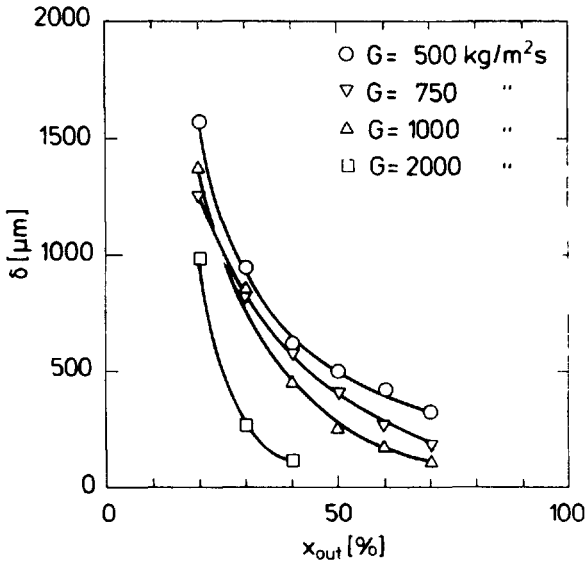

Fig. 3.33. Film Thickness Measurements. Test Section 20. Adiabatic. p = 70 bar.

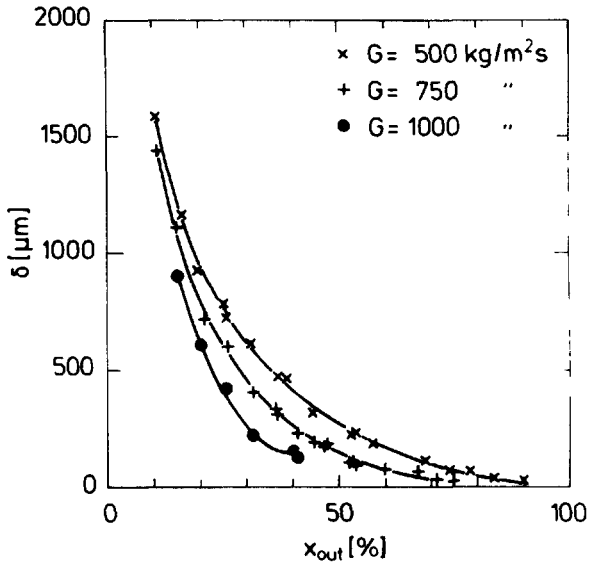

Fig. 3.34. Film Thickness Measurements. Kirillov et al. (1973). Tubular Test Section. r_2 = 0.0085 m. L_a = 4.68 m. Adiabatic. p = 68.6 bar.

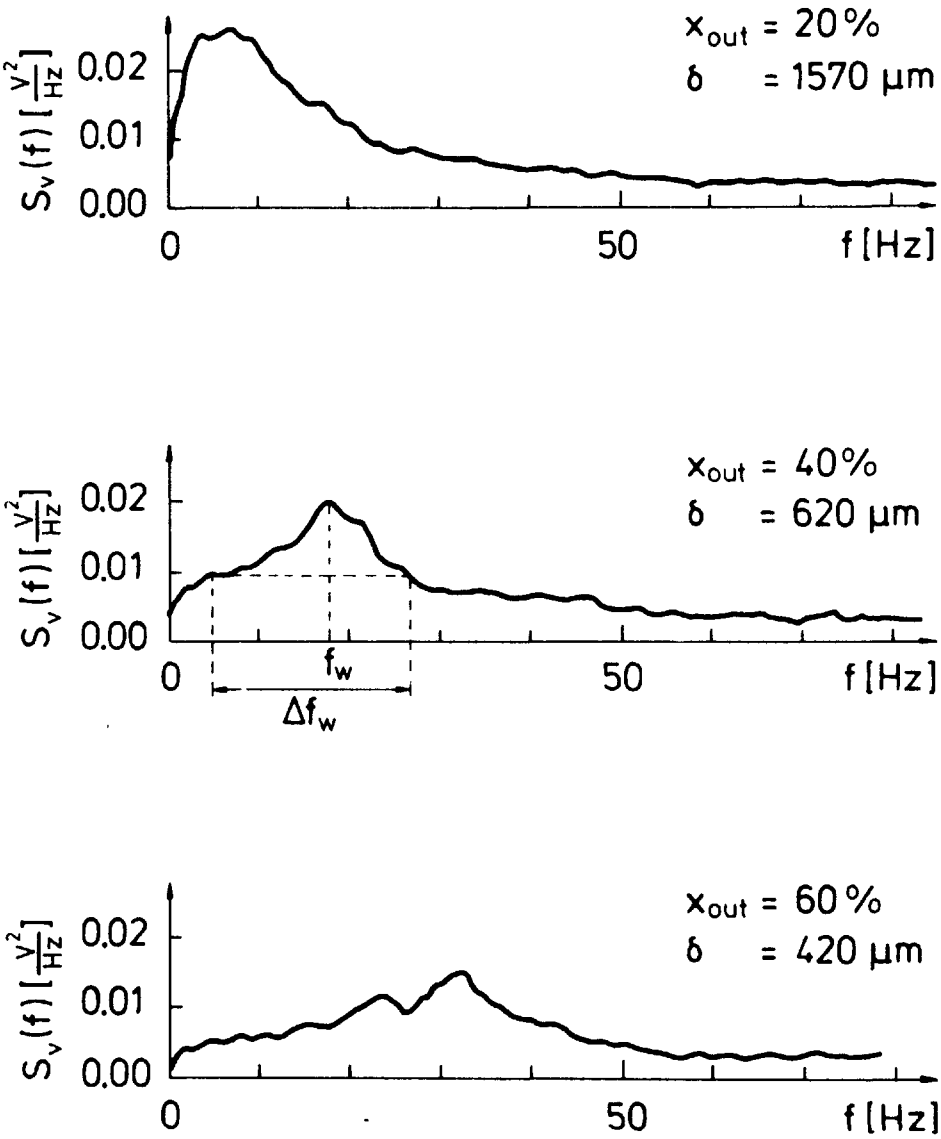

Fig. 3.35. Examples of Power Spectra of Needle Signals.
Test Section 20. Adiabatic. p = 70 bar. G = 500 kg/m^{2}s.

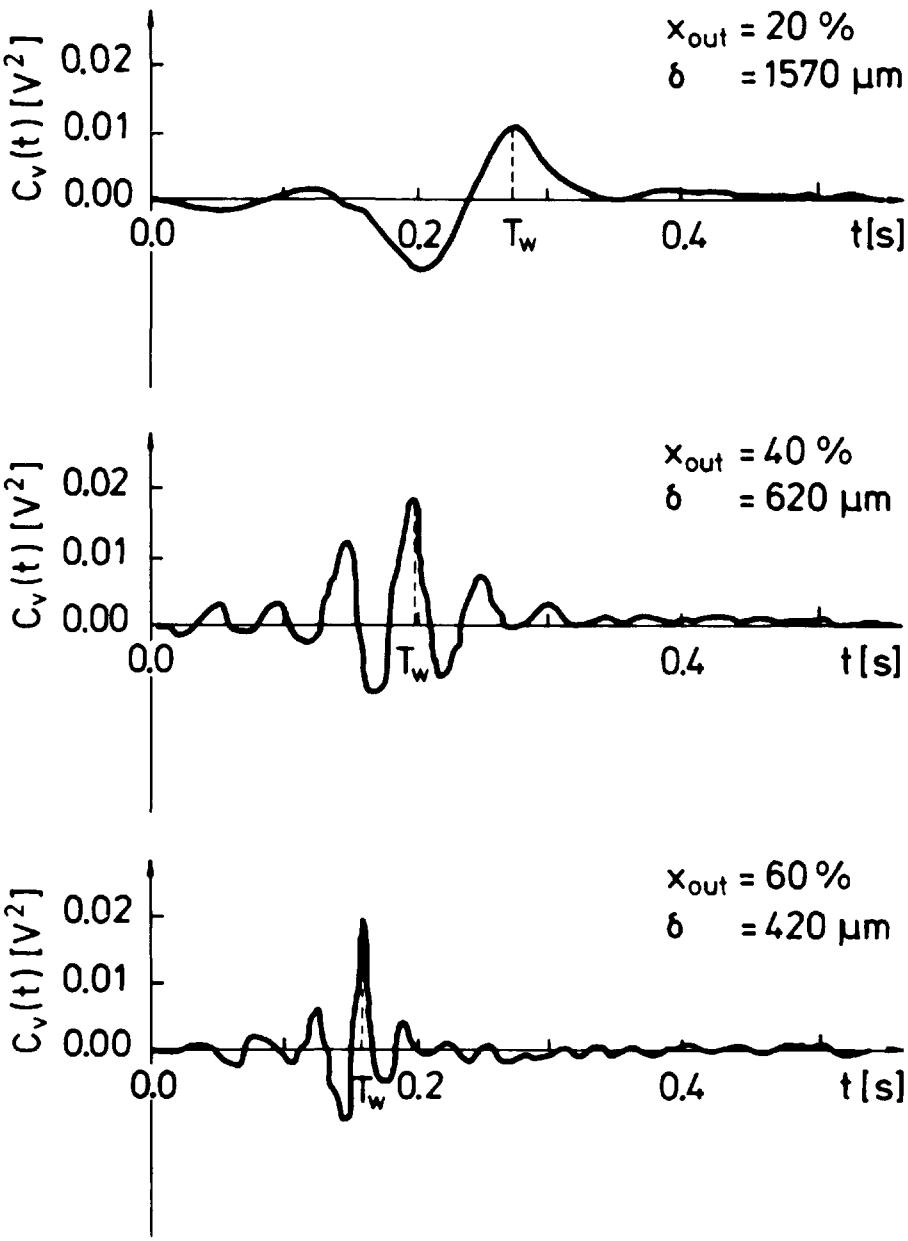

Fig. 3.36. Examples of Cross-Correlations of Needle Signals. Test Section 20. Adiabatic. p = 70 bar. G = 500 kg/m^2s.

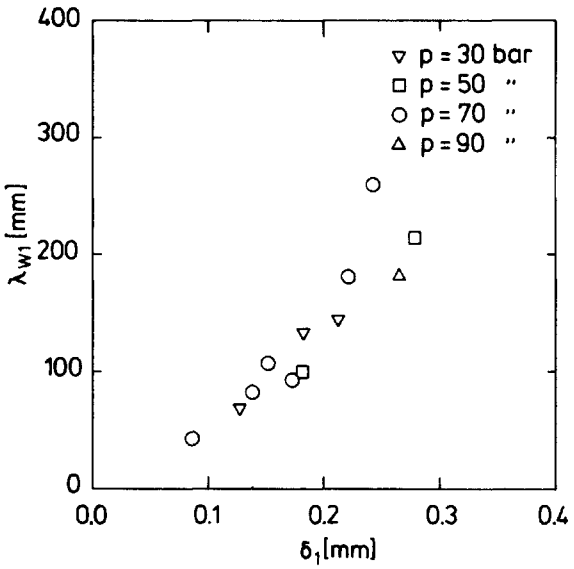

Fig. 3.37. Measurements of Wavelength of Roll Waves on Rod.
Test Section 17/26L. Adiabatic.

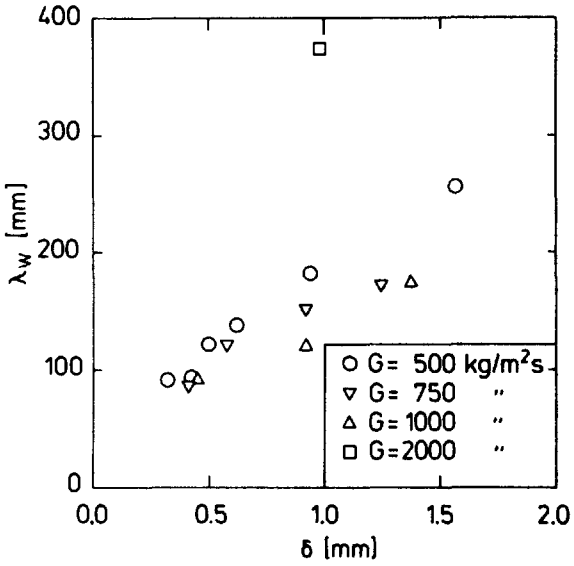

Fig. 3.38. Measurements of Wavelength of Roll Waves.
Test Section 20. Adiabatic. p = 70 bar.

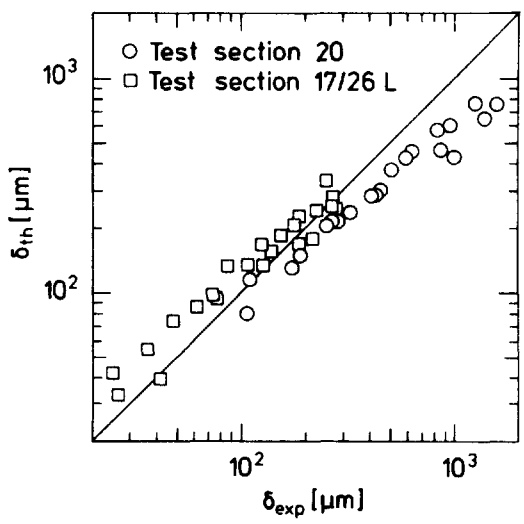

Fig. 4.1. Comparison between Experimental and Theoretical Film Thicknesses.
Test Sections 20 and 17/26L. Adiabatic.
P = 30-90 bar.

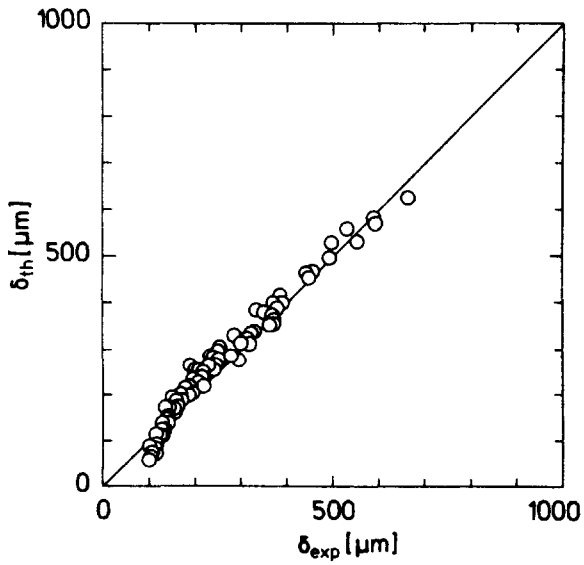

Fig. 4.2. Comparison between Experimental and Theoretical Film Thicknesses.
Whalley, Hewitt and Hutchinson (1973).
Air-Water. p = 2-4 bar. r_2 = 0.0159 m.
L_a = 18.9 m.

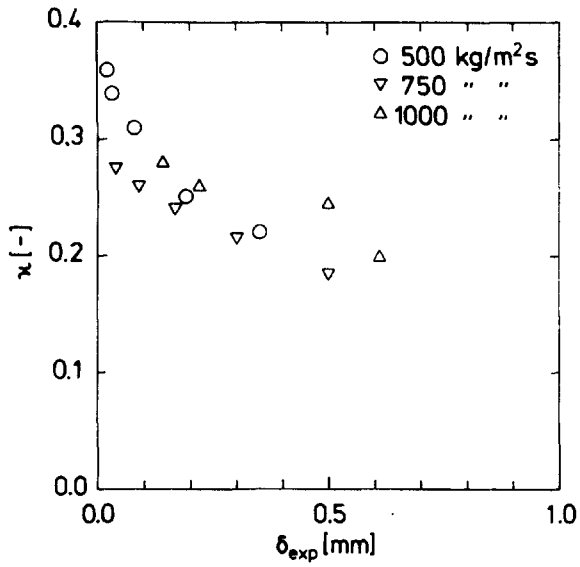

Fig. 4.3. Von Kármán's Constant Versus Experimental Film Thickness.
Kirillov et al. (1973).
Tube. r_2 = 0.0085 m. l = 4.68 m.
p = 68.6 bar.

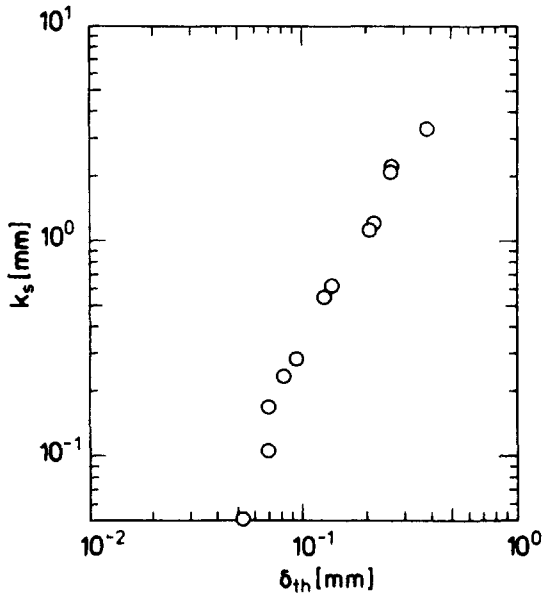

Fig. 4.4.a. Equivalent Sand Roughness Versus Theoretical Film Thickness.
Test Section 10. Adiabatic. p = 30 bar.

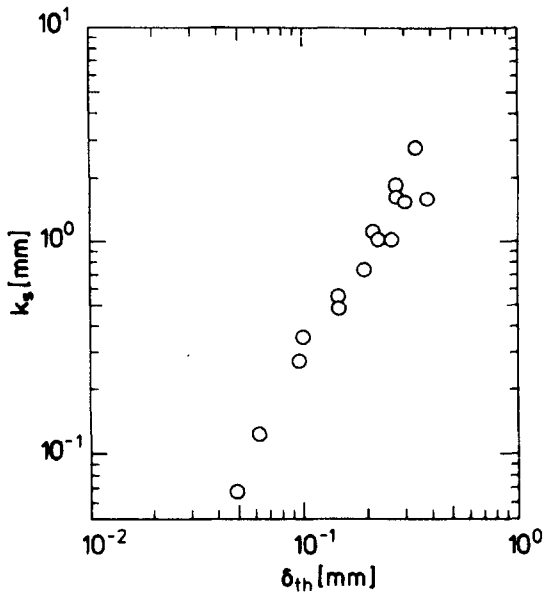

Fig. 4.4.b. Equivalent Sand Roughness Versus Theoretical Film Thickness.
Test Section 10. Adiabatic. p = 50 bar.

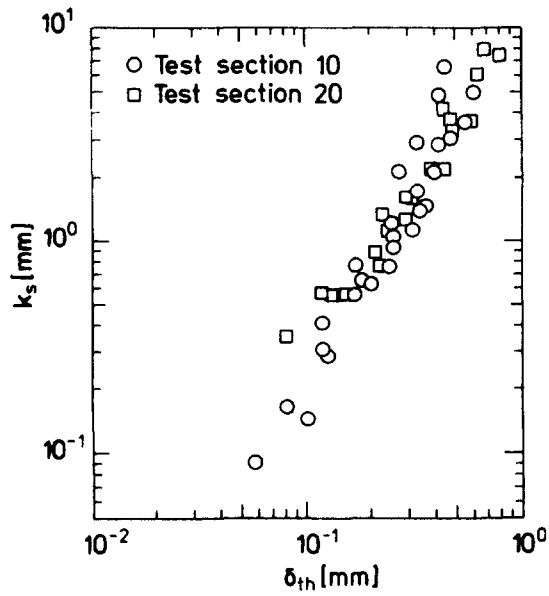

Fig. 4.4.c. Equivalent Sand Roughness Versus Theoretical Film Thickness.
Adiabatic. p = 70 bar.

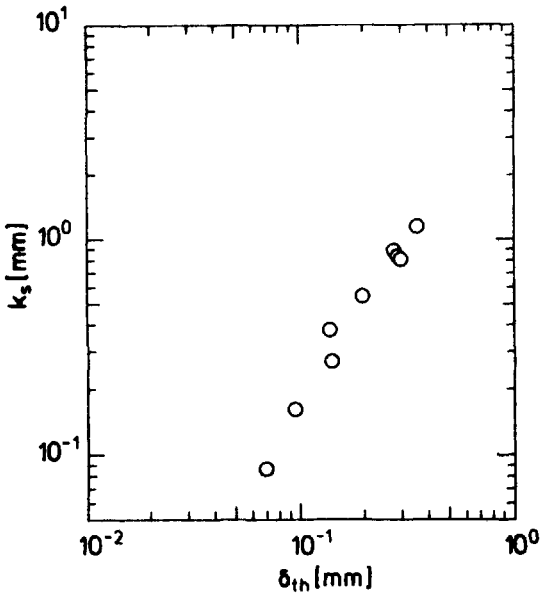

Fig. 4.4.d. Equivalent Sand Roughness Versus Theoretical Film Thickness.
Test Section 10. Adiabatic. p = 90 bar.

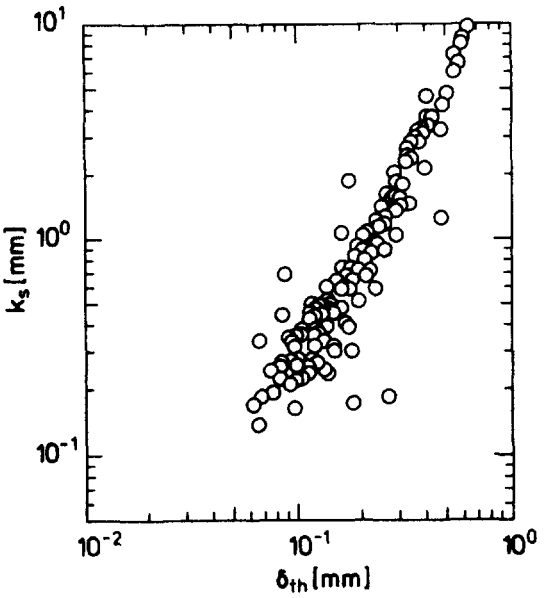

Fig. 4.5. Equivalent Sand Roughness Versus Theoretical Film Thickness.
Whalley, Hewitt and Hutchinson (1973).
Air-Water. p = 2-4 bar. r_2 = 0.0159 m.
L_a = 18.9 m.

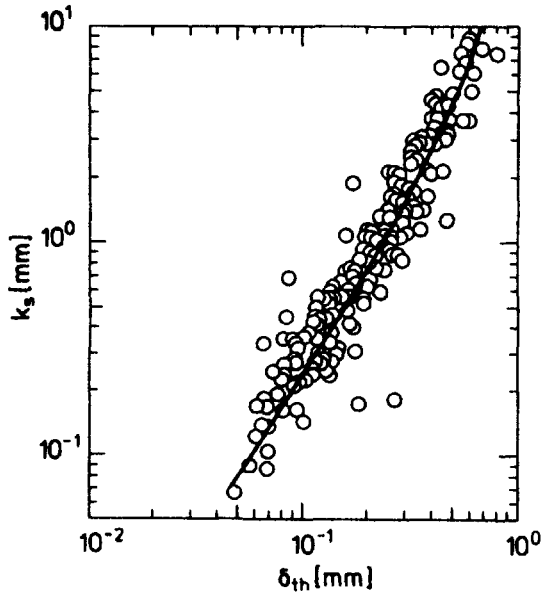

Fig. 4.6. Equivalent Sand Roughness Versus Theoretical Film Thickness.
Summary of Figs. 4.4.a-d and Fig. 4.5.

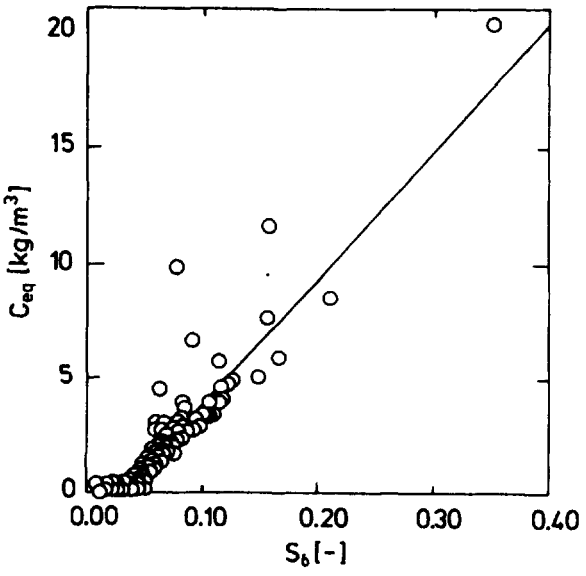

Fig. 4.7. Droplet Concentration Versus Entrainment Parameter.
Air-Water. p = 2-4 bar. r_2 = 0.0159 m.
L_a = 18.9 m.
Whalley, Hewitt and Hutchinson (1973).

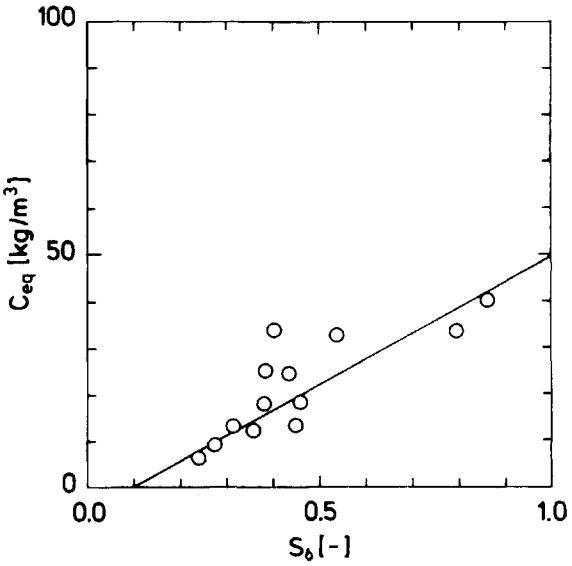

Fig. 4.8.a. Droplet Concentration Versus Entrainment Parameter.
Test Section 10. Adiabatic.
p = 30 bar.

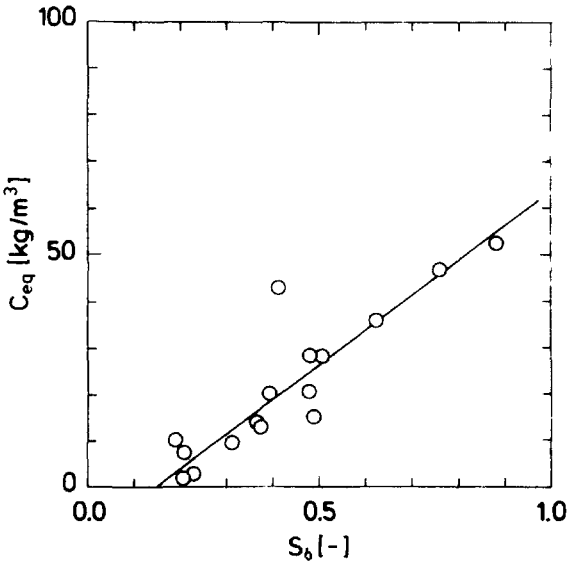

Fig. 4.8.b. Droplet Concentration Versus Entrainment Parameter.
Test Section 10. Adiabatic.
p = 50 bar.

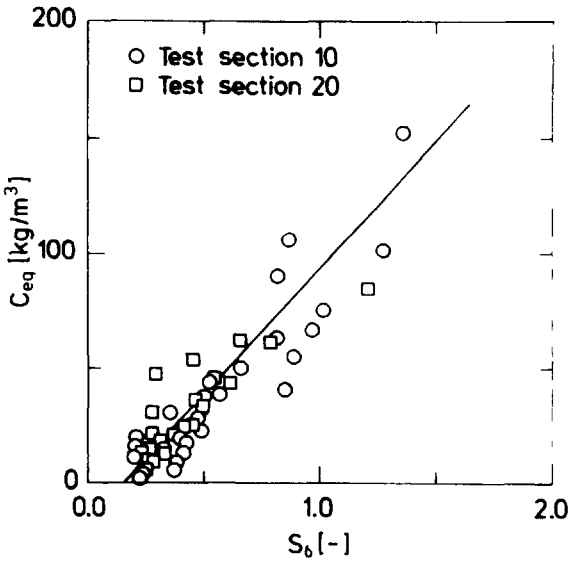

Fig. 4.8.c. Droplet Concentration Versus Entrainment Parameter.
Test Sections 10 and 20. Adiabatic.
p = 70 bar.

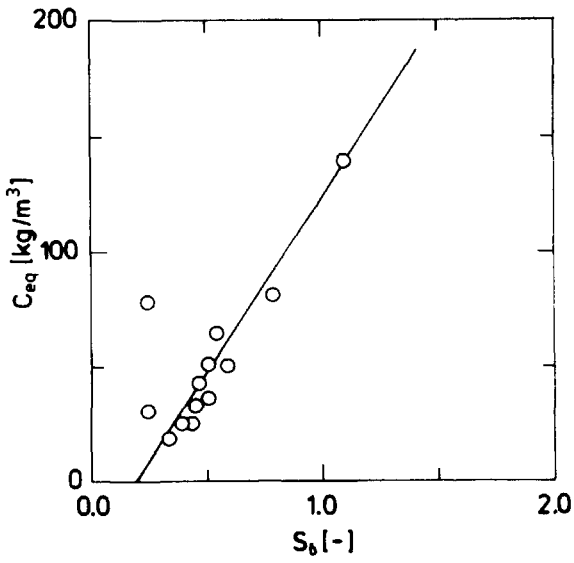

Fig. 4.8.d. Droplet Concentration Versus Entrainment Parameter.
Test Section 10. Adiabatic.
p = 90 bar.

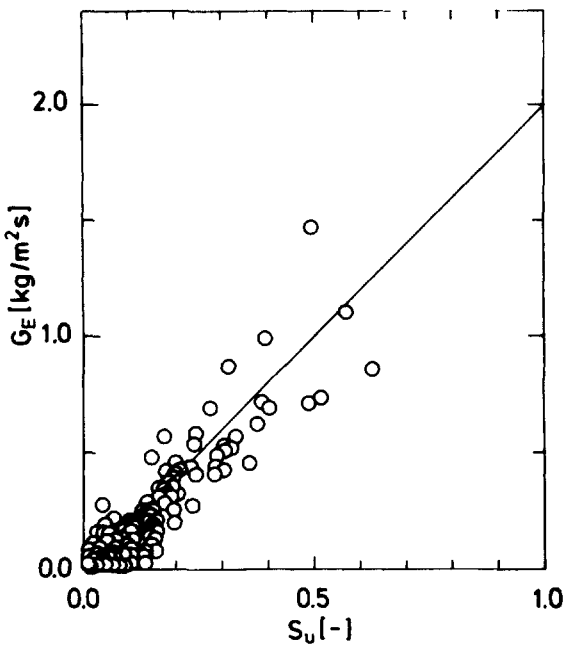

Fig. 4.9.a. Entrainment Correlation. Air-Water. p = 2-4 bar. r_2 = 0.0159 m. L_a = 18.9 m. Whalley, Hewitt and Hutchinson (1973).

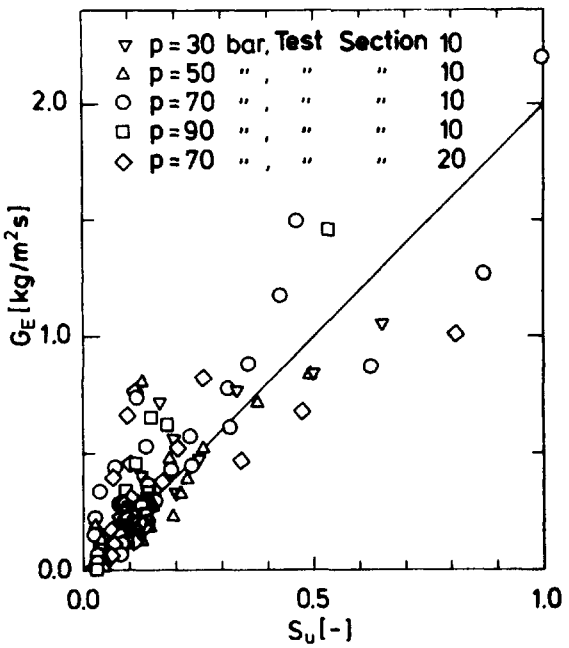

Fig. 4.9.b. Entrainment Correlation. Steam-Water. Test Sections 10 and 20. Adiabatic. p = 30-90 bar.

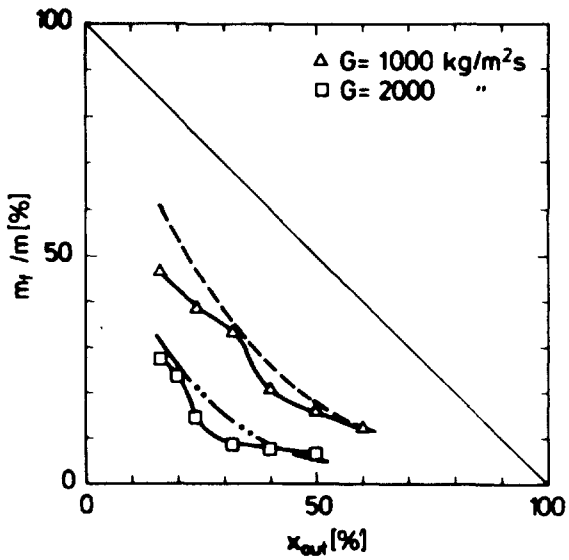

Fig. 4.10.a. Comparison between Measured and Predicted Film Flow Rates. Test Section 10. Adiabatic. P = 30 bar. The Symbols and Solid Lines Apply to the Measurements. The Stippled Lines Apply to the Predictions:
— — — : G = 1000 kg/m²s
— .. — : G = 2000 -

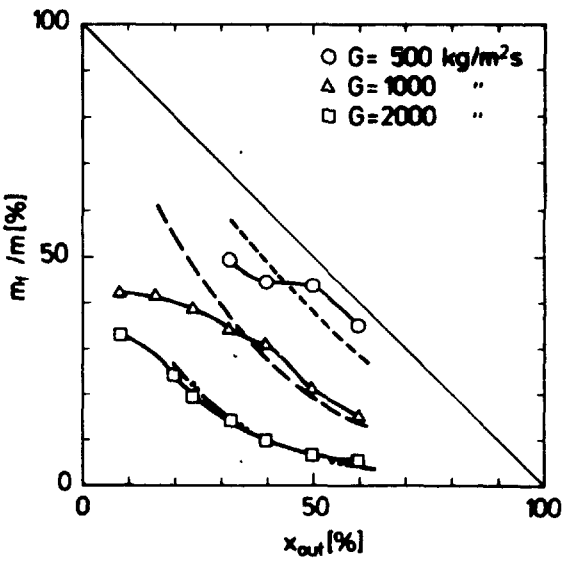

Fig. 4.10.b. Comparison between Measured and Predicted Film Flow Rates. Test Section 10. Adiabatic. P = 50 bar. The Symbols and Solid Lines Apply to the Measurements. The Stippled Lines Apply to the Predictions:
- - - - : G = 500 kg/m²s
— — — : G = 1000 -
— .. — : G = 2000 -

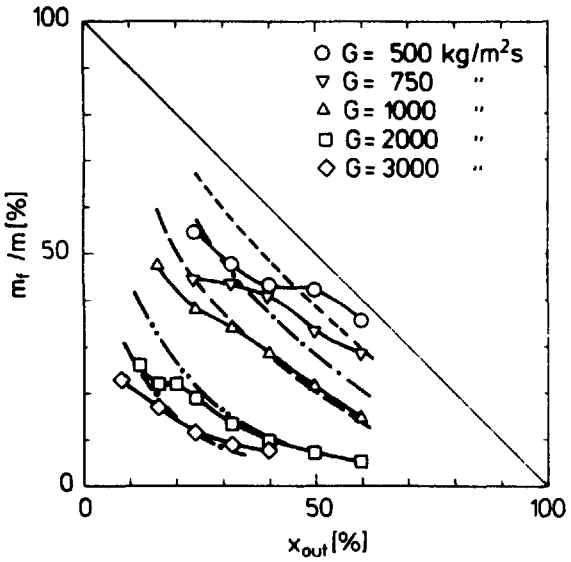

Fig. 4.10.c. Comparison between Measured and Predicted Film Flow Rates.
Test Section 10. Adiabatic. P = 70 bar.
The Symbols and Solid Lines Apply to the Measurements. The Stippled Lines Apply to the Predictions:
- - - - : G = 500 kg/m²s
— . — : G = 750 -
— — — : G = 1000 -
— .. — : G = 2000 -
— — . : G = 3000 -

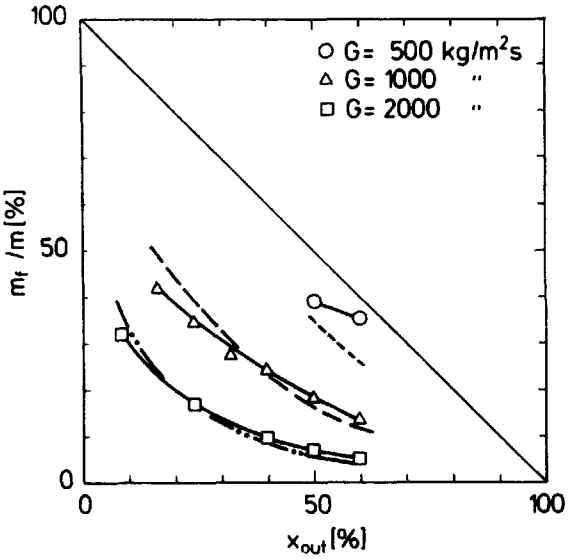

Fig. 4.10.d. Comparison between Measured and Predicted Film Flow Rates.
Test Section 10. Adiabatic. P = 90 bar.
The Symbols and Solid Lines Apply to the Measurements. The Stippled Lines Apply to the Predictions:
- - - - : G = 500 kg/m²s
— — — : G = 1000 -
— .. — : G = 2000 -

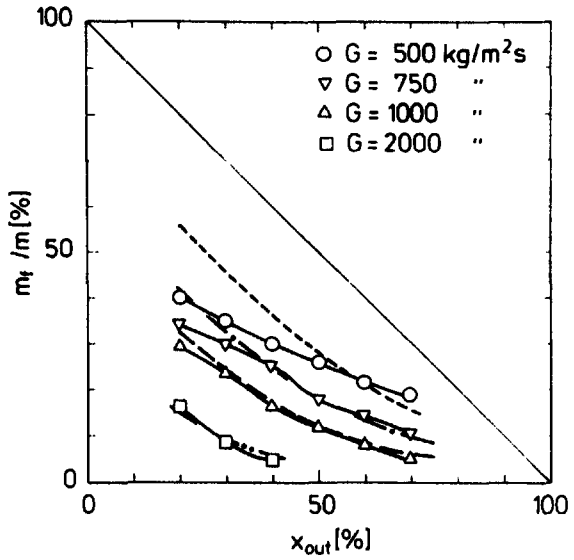

Fig. 4.11. Comparison between Measured and Predicted Film Flow Rates.
Test Section 20. Adiabatic. P = 70 bar
The Symbols and Solid Lines Apply to the Measurements. The Stippled Lines Apply to the Predictions:
- - - - : G = 500 kg/m²s
— . — : G = 750 -
— — — : G = 1000 -
— .. — : G = 2000 -

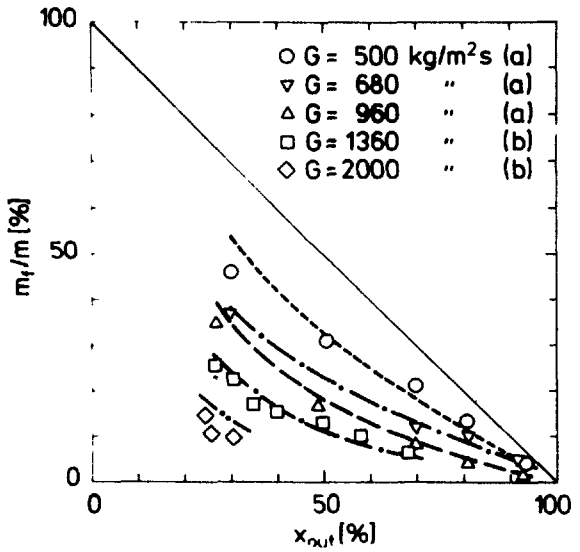

Fig. 4.12 Comparison between Measured and Predicted Film Flow Rates.
The Symbols Apply to Measurements by:
(a) Singh et al. (1969). d_2 = 12.5 mm
(b) Keeys et al. (1970a). d_2 = 12.7 mm
Adiabatic. P = 69 bar.
The Stippled Lines Apply to the Predictions:
- - - - : G = 550 kg/m²s
— . — : G = 860 -
— — — : G = 960 -
— — . : G = 1360 -
— .. — : G = 2000 -

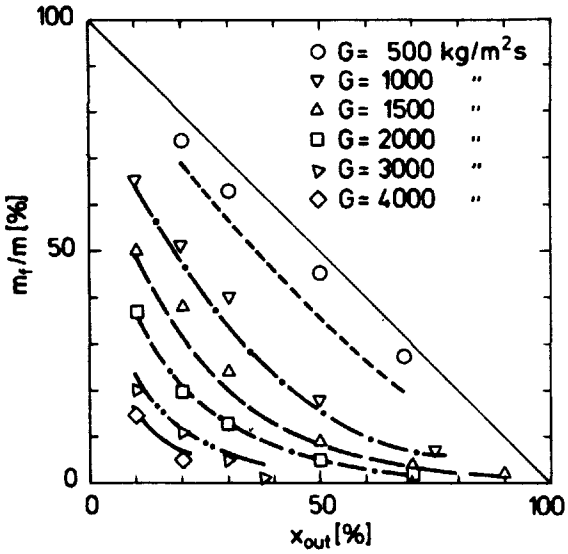

Fig. 4.13. Comparison between Measured and Predicted Film Flow Rates.
The Symbols Apply to Measurements by Nigmatulin, Malyshenko and Shugaev (1976).
d_2 = 13.3 mm. Adiabatic. P = 50 bar.
The Stippled Lines Apply to the Predictions:

- - - - : G = 500 kg/m²s
— . — : G = 1000 -
— — — : G = 1500 -
— — . : G = 2000 -
— .. — : G = 3000 -
———— : G = 4000 -

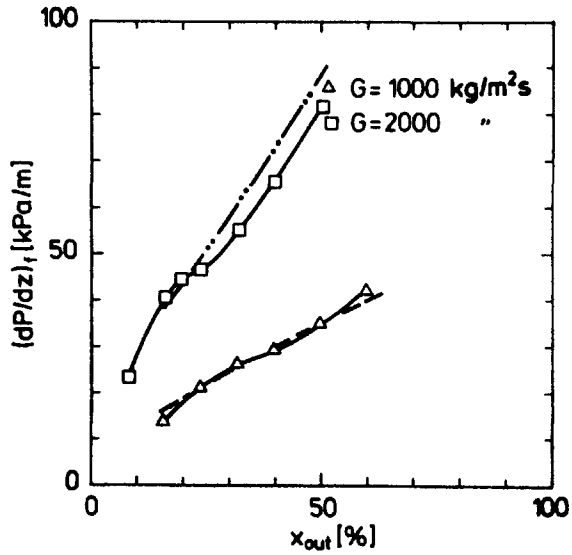

Fig. 4.14.a. Comparison between Measured and Predicted Frictional Pressure Gradients.
Test Section 10. Adiabatic. P = 30 bar.
The Symbols and Solid Lines Apply to the Measurements. The Stippled Lines Apply to the Predictions:

— — — : G = 1000 kg/m²s
— .. — : G = 2000 -

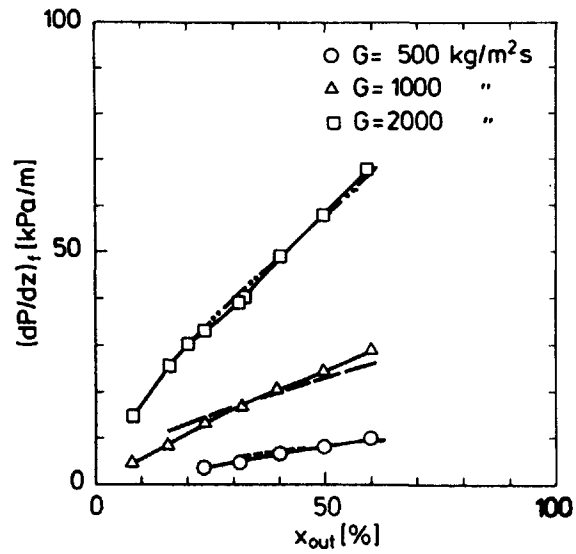

Fig. 4.14.b. Comparison between Measured and Predicted Frictional Pressure Gradients.
Test Section 10. Adiabatic. P = 50 bar.
The Symbols and Solid Lines Apply to the Measurements. The Stippled Lines Apply to the Predictions:

- - - - : G = 500 kg/m²s
— — — : G = 1000 -
— .. — : G = 2000 -

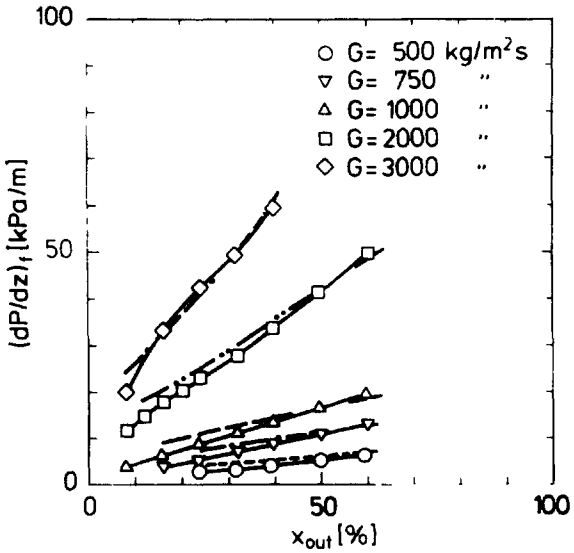

Fig. 4.14.c. Comparison between Measured and Predicted Frictional Pressure Gradients.
The Section 10. Adiabatic. P = 70 bar.
The Symbols and Solid Lines Apply to the Measurements. The Stippled Lines Apply to the Predictions:
- - - - : G = 500 kg/m^{2}s
— . — : G = 750 -
— — — : G = 1000 -
— .. — : G = 2000 -
— . — : G = 3000 -

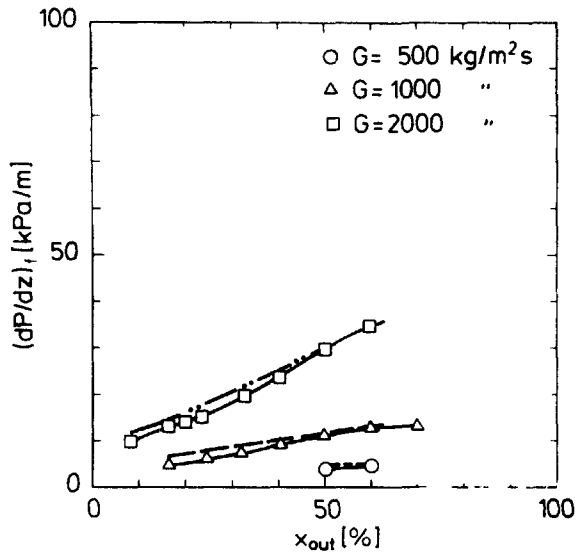

Fig. 4.14.d. Comparison between Measured and Predicted Frictional Pressure Gradients.
Test Section 10. Adiabatic. P = 90 bar.
The Symbols and Solid Lines Apply to the Measurements. The Stippled Lines Apply to the Predictions:
- - - - : G = 500 kg/m^{2}s
— — — : G = 1000 -
— .. — : G = 2000 -

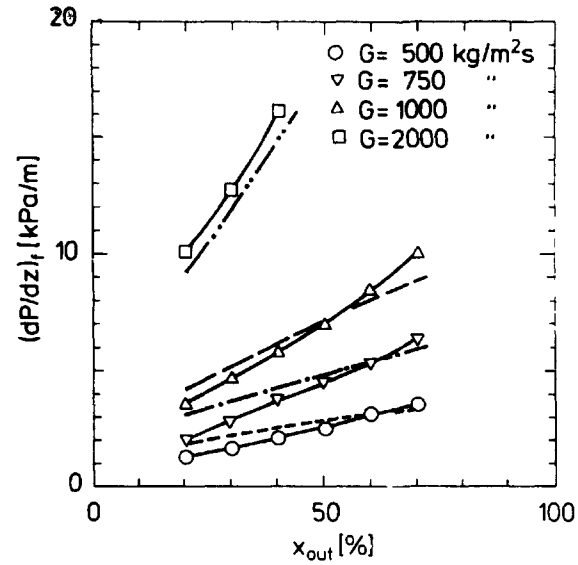

Fig. 4.15. Comparison between Measured and Predicted Frictional Pressure Gradients.
Test Section 20. Adiabatic. P = 70 bar.
The Symbols and Solid Lines Apply to the Measurements. The Stippled Lines Apply to the Predictions:
- - - - : G = 500 kg/m^{2}s
— . — : G = 750 -
— — — : G = 1000 -
— .. — : G = 2000 -

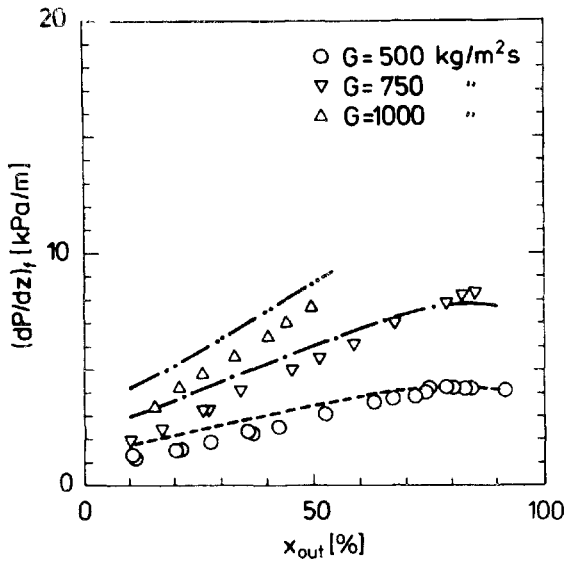

Fig. 4.16. Comparison between Measured and Predicted Frictional Pressure Gradients.
The Symbols Apply to the Measurements by Kirillov et al. (1973). Tubular Test Section. d_2 = 17 mm. L_a = 4.68 m. Adiabatic. P = 68.6 bar. The Stippled Lines Apply to the Predictions:
- - - - : G = 500 kg/m^{2}s
— . — : G = 750 -
— .. — : G = 1000 -

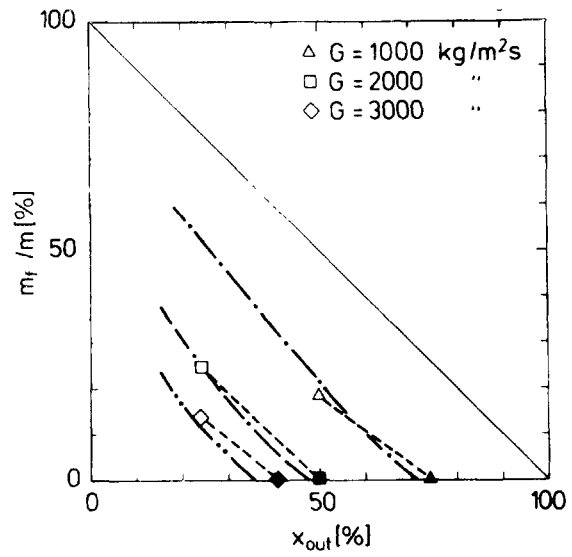

Fig. 4.17.a. Comparison between Measured and Predicted Film Flow Rates and Burnout Steam Qualities.
Test Section 10. Diabatic. P = 30 bar. q" = 100 W/cm^2. L_d = 4.02 m.
The Symbols Apply to the Measurements. The Stippled Lines Apply to the Predictions:
— . — : G = 1000 kg/m^{2}s
— — . : G = 2000 -
— .. — : G = 3000 -

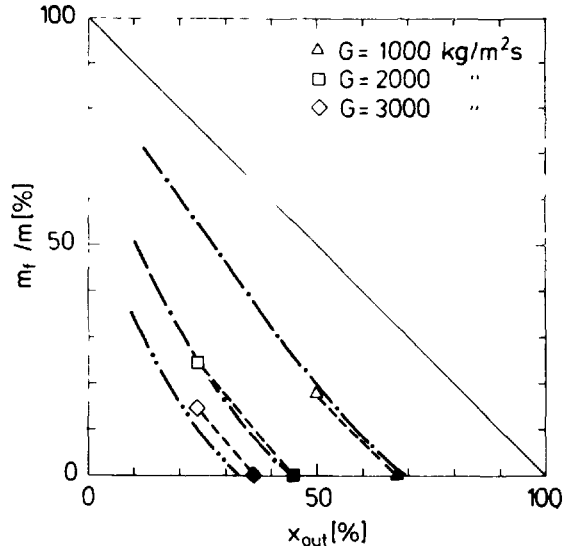

Fig. 4.17.b. Comparison between Measured and Predicted Film Flow Rates and Burnout Steam Qualities.
Test Section 10. Diabatic. P = 50 bar. q" = 100 W/cm^2. L_d = 4.02 m.
The Symbols Apply to the Measurements. The Stippled Lines Apply to the Predictions:
— . — : G = 1000 kg/m^{2}s
— — . : G = 2000 -
— .. — : G = 3000 -

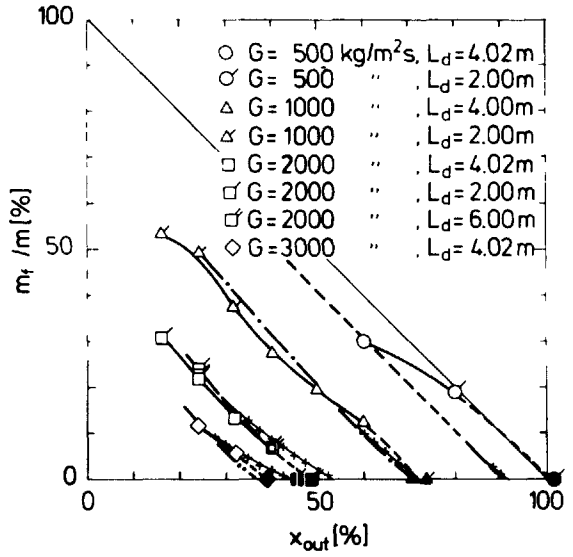

Fig. 4.17.c. Comparison between Measured and Predicted Film Flow Rates and Burnout Steam Qualities.
Test Section 10. Diabatic. P = 70 bar.
q" = 100 W/cm^2. L_d = 2.00-6.00 m.
The Symbols and Solid Lines Apply to the Measurements. The Stippled Lines Apply to the Predictions:
- - - - : G = 500 kg/m^{2}s
— . — : G = 1000 -
— — . : G = 2000 -
— .. — : G = 3000 -
✱-✱-✱ : Predictions with y_D = 0.

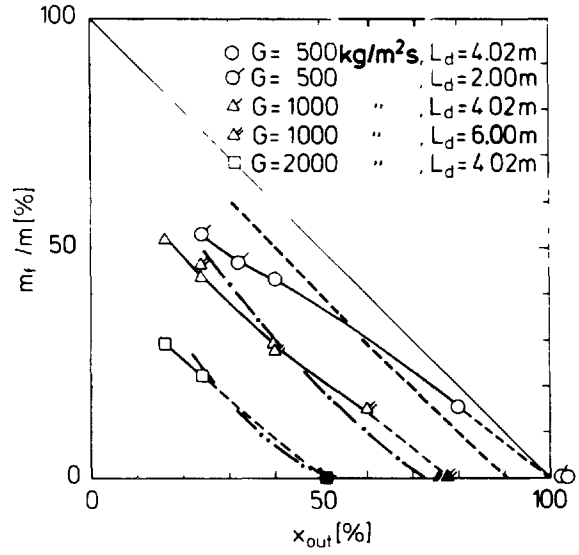

Fig. 4.17.d. Comparison between Measured and Predicted Film Flow Rates and Burnout Steam Qualities.
Test Section 10. Diabatic. P = 70 bar.
q" = 50 W/cm^2. L_d = 2.00-6.00 m.
The Symbols and Solid Lines Apply to the Measurements. The Stippled Lines Apply to the Predictions:
- - - - : G = 500 kg/m^{2}s
— . — : G = 1000 -
— .. — : G = 2000 -

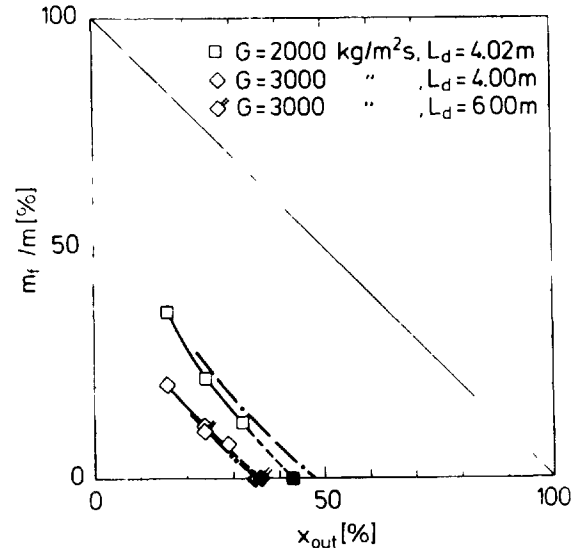

Fig. 4.17.e. Comparison between Measured and Predicted Film Flow Rates and Burnout Steam Qualities.
Test Section 10. Diabatic. P = 70 bar.
q" = 150 W/cm^2. L_d = 4.00-6.00 m.
The Symbols and Solid Lines Apply to the Measurements. The Stippled Lines Apply to the Predictions:
— — . : G = 2000 kg/m^{2}s
— .. — : G = 3000 -

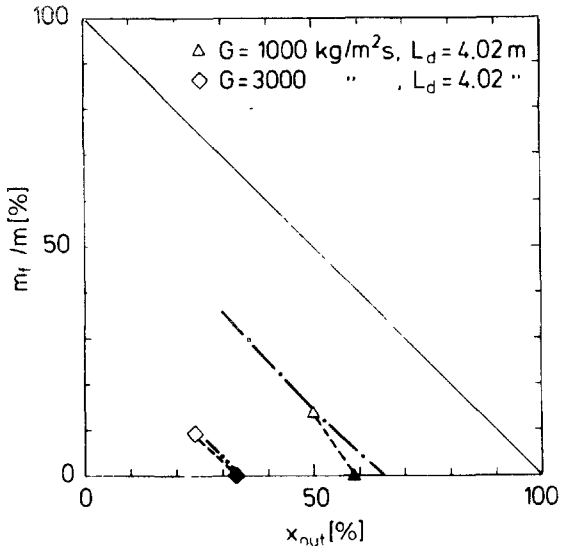

Fig. 4.17.f. Comparison between Measured and Predicted Film Flow Rates and Burnout Steam Qualities.
Test Section 10. Diabatic. P = 90 bar.
q" = 100 W/cm^2. L_d = 4.02 m.
The Symbols Apply to the Measurements.
The Stippled Lines Apply to the Predictions:
— . — : G = 1000 kg/m^{2}s
— .. — : G = 3000 -

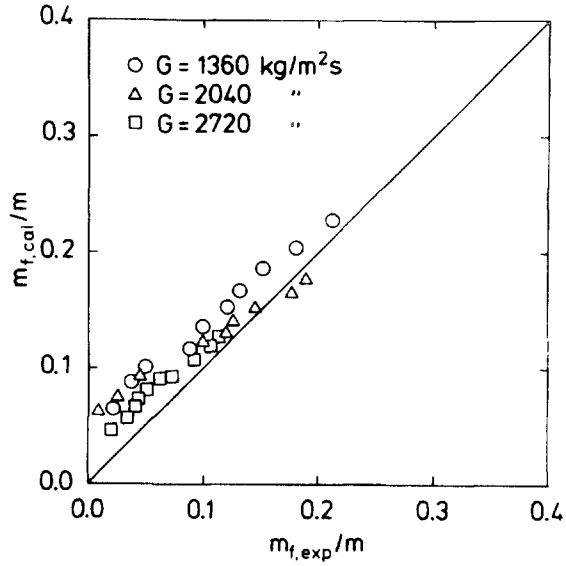

Fig. 4.18. Comparison between Measured and Predicted Film Flow Rates.
Measurements by Bennet et al. (1969).
Tubular Test Section. Diabatic.
d_2 = 12.7 mm. L_{d_2} = 3.66 m. P = 69 bar.
q" = 75-148 W/cm^2.

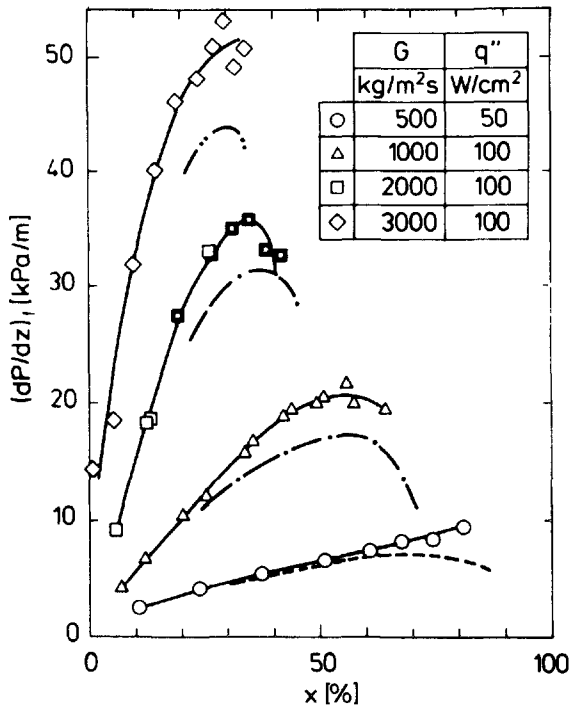

Fig. 4.19. Comparison between Measured and Predicted Frictional Pressure Gradients.
Test Section 10. Diabatic. P = 70 bar.
The Symbols and Solid Lines Apply to the Measurements. The Stippled Lines Apply to the Predictions:
- - - - : G = 500 kg/m^{2}s
— . — : G = 1000 -
— — . : G = 2000 -
— .. — : G = 3000 -

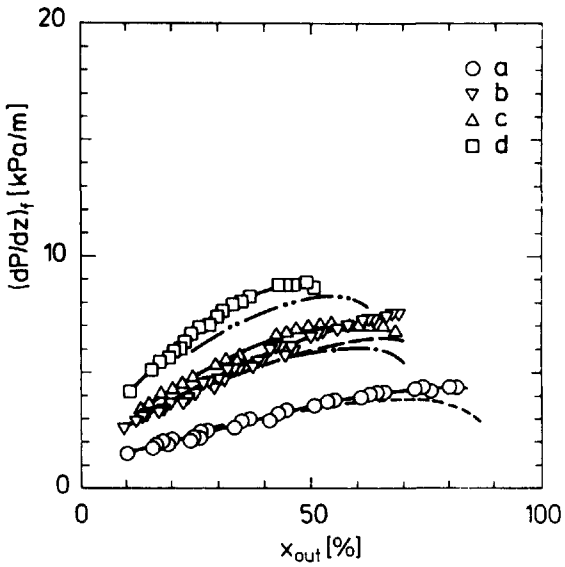

Fig. 4.20. Comparison between Measured and Predicted Frictional Pressure Gradients.
Measurements by Kirillov et al. (1973).
Tubular Test Section. d_2 = 17 mm.
L_d = 4.68 m. Diabatic. P = 68.6 bar.
The Symbols Apply to the Measurements.
The Stippled Lines Apply to the Predictions:

a: - - - - : G = 500 kg/m^{2}s, q" = 23W/cm^2
b: — — — : G = 750 - , q" = 23 -
c: — . — : G = 750 - , q" = 46 -
d: — .. — : G = 1000 - , q" = 46 -

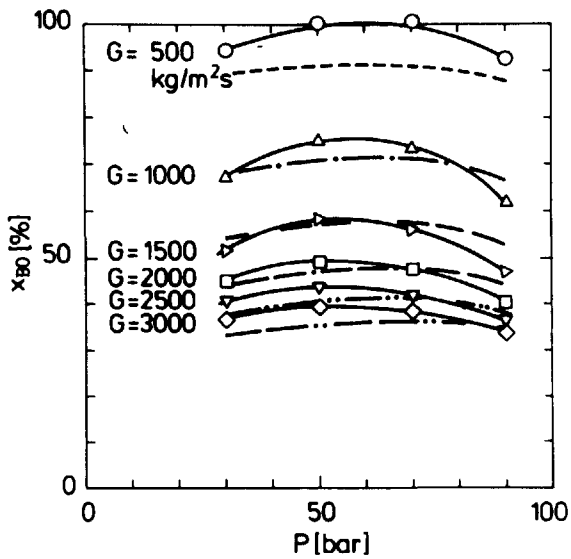

Fig. 4.21. Comparison between Measured and Predicted Burnout Steam Qualities.
Test Section 10. L_d = 4.02 m.
ΔT_{sub} = 10°C.
The Symbols and Solid Lines Apply to the Measurements. The Stippled Lines Apply to the Predictions:

- - - - : G = 500 kg/m^{2}s
— . — : G = 1000 -
— — — : G = 1500 -
— — . : G = 2000 -
— .. — : G = 2500 -
— — .. : G = 3000 -

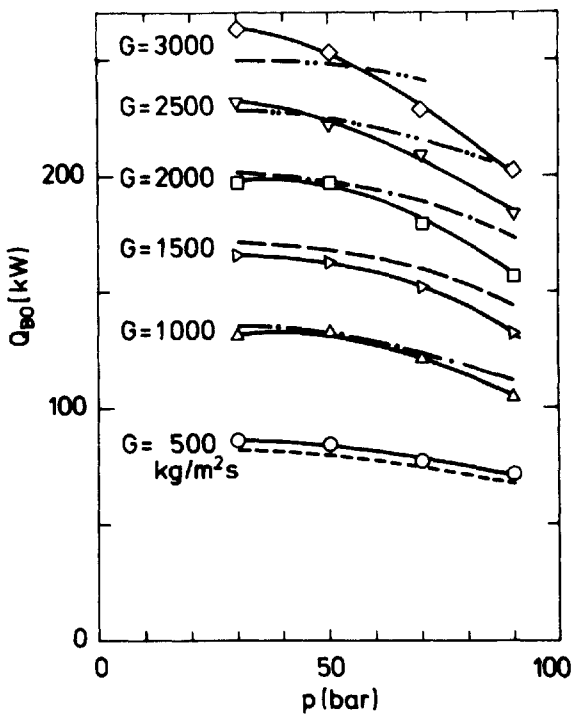

Fig. 4.22. Comparison between Measured and Predicted Burnout Powers.
Test Section 10. L_d = 4.02 m.
ΔT_{sub} = 100°C.
The Symbols and Solid Lines Apply to the Measurements. The Stippled Lines Apply to the Predictions:
- - - - - : G = 500 kg/m^{2}s
— . — : G = 1000 -
— — — : G = 1500 -
— — . : G = 2000 -
— .. — : G = 2500 -
— — .. : G = 3000 -

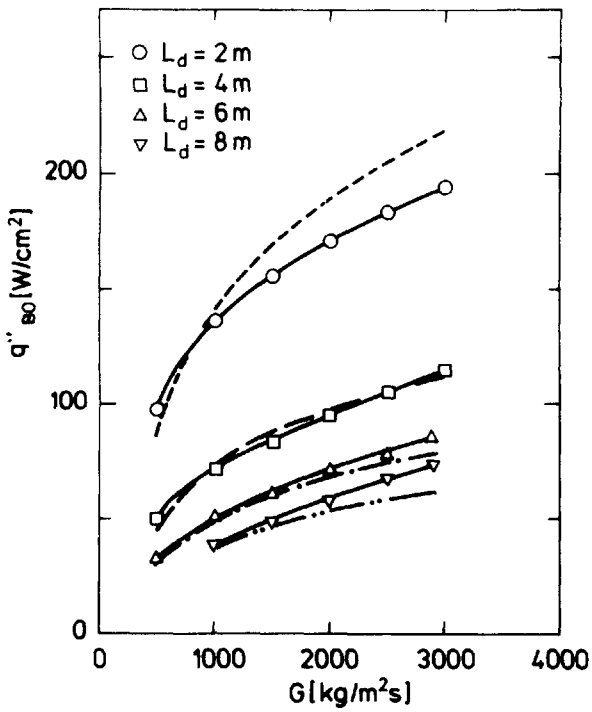

Fig. 4.23. Comparison between Measured and Predicted Burnout Heat Fluxes.
Test Section 10. P = 70 bar.
ΔT_{sub} = 10°C.
The Symbols and Solid Lines Apply to the Measurements. The Stippled Lines Apply to the Predictions:
- - - - : L_d = 2.02 m
— — — : L_d = 4.02 m
— . — : L_d = 6.00 m
— .. — : L_d = 8.00 m

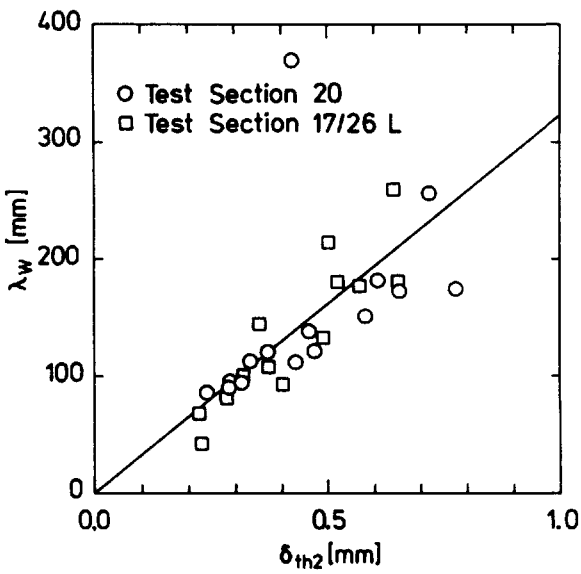

Fig. 4.24. Experimental Wavelength of Roll Waves Versus Theoretical Tube Film Thickness.
Test Sections 20 and 17/26L. Adiabatic.
p = 30-90 bar.

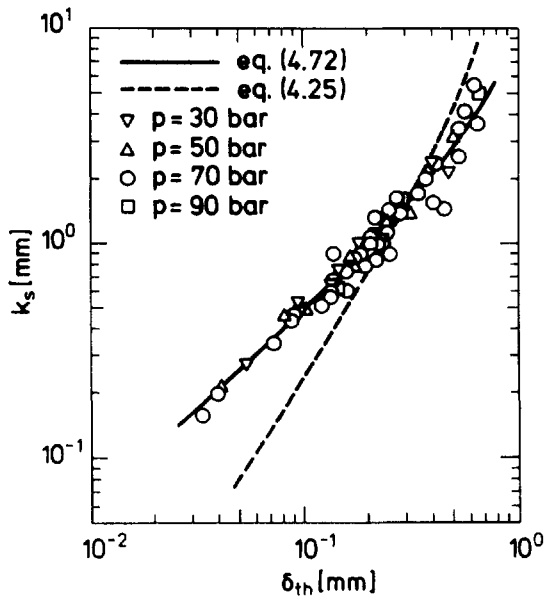

Fig. 4.25. Equivalent Sand Roughness Versus Theoretical Film Thickness.
Annular Test Section 17/26L. Adiabatic.

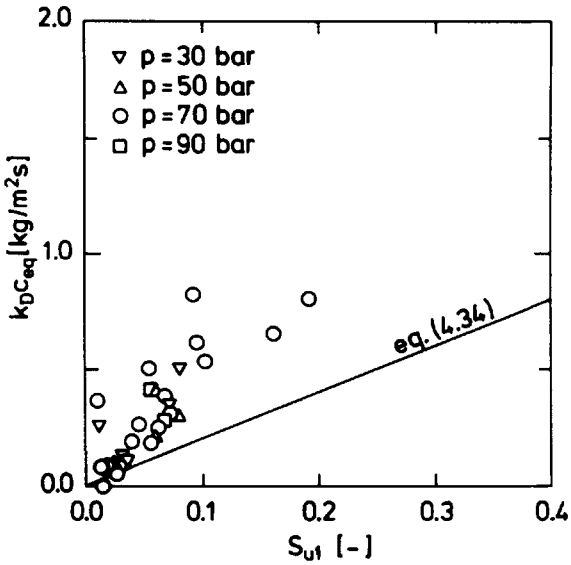

Fig. 4.26.a. Entrainment Correlation.
Test Section 17/26L. Rod. Adiabatic.
The Values Given in Table 4.2 Are Used for k_D.

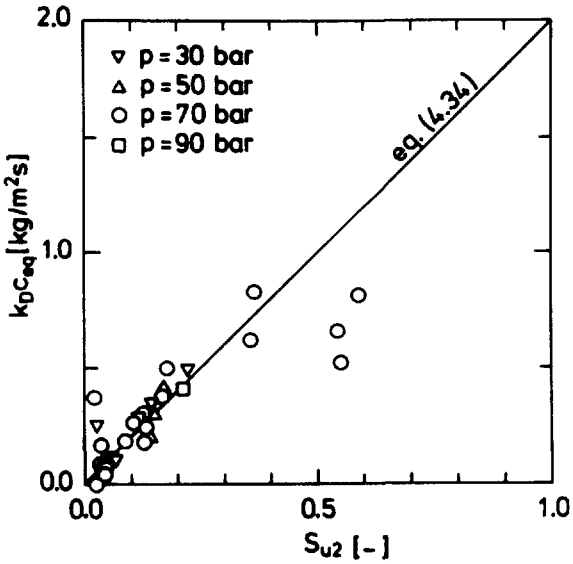

Fig. 4.26.b. Entrainment Correlation.
Test Section 17/26L. Tube. Adiabatic.
The Values Given in Table 4.2 Are Used for k_D.

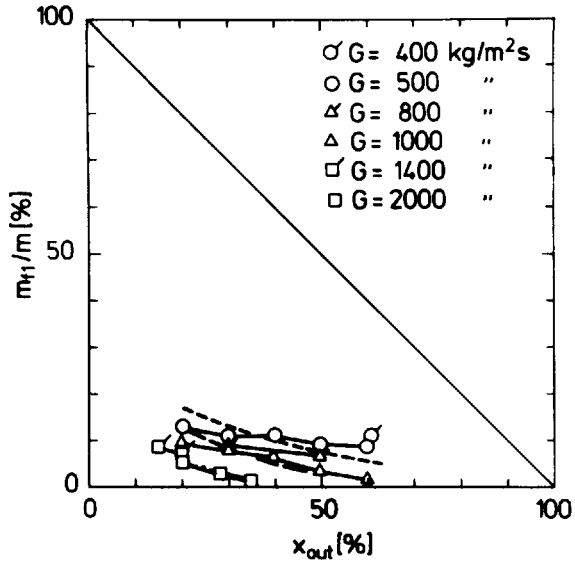

Fig. 4.27.a. Comparison between Measured and Predicted Rod Film Flow Rates.
Test Section 17/26L. Adiabatic.
P = 70 bar.
The Symbols and Solid Lines Apply to the Measurements. The Stippled Lines Apply to the Predictions:
- - - - : G = 500 kg/m^{2}s
— — — : G = 1000 -
— .. — : G = 2000 -

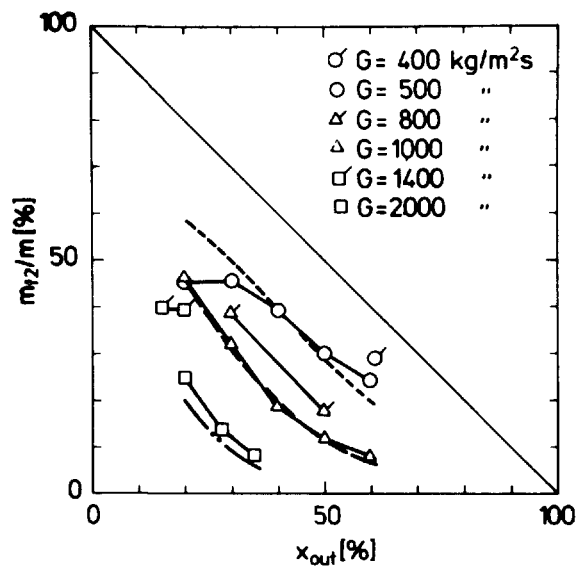

Fig. 4.27.b. Comparison between Measured and Predicted Tube Film Flow Rates.
Test Section 17/26L. Adiabatic.
P = 70 bar.
The Symbols and Solid Lines Apply to the Measurements. The Stippled Lines Apply to the Predictions:
- - - - : G = 500 kg/m^{2}s
— — — : G = 1000 -
— .. — : G = 2000 -

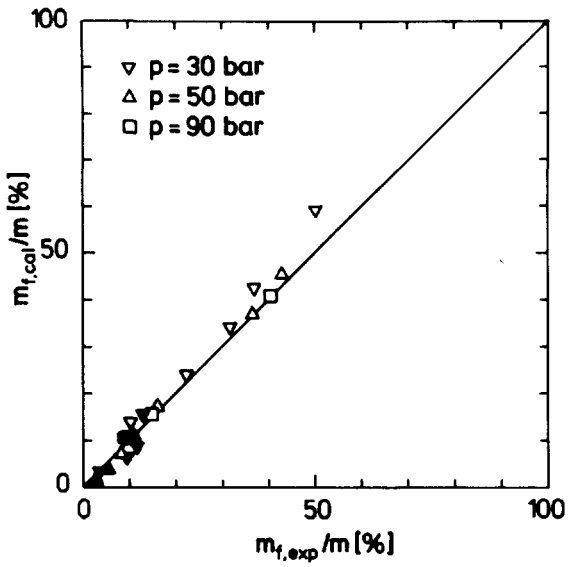

Fig. 4.28. Comparison between Measured and Predicted Film Flow Rates.
Test Section 17/26L. Adiabatic.
P = 30,50 and 90 bar.
Solid Symbols Apply to the Rod Film.
Open Symbols Apply to the Tube Film.

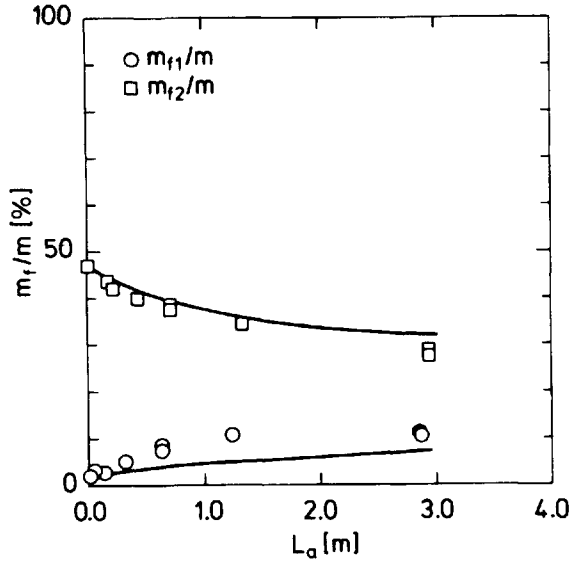

Fig. 4.29. Comparison between Measured and Predicted Film Flow Rates.
The Symbols Apply to the Measurements by Moeck (1970): Annular Test Section d_1 = 19.7 mm. d_2 = 23.8 mm. P = 70 bar. G = 1360 kg/m^{2}s. x_{out} = 28%. Adiabatic.
The Solid Lines Apply to the Predictions.

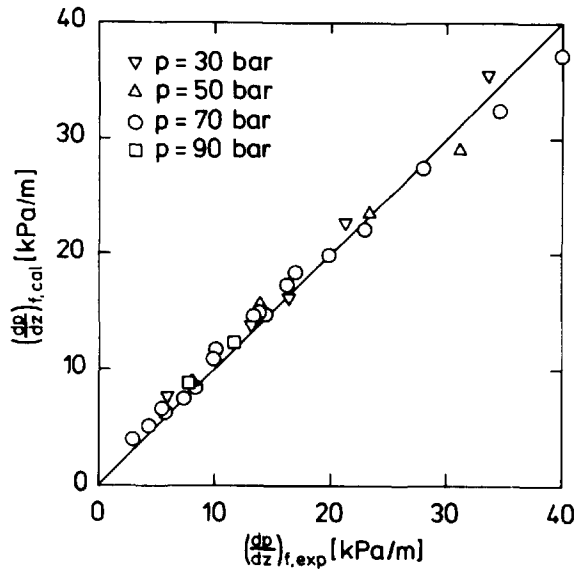

Fig. 4.30. Comparison between Measured and Predicted Frictional Pressure Gradients. Test Section 17/26L. Adiabatic P = 30-90 bar.

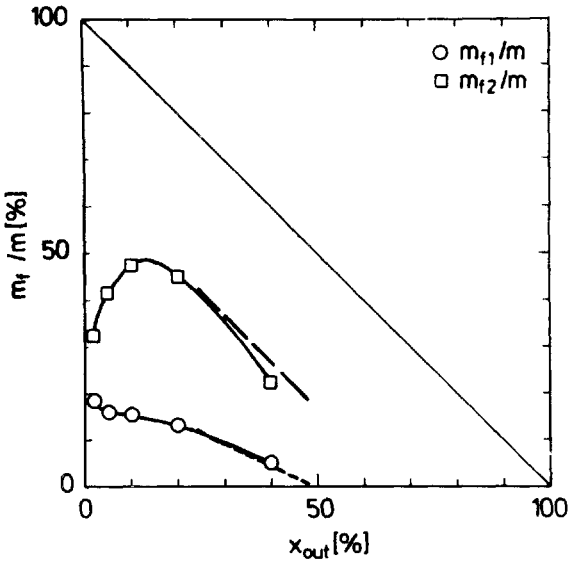

Fig. 4.31.a. Comparison between Measured and Predicted Film Flow Rates.
Test Section 17/26S. Diabatic.
P = 70 bar. G = 1000 kg/m^{2}s. $q_1'' = q_2''$ = 45 W/cm^2.
The Symbols and Solid Lines Apply to the Measurements. The Stippled Lines Apply to the Predictions:
- - - - : m_{f1}/m
— — — : m_{f2}/m

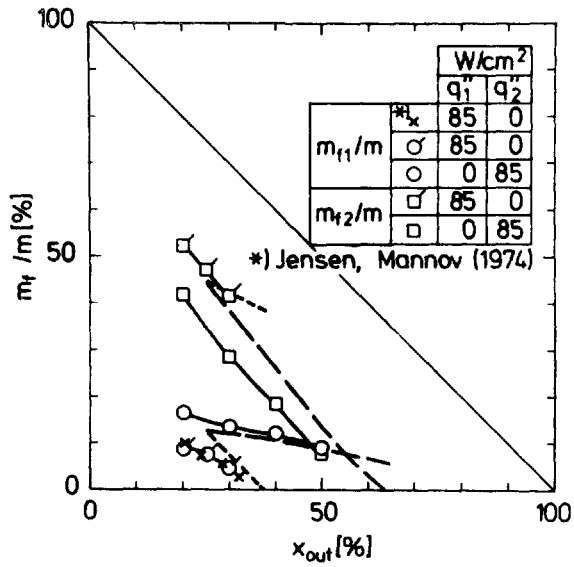

Fig. 4.31.b. Comparison between Measured and Predicted Film Flow Rates.
Test Section 17/26 S. Diabatic.
P = 70 bar. G = 900 kg/m^{2}s.
The Symbols and Solid Lines Apply to the Measurements. The Stippled Lines Apply to the Predictions:
- - - - : q_{1_w}'' = 85 W/cm^2, q_{2_w}'' = 0 W/cm^2
— — — : q_1'' = 0 - , q_2'' = 85 -

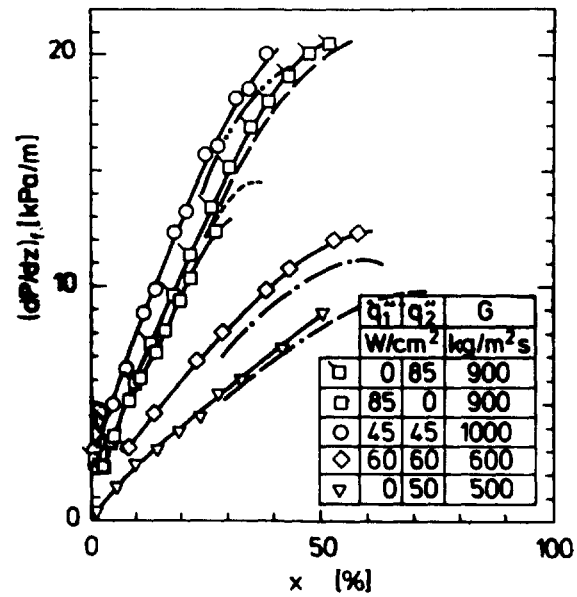

Fig. 4.32. Comparison between Measured and Predicted Frictional Pressure Gradients.
Test Section 17/26S. Diabatic. P = 70 bar
The Symbols and Solid Lines Apply to the Measurements. The Stippled Lines Apply to the Predictions:
— — . : G = 500 kg/m^{2}s, q_{1_w}'' = 0 W/cm^2
— . — : G = 600 - , q_{1_w}'' = 60 -
— — — : G = 900 - , q_{1_w}'' = 0 -
- - - - : G = 900 - , q_{1_w}'' = 85 -
— .. — : G = 1000 - , q_1'' = 45 -

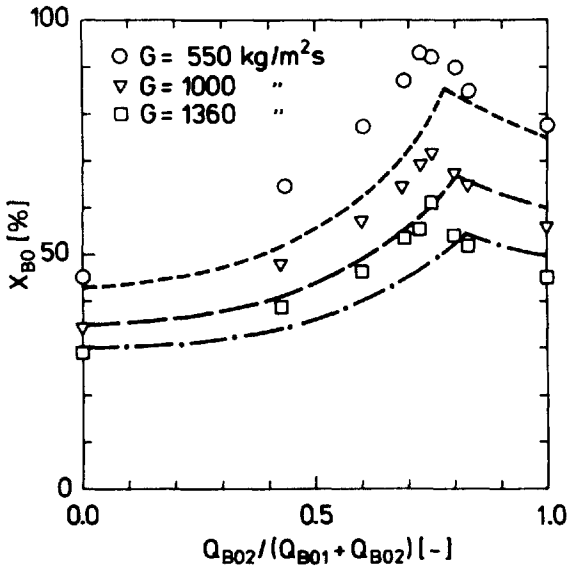

Fig. 4.33.a. Comparison between Measured and Predicted Burnout Steam Qualities. The Symbols Apply to the Measurements by Jensen and Mannov (1974): Test Section 17/26S. P = 70 bar. ΔT_{sub} = 10°C. The Stippled Lines Apply to the Predictions:
- - - - : G = 500 kg/m²s
— — — : G = 1000 -
— . — : G = 1360 -

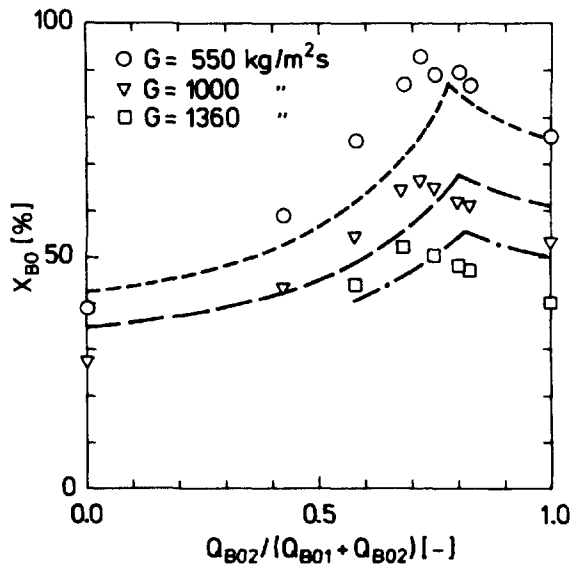

Fig. 4.33.b. Comparison between Measured and Predicted Burnout Steam Qualities. The Symbols Apply to the Measurements by Jensen and Mannov (1974): Test Section 17/26S. P = 70 bar. ΔT_{sub} = 100°C. The Stippled Lines Apply to the Predictions:
- - - - : G = 500 kg/m²s
— — — : G = 1000 -
— . — : G = 1360 -

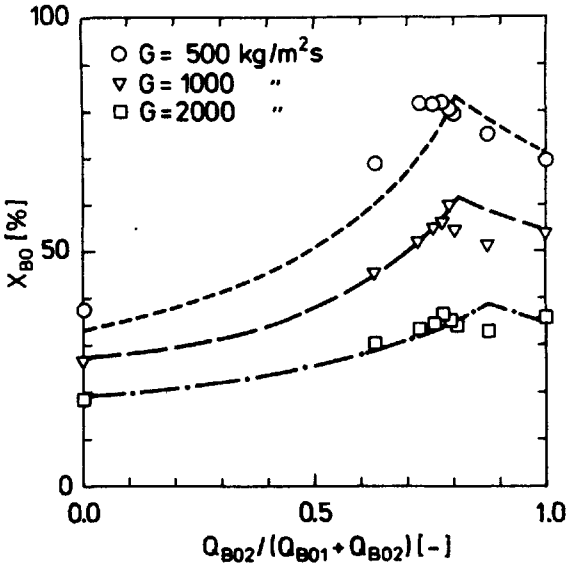

Fig. 4.34.a. Comparison between Measured and Predicted Burnout Steam Qualities. The Symbols Apply to the Measurements by Becker and Letzter (1975): Annular Test Section. d_1 = 12.0 mm. d_2 = 21.3 mm. L_d = 3.00 m. P = 30 bar. ΔT_{sub} = 10°C. The Stippled Lines Apply to the Predictions:
- - - - : G = 500 kg/m²s
— — — : G = 1000 -
— . — : G = 2000 -

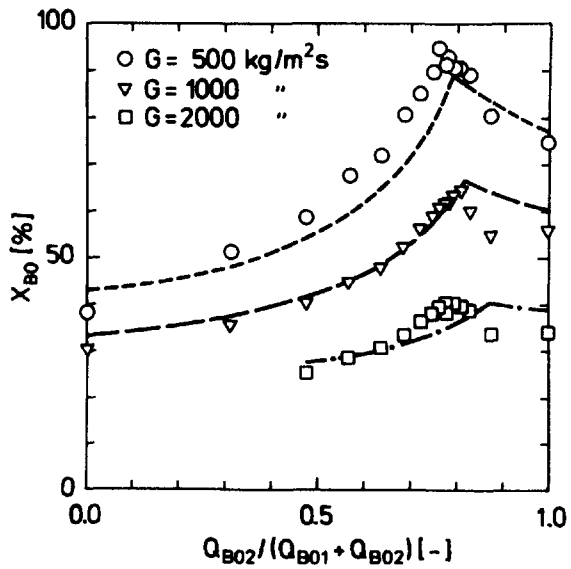

Fig. 4.34.b. Comparison between Measured and Predicted Burnout Steam Qualities. The Symbols Apply to the Measurements by Becker and Letzter (1975): Annular Test Section. d_1 = 12.0 mm. d_2 = 21.3 mm. L_d = 3.0 m. P = 70 bar. ΔT_{sub} = 10°C. The Stippled Lines Apply to the Predictions:
- - - - : G = 500 kg/m²s
— — — : G = 1000 -
— . — : G = 2000 -

ISBN 87-550-0593-4
ISSN 0418-6443